Master's thesis

NTNU
Norwegian University of Science and Technology
Faculty of Natural Sciences
Department of Physics

Kasper Aas Hunnestad

Visualizing Ferroelectric Domain Structures in $ErMnO_3$ and $Pb_5Ge_3O_{11}$ by Electron Microscopy

Master's thesis in Applied Physics and Mathematics
Supervisor: Antonius Theodorus Johannes van Helvoort, IFY
Co-supervisor: Dennis Gerhard Meier, IMA
June 2019

NTNU
Norwegian University of
Science and Technology

Kasper Aas Hunnestad

Visualizing Ferroelectric Domain Structures in $ErMnO_3$ and $Pb_5Ge_3O_{11}$ by Electron Microscopy

Master's thesis in Applied Physics and Mathematics
Supervisor: Antonius Theodorus Johannes van Helvoort, IFY
Co-supervisor: Dennis Gerhard Meier, IMA
June 2019

Norwegian University of Science and Technology
Faculty of Natural Sciences
Department of Physics

Abstract

Ferroelectric domain walls have attracted increasing attention as novel candidates for functional 2D systems just recently. These atomically sharp interfaces that can be moved, created and removed with electric fields, possess a flexibility in creating electronic devices not obtainable with other materials. However, for many multiferroic materials much of the underlying physics of charged domain walls is still unknown which limits the potential for developing devices. Complete investigations into the domain walls requires a spatial resolution range above mesoscopic to sub-nanoscopic which the transmission electron microscope (TEM) covers. However, the domain structures fails to give a dominant image contrast in conventional imaging, so specialized techniques are needed to visualize them. Even with these techniques, the contrast is easily misinterpreted and correlating the high resolution results of the TEM with other techniques such as the scanning electron microscope (SEM) can be highly advantageous. In this thesis, both SEM and TEM have been applied to investigate techniques and routines to study the ferroelectric domain structures of $ErMnO_3$ and $Pb_5Ge_3O_{11}$.

Specimens from both materials are prepared for the first time by mechanical tripod polishing, creating a large (> 1 mm) electron transparent edge without an amorphous layer or potential damage from ions commonly used in the thinning process. The SEM is used to give an overview on the domain walls along the large edge. Domains are found to only be visible above a critical thickness of 427 nm in $ErMnO_3$. A two step preparation was developed, where first SEM domain imaging was applied for a specimen above the critical thickness. Gentle Ar ion milling was thereafter done for TEM analysis of areas mapped by SEM. For $ErMnO_3$, the 002 reflection is found through simulations to be the best choice for dark-field (DF) imaging. Tripod polishing however introduced to many defects to find domain walls using DF. The specimens were still usable for high-quality lattice imaging with high resolution TEM and scanning transmission electron microscopy (STEM). Polarization was found in a perfect powder specimen using high-resolution high-angle annular DF (HAADF) STEM using serial acquisition and reconstruction in an uncorrected STEM. The $Pb_5Ge_3O_{11}$ tripod specimens on the other hand were free of induced defects, but the surface was damaged instead. Electron microscope studies of tripod specimens suffer severely from charging effects and electron beam damage. They amorphized quickly with a critical dose of 0.64 $\frac{C}{cm^2}$ ($3.99 * 10^2 \frac{e}{\mathring{A}^2}$) per nanometer in STEM mode. In TEM mode the material would decompose into Pb particles at a critical dose of 5.78 $\times 10^3 \frac{C}{cm^2}$ ($3.61 * 10^6 \frac{e}{\mathring{A}^2}$).

Regarding the ferroelectric domains of $Pb_5Ge_3O_{11}$, they were found to be easily rewritten during imaging in SEM, even at low currents ($\leq$0.1 nA) and voltages ($\leq$5 keV). Both thickness and geometry play a role, where thinner regions and sharp edges are the most vulnerable to being rewritten by the electron beam. Due to charging effects the edges were especially challenging to image, so the correlated routine using both TEM and SEM at the same location could not be applied to study the domain structure. Instead the SEM was used for the thicker parts of the tripod wedge and TEM on the thin edge. For $Pb_5Ge_3O_{11}$, the 003 reflection was found through simulations to be ideal choice for DF imaging, and several features resembling domain walls were studied using conventional DF TEM. Convergent beam electron diffraction was used to find polarization locally in a powder specimen, but could not be used on tripod specimens due to charging effects. The results of this study identify the boundaries for lattice imaging of domain walls in $Pb_5Ge_3O_{11}$ which is never achieved yet, but lattice imaging is essential for further investigations into the fundamental properties of these intriguing structural features.

Sammendrag

Ferroelektriske domenevegger har nylig tiltrukket økende oppmerksomhet som nye kandidater for funksjonelle 2D-systemer. Disse atomskarpe grensesnittene som kan flyttes, opprettes og fjernes med elektriske felt, kan brukes til å lage elektroniske enheter med en fleksibilitet som ikke finnes i andre materialer. For mange multiferroiske materialer er imidlertid mye av den underliggende fysikken til ladede domenevegger fortsatt ukjent som begrenser potensialet for å utvikle enheter. Fullstendig undersøkelser av domenevegger krever en romlig oppløsning i en rekkevidde fra over mesoskopisk til mindre enn nanoskopisk som transmisjonselektronmikroskopet (TEM) dekker. Domenestrukturene gir imidlertid ikke en dominerende bildekontrast, så spesialiserte teknikker er nødvendig for å visualisere dem. Selv med disse teknikkene, er kontrasten lett å misforstå og samsvare høyoppløsningsresultater fra TEM med andre teknikker som sveipelektronmikroskopet (SEM) kan være svært fordelaktig. I denne oppgaven har både SEM og TEM blitt anvendt for å undersøke teknikker og rutiner for å studere de ferroelektriske domenestrukturer av $ErMnO_3$ og $Pb_5Ge_3O_{11}$.

Prøver fra begge materialer prepareres for første gang ved mekanisk stativpolering, og danner en stor (> 1 mm) elektron-gjennomsiktig kant uten et amorft lag eller potensiell skade fra ioner som vanligvis brukes i tynningsprosessen. En SEM brukes til å gi en oversikt over domenevegger langs den store kanten. Domener er observert å bare være synlige over en kritisk tykkelse på 427 nm i ErMnO3. Et to-trinns preparering ble utviklet, hvor først en ble brukt til å ta oversiktsbilder på en prøve over kritisk tykkelse. Forsiktig Ar-ioneetsing ble deretter gjort for TEM-analyse av områdene kartlagt av SEM. For $ErMnO_3$ er 002 refleksjonen funnet gjennom simuleringer til å være det beste valget for mørkefelt bilder. Stativpolering innførte imidlertid for mange defekter for å finne domenevegger ved bruk av mørkefelt bilder. Prøvene var fortsatt anvendbare for høy kvalitets atom avbildning med høyoppløselig TEM og sveip transmisjonselektronmikroskopi (STEM). Polariseringen ble funnet i en perfekt pulverprøve ved bruk av en ringformet detektor i mørkefelt STEM ved å ta en serie bilder med rekonstruksjon i et ikke-korrigert STEM. $Pb_5Ge_3O_{11}$ stativpolerte prøver var derimot fri for induserte defekter, men overflaten ble skadet i stedet. Elektronmikroskopstudier av stativpolerte prøver lider sterkt av oppladningseffekter og stråleskader. De amorfiserte raskt med en kritisk dose på 0.64 $\frac{C}{cm^2}$ ($3.99 * 10^2 \frac{e}{\mathring{A}^2}$) per nanometer i STEM-modus. I TEM-modus dekomponerer materialet til Pb-partikler med en kritisk dose på 5.78 $\times 10^3 \frac{C}{cm^2}$ ($3.61 * 10^6 \frac{e}{\mathring{A}^2}$).

Angående de ferroelektriske domenene til $Pb_5Ge_3O_{11}$, ble de funnet å bli lett omskrevet under avbildning i SEM, selv med en lav elektronstrøm ($\leq$0.1 nA) og spenning ($\leq$5 keV). Både tykkelse og geometri spiller en rolle, hvor tynnere områder og skarpe kanter er de mest sårbare for å bli omskrevet av elektronstrålen. På grunn av oppladningseffekter var kantene spesielt utfordrende for avbildning, så rutinen med å samsvare TEM og SEM på samme lokasjon i prøven kunne ikke brukes for å studere domenestrukturen. I stedet ble SEM brukt til tykkere deler av de stativpolerte prøvene og TEM på den tynne kanten. For $Pb_5Ge_3O_{11}$ ble 003-refleksjonen funnet gjennom simuleringer til å være det ideelle valget for mørkefelt bilder, og flere grensesnitt som ligner på domenemurer ble studert. Konvergerende elektron diffraksjon ble brukt til å finne polarisering lokalt i en pulverprøve, men kunne ikke brukes på stativpolerte prøver på grunn av oppladningseffekter. Resultatene av dette studiet identifiserer grensene for avbildning av atomstrukturen i domenevegger i $Pb_5Ge_3O_{11}$, som aldri har blitt oppnådd, men er essensielt for videre undersøkelser av de grunnleggende egenskapene av de fascinerende domeneveggene.

Preface

This thesis is the conclusion of my 5 year M.Sc. degree in Applied Physics at the Department of Physics at the Norwegian University of Science and Technology (NTNU), during the spring of 2019. The work has been carried out at the TEM Group with Professor Antonius van Helvoort as my supervisor, and in collaboration with Professor Dennis Meier as co-supervisor and PhD. candidate Theodor Holstad at the Department of Materials Science and Engineering. Some of the work has also been carried out at the NTNU NanoLab facilities. The thesis is a continuation of a specialization project carried out during the fall of 2018. I hereby declare that this Master's thesis is my own independent work and is in accordance with the regulations for the Master's degree program in Applied Physics at NTNU. All specimen preparation, data collection, data handling and writing was done by me.

First and most importantly, I want to thank Ton for the valuable guidance he has provided throughout the last year and making the work possible. The weekly meetings have been truly rewarding and encouraging, and learning the TEM has been an exciting experience. I also want to thank Theodor for insightful discussions on the materials, and for accompanying some of the lab work when exploring the new material. I am also grateful to Ton, Dennis and Theodor for your help in planning the project and for helping me present the work in a (somewhat) orderly fashion. A final thanks the engineers, Bjørn Soleim and Ragnhild Sæterli, for providing training, and especially for helping me whenever the microscopes was not behaving.

Kasper Aas Hunnestad

Trondheim, June 11, 2019

Abbreviations

- IC - Integrated Circuit
- TEM - Transmission Electron Microscope
- (F)FT - (Fast) Fourier Transform
- FCC - Face Centered Cubic
- BCC - Body Centered Cubic
- NA - Numerical Aperture
- VLM - Visual Light Microscope
- FEG - Field-emission Gun
- DP - Diffraction Pattern
- c/o lens - Condenser/Objective lens
- BF - Bright-field
- DF - Dark-field
- HRTEM - High Resolution Transmission Electron Microscopy
- POA - Phase-object Approximation
- WPOA - Weak Phase-object Approximation
- SA(E)D - Selected Area (Electron) Diffraction
- CBED - Convergent Beam Electron Diffraction
- CCD - Charge-coupled device
- EDX - Energy Dispersive X-ray Spectroscopy
- ZOLZ - Zero-order Laue zone
- FOLZ - First-order Laue zone

- HOLZ - Higher-order Laue zone
- BFP - Back Focal Plane
- STEM - Scanning transmission electron microscope
- HAADF - High-angle annular dark-field
- EDS-STEM - Energy Dispersive X-ray Spectroscopy-STEM
- SCBED - Scanning Convergent Beam Electron Diffraction
- SEM - Scanning Electron Microscope
- BSE - Back-scattered electrons
- SE - Secondary Electrons
- SDS - Starting Domain Structure
- FDS - Free Domain Structure
- DLF - Diamond-lapping film
- VLM - Visible Light Microscope
- FIB - Focused Ion Beam
- SPM - Scanning Probe Microscopy
- ETD - Everhart-Thornley Detector
- EELS - Electron Energy Loss Spectroscopy
- DPC-STEM - Differential Phase Contrast STEM

Contents

Chapter 1

Introduction

1.1 Background and Motivation

The demand for novel low-power information and communication technologies has pushed a revolution in how functional materials are designed[1]. Of particular interest are novel 2D systems, such as oxide interfaces, single-layer graphene and MoS_2, as well as surface states in topological insulators, because they exhibit a wide variety of functional physical properties. Most recently, domain walls in ferroelectrics came into the spotlight[2][3]: These domain walls separate regions with different orientation of the electric ordering. They occur naturally, and in contrast to artificially grown interfaces, which reside as the growth has been completed, domain walls can be generated, deleted or moved by an electric field at will any time. Because of this additional degree of freedom, domain walls hold great promise as "active" 2D materials for next-generation nanoelectronics[4][5][6].

More specifically, the domains walls of ferroelectrics where the polarization meets head-to-head or tail-to-tail are of interest as the interface accumulates or is depleted of mobile carriers[7]. Under applied electrostatic fields, these domain walls can then display functional behaviour similar to that of transistors or conductors, contained within the atomically sharp interface surrounded by the insulating bulk material[4]. However, these domain walls are unstable in conventional ferroelectrics such as $BaTiO_3$ and $BiFeO_3$, as the energy cost of the charged domain walls are greater than their neutral counterparts[6]. Finding other ferroelectrics where charged domain walls are both present and stable can therefore be important for future oxide electronics.

The hexagonal manganites, h-$R$$MnO_3$ (R = Er, Y, Sc, Dy, Ho, Tm, Yb, Lu), have not been studied as much as the more conventional ferroics, as the ferroelectric response is about twenty times weaker[4][5]. These materials belong to a class of improper ferroelectrics where the extra energy from the charged domain walls is not essential to the domain formation. Thus, stable charged domain walls possessing either enhanced conductivity or a transistor-like response to external fields, are both stable and present in equilibrium conditions. In additions, special vortices of intersecting domain walls have also been reported having unsual charge transport properties, and possible applications is worth exploring[5][8]. There is however much left to be worked out on the fundamental

characteristics on the charged domain walls before exclusive domain wall devices can be made.

Besides the hexagonal manganite, another ferroelectric, $Pb_5Ge_3O_{11}$ or lead germanate, has not well understood head-to-head and tail-to-tail domain walls[9][10][11]. Similar to $ErMnO_3$, this material is a ferroelectric with unusual domain structure[12], but in contrast to $ErMnO_3$, this material is a far less studied in recent years (218 papers on $ErMnO_3$ against 41 on $Pb_5Ge_3O_{11}$ in the last ten years[1]). Poor crystal quality and charging effects may be the reason researchers diversed away from it. The majority of research on this material was conducted in the 1970's and 1980's before advanced transmission electron microscopes (TEM) and scanning electron microscopes (SEM) became accessible, and a main interest was in the optical rotation properties of the ferroelectric domains[13]. As a result, the domain structures have mainly been visualized through optical techniques, exploiting the fact that opposite domains rotate light differently.

Optical techniques are however not capable of probing the crystal structure with the same resolution as the TEM, and only a short conventional TEM study on the bulk material is reported[14], without connecting the results towards the ferroelectric properties. The details of the domain structure at the atomic scale is therefore unknown, but the presence of charged domain walls imply the same functionality as has been found in $ErMnO_3$. Measurements on conductivity using scanning probe microscopy (SPM), a relatively new characterization class, can not provide confirmation[15]. This motivates an investigations into the atomic structure of the domain walls to get insight into this paradox.

To study domain structures requires a certain spatial resolution, as the width of domain walls is just a few nanometers (several micrometers apart). SPM has been the workhorse technique for much of the research done on the domain structure in these ferroelectrics, but electron microscopes is also becoming more conventional ways for studying ferroelectrics. The TEM holds the highest resolution of any microscopy technique and yet has a broad range of additional signals to explore different structural, compositional and functional aspects[16]. It has also been a key instrument for discovering the details on the ferroelectric mechanisms of $ErMnO_3$[5]. With the high resolution, the atomic structure can be directly probed, although the small regions are not representative for the entire domain structure.

Structural information on the larger domain structure is therefore needed with high resolution, and while the SPM techniques are conventional for ferroelectrics, SEM is highly complentary with the TEM techniques and specimens. So far, visualization of the domain structure in a SEM of both the hexagonal manganites and $Pb_5Ge_3O_{11}$ has been reported[17][9], but not in combination with the TEM using the same specimens and domain walls. The domain structure of $ErMnO_3$ has been studied with TEM thoroughly, but mostly with a focus towards the material and not the TEM techniques and specimen preparation that could be suboptimal[18][19][5][20][4][8]. Therefore, **the first goal** of this thesis will be to find and report a general platform for studying ferroelectric domain

[1]Found from a Web of Science search between 2009 and 2019, with the following search criteria: ErMnO3 OR (hexagonal NEAR/1 manganite*) in topic or title, Pb5Ge3O11 in topic or title.

structures with a correlated SEM/TEM set-up, applicable for both overview and high resolution investigations. For this purpose, the tripod polisher[21], which is still untested on both materials, is applied to gain large high quality specimens that fits both overview and high resolution techniques. $ErMnO_3$ is especially well suited as a test case as the domain structure is easily recognizable as it forms six-fold vortices at the domain wall intersections. On the other hand, $Pb_5Ge_3O_{11}$ display irregular domain structures that is challenging to identify and separate from defects and surface variations, so the experience obtained with $ErMnO_3$ will be useful when working with this material.

Since $Pb_5Ge_3O_{11}$ has barely been studied in the TEM, there is a lot of open questions regarding how it should be done. The only paper applying the TEM to this material used a powder specimen on a carbon grid, with a TEM operating at 800 kV, far above the conventional value of 200 kV in use today[14]. Other reports that a 25 kV SEM is enough to reverse the polarization ordering, so operating at 200 kV can also change the structure too fast to capture the natural domain structure[9]. A powder specimen with grains in the size of a few micrometers are also unlikely to contain the larger domains and therefore make it challenging to find domain walls[11]. Overcoming these limitations with the correlated SEM/TEM routine with the tripod polisher established for $ErMnO_3$ and any problems associated with charging effects is also undocumented, and may be necessary to investigate before conclusive TEM studies can be made. **The second goal** of this thesis is therefore to establish TEM techniques and routines specific for $Pb_5Ge_3O_{11}$, while addressing challenges with the materials behaviour in electron microscopes and with an interest towards the ferroelectric domain structures. As the central feature of interest is the charged domain walls which are most likely atomically sharp, an additional goal is high resolution information on the domain structures.

1.2 Outline

This thesis is divided into six chapters. The next chapter, chapter 2, will survey the relevant theory for this thesis, beginning with the relevant basics of solid state physics. As the TEM is a core part of this work, the theory on its design, working principles and operational modes is covered. Most of this overlaps with the SEM which is the second important instrument used, but a separate section is included for understanding SEM specific theory. Ferroelectricity is also a central part of the study as the ferroelectric domains are the main interest, and both fundamental principles of ferroelectricity and the details on ferroelectric mechanisms in $ErMnO_3$ is presented. Finally, a brief survey is given of $ErMnO_3$ and $Pb_5Ge_3O_{11}$ and their relevant properties for a TEM study such as crystal structure and diffraction conditions.

Chapter 3 covers the experimental details in the work. For sample preparation, a tripod polisher is used to mechanically polish the samples into electron transparency using a specific recipe, and further thinning using ion milling with low-energy (3 keV) Ar ions. A detailed explanation of this sample preparation technique is then given, and the different parameters during this process is listed. Necessary parameters for the SEM and TEM that is not included in each image is also listed here along with the used

softwares for data handling.

In chapter 4, the results are presented along with a discussion. The first section covers the sample preparation procedure using the tripod polisher or a mortar and pestle to prepare specimens. The second section goes into detail on the charging effects that was present in $Pb_5Ge_3O_{11}$. This includes a structural and compositional analysis of the material after decomposition, as well as measurements on critical doses. Finally, the two last sections covers the results and discussion on the domain structures for both materials, where the sections are split between the different techniques and purpose (SEM, TEM, overview and high resolution imaging). The results on $ErMnO_3$ is mainly directed towards the first goal of finding a correlated SEM/TEM routine with the tripod polisher, while the results on $Pb_5Ge_3O_{11}$ is mainly towards the second goal on finding techniques for studying the domains. Finally, the conclusion of the thesis is found in chapter 5, and suggestions for further works are found in chapter 6, although some suggestions are also found throughout the discussion. Most of these are either focused at new TEM techniques or new instruments that can overcome some of the challenges faced in the present study. Additional data, simulations, calibrations and detailed preparation routine are given in the appendices.

Chapter 2

Theory

The physics of crystals, their properties and how they are studied through the interaction with waves is a large and intriguing field, and multiple textbooks are needed for covering all the different aspects and details. The following chapter will attempt to condense the most relevant theory into short sections, to help with the understanding of later chapters. The first chapter will cover the basic physics of crystals, their representation using lattice vectors and reciprocal lattice vectors and how they are systematically categorized. Furthermore, the fundamental ideas of how waves scatter on the crystal to form diffraction patterns and the rules governing these processes will be covered. The second section will go into detail on the transmission electron microscope focusing on basic principles, design and techniques. In addition, a more specific description of electron interaction with the specimen are given, and how these contribute to create contrast in images. The scanning electron microscope is used as a complementary technique to the TEM, so a brief section goes into detail on the instrument and how contrast in images can be interpreted. Since the ferroelectric properties of $ErMnO_3$ and $Pb_5Ge_3O_{11}$ are central to this thesis, the next section will cover the main principles of ferroelectricity. A brief survey of the field of ferroelectrics will be given for clarity, with an emphasis on the mechanisms at play in the geometrically driven improper ferroelectrics. Finally, a systematic description of $ErMnO_3$ and $Pb_5Ge_3O_{11}$ including crystal structure, symmetry and diffraction patterns is given.

2.1 Crystal Structure and Diffraction

The first sections are based on the book *Introduction to Solid State Physics* from Charles Kittel[22], except for the point group and symmetry theory which is taken from a compendium by Emil Samuelsen[23]. The last section on Dynamical theory is based on the book *Transmission Electron Microscopy and Diffractometry of Materials* from Brent Fultz and James Howe[24], in addition to the book *Advanced Transmission Electron Microscopy* by Jian Zuo and John Spence[25].

2.1.1 Crystal Structure

Crystals consist of atoms bonded together by electrostatic forces in a periodical fashion, organized into unit cells located at points on a lattice. The are held together by the bonding between the negatively charged electrons and positively charged nucleus, and this bonding are categorized into four different types: Van der Waals, ionic, metallic or covalent bonding. Furthermore, the crystals periodic arrangement can also be categorized into different structures that are expressed through mathematical vectors and symmetry considerations.

Mathematical Representation

An ideal crystal consist of an infinite periodical lattice convoluted with a basis. The lattice consists of points in space, while the basis consists of the atoms that make the crystal. When convoluted, the result is the atom set (basis) placed at each lattice point. Since the lattice is periodic, only a integer multiple of three vectors are necessary to get from any one lattice point to another and these are the primitive translation vectors $\mathbf{a}, \mathbf{b}, \mathbf{c}$. The translation vector that goes from one point to another identical point is therefore defined as

$$\mathbf{T} = u_1\mathbf{a} + u_2\mathbf{b} + u_3\mathbf{c} \tag{2.1}$$

where u_1, u_2, u_3 are integers when moving along identical lattice points, or between 0 and 1 when moving to different atoms of the basis. The unit cell spanned by the three vectors are called the primitive unit cell and is the smallest building block for any crystal containing one atom, a parallelepiped with volume $\mathbf{a} \cdot \mathbf{b} \times \mathbf{c}$. The usual convention is to use unit cells with the atoms/lattice point in the corner of the cell, but other choices are also possible. For instance, the Wigner-Seitz and Brillouin zones are the primitive unit cells with the atom in the center, for the crystal and reciprocal lattice respectively. Other unit cells larger than this may be more useful to work with though, as the symmetry relations may be more obvious. The crystal axes are also defined as these vectors, often with the longest vector denoted as the $\boldsymbol{c}$-axis. The angles between the vectors are defined as:

$$\mathbf{a}\angle\mathbf{b} = \gamma, \quad \mathbf{a}\angle\mathbf{c} = \beta, \quad \mathbf{b}\angle\mathbf{c} = \alpha \tag{2.2}$$

The electron density, $n(\mathbf{r})$, is one example of a characteristic property related to the crystal structure. Since the lattice is a periodic function, the electron density must be as well, and this implies that a Fourier analysis is useful to study the structure. In three dimensions, the Fourier series and its coefficient becomes:

$$n(\mathbf{r}) = \sum_{\mathbf{G}} n_{\mathbf{G}}\, e^{i\mathbf{G}\cdot\mathbf{r}}, \quad n_{\mathbf{G}} = V_c^{-}1 \int_{cell} dV n(\mathbf{r})\, e^{-i\mathbf{G}\cdot\mathbf{r}} \tag{2.3}$$

Where cell and V_c stands for a unit cell and its volume in the crystal. The set of vectors $\mathbf{G}$ are called the reciprocal lattice vectors, and they define the reciprocal lattice which is related to the inverse of the spatial crystal lattice. More precisely, it is related to the

spacing between parallel lattice planes d, as $|G| = 2\pi/d$. It can be shown that the $\mathbf{G}$ vectors can be written in the following form:

$$\mathbf{G}(hkl) = h\mathbf{b_1} + k\mathbf{b_2} + l\mathbf{b_3}, \quad \mathbf{b_i} = \frac{2\pi}{V_c}\mathbf{a_j} \times \mathbf{a_k}, \quad \epsilon_{ijk} = 1 \tag{2.4}$$

hkl are integer numbers, while b_i are the primitive reciprocal lattice vectors and $\mathbf{a_1}, \mathbf{a_2}, \mathbf{a_3}$ is $\mathbf{a}$, $\mathbf{b}$, $\mathbf{c}$, respectively. Another useful property is that $\mathbf{b_i} \cdot \mathbf{a_j} = 2\pi\delta_{ij}$, which enables the translation symmetry of n($\mathbf{r}$) in equation 2.3 since $e^{i\mathbf{G}\cdot(\mathbf{r}+\mathbf{T})} = e^{i\mathbf{G}\cdot\mathbf{r}}$. In order to also understand the planes and directions in the lattices, the Miller indices are used. They are a set of three numbers (hkl), representing the plane that is perpendicular to the unit or translation vector containing the reciprocal of the Miller indices. For example, a unit vector of $[\frac{1}{2}10]$ in real space will become [210], which represents the lattice plane (210) intersecting the $\mathbf{a}$-axis at $\frac{1}{2}$, the $\mathbf{b}$-axis at 1 and never the $\mathbf{c}$-axis[1].

Systematic description of crystals

While the mathematical representation of the crystal structure are described above, they are also categorized into a set of unique lattices. The Bravais lattices are a common name for a distinct type of lattice, and there are in total fourteen three-dimensional lattices that make up all possible lattices for a crystal structure. The general structure is the triclinic, with the thirteen other lattices being special cases listed in table 2.1. Furthermore, they are divided into seven crystal systems that are combined with the centering types (additional lattice points): Primitive(P), Base-centered(C), Body-centered(I) and Face-centered(F).

Most crystallines materials have non-primitive unit cells. These unit cells are often more convenient for understanding the symmetry elements in the lattice, and understanding the symmetry elements is crucial. For instance, the cubic unit cells always contain a fourfold symmetry along the axes perpendicular to the faces, even if this is not obvious from the primitive unit cells. An example of an interesting structure is $CaTiO_3$ as shown in figure 2.1(b). This perovskite is a primitive cubic structure with a basis including three different atoms: Ca atoms in the corners at the lattice points, Ti atoms in the center and O atoms at the faces.

Symmetry of Crystals

To further describe the symmetry of crystals which is closely related to the physical properties, point groups and space groups are used. Each point group is a set of symmetry operations around a point (rotation axes, mirror planes and inversion centers), and there are 32 unique point groups used to describe the possible crystal structures. Furthermore, when also taking translational symmetry (screw axes and glide planes) into account, the the combination of point symmetry and translation symmetry constitute the space group of the crystal structure. In total there are 230 distinct space

[1]While the the brackets [100] indicate directions, the parenthesis (100) indicate a plane. A group of symmetrically identical planes are defined as {100}, and identical directions are grouped as <100>.

Table 2.1: The 7 Bravais systems in three dimensions with their possible crystallographic lattices and restrictions.

System	**Unit cell**	**Restrictions**
Triclinic	P	$\mathbf{a} \neq \mathbf{b} \neq \mathbf{c}$ $\alpha \neq \beta \neq \gamma$
Monoclinic	P, C	$\mathbf{a} \neq \mathbf{b} \neq \mathbf{c}$ $\alpha = \gamma = 90° \neq \beta$
Orthorombic	P, I, F, C	$\mathbf{a} \neq \mathbf{b} \neq \mathbf{c}$ $\alpha = \gamma = \beta = 90°$
Tetragonal	P, I	$\mathbf{a} = \mathbf{b} \neq \mathbf{c}$ $\alpha = \gamma = \beta = 90°$
Cubic	P, I, F	$\mathbf{a} = \mathbf{b} = \mathbf{c}$ $\alpha = \gamma = \beta = 90°$
Rhombohedral	P	$\mathbf{a} = \mathbf{b} = \mathbf{c}$ $\alpha = \gamma = \beta < 120°, \neq 90°$
Hexagonal	P	$\mathbf{a} = \mathbf{b} \neq \mathbf{c}$ $\alpha = \beta = 90°, \gamma = 120°$

groups, and every crystal has its symmetry elements described entirely by one of these groups. Using the structure of $CaTiO_3$ in room temperature as an example (not the same as figure 2.1(b)), it belongs to space group 62 or *Pnma* and point group *mmm*. The complete space and point group notations will not be covered, but the space group notation indicates that it belongs to the primitive orthorhombic system, and the point group notation indicate three mirror planes.

The primary motivation for labelling and categorizing crystals based on their symmetries is due to Neumann's principle, which states that if a crystal is invariant to a symmetry operation, then any physical property must also remain invariant to the same symmetry operation. This implies that the macroscopic properties of the crystal are directly related to the symmetry of the unit cell at the atomic scale. Therefore the orientation of the crystal is vital to understanding the behaviour of the material.

An important example of this is spontaneous polarization, where the crystal sets up a polarization field in one particular direction. Due to Neumann's principle, materials showing spontaneous polarization can not posess any inversion centers. An inversion center would imply that the polarization direction could be inverted without changing the crystal (which is the opposite of spontaneous polarization). By looking at the structure of $CaTiO_3$ in figure 2.1(b), the inversion symmetry implies that there are no spontaneous polarization present. For an effect such as piezoelectricity or ferroelectricity (see section 2.4) to then occur, the material must undergo a structural phase transition to a different crystal structure without an inversion center.[2]

[2] $CaTiO_3$ actually does undergo a phase transition at 1498K from orthorombic (below) to tetragonal (above), and from tetragonal to cubic at 1634K, enabling piezoelectricity at room temperature[26].

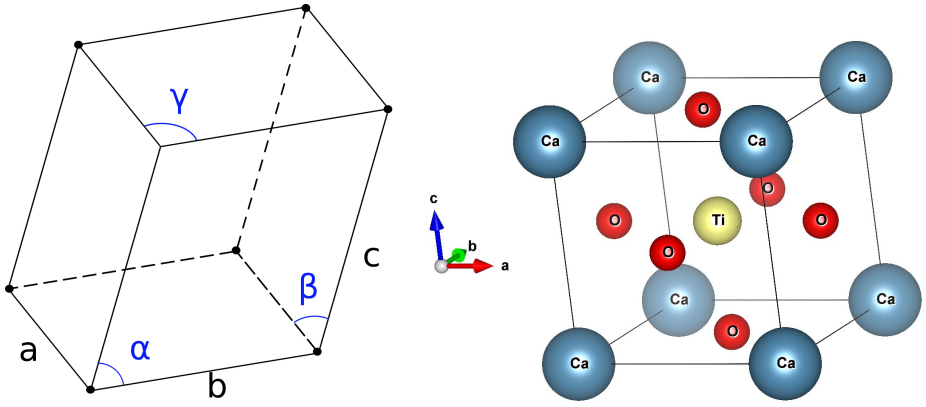

(a) (b)

Figure 2.1: Figures shows (a), a general triclinic unit cell and (b), the crystal structure of the perovskite (ABO_3) $CaTiO_3$. In the case of $CaTiO_3$, the basis include a Ca at the lattice point, a Ti atom displaced to the center($\frac{1}{2}\mathbf{a}+\frac{1}{2}\mathbf{b}+\frac{1}{2}\mathbf{c}$) and three O atoms at the faces($\frac{1}{2}\mathbf{a_i}+\frac{1}{2}\mathbf{a_j}, i \neq j$).

Crystal structures, including their point groups and space groups offer the most fundamental understanding of materials, and can be studied by diffraction techniques performed for example in a TEM (see section 2.2).

2.1.2 Kinematic Diffraction

Braggs Law

When studying the crystal structures described above, diffraction is the most commonly used method, and single elastic diffraction events (kinematic) are the simplest and most intuitive to explain. Diffraction experiments can be done by any waves or particles with a wave-like nature such as electron, neutrons or photons. One of the simplest explanations for diffraction was given by W.L. Bragg and is contained in the Bragg law:

$$2d_{hkl}sin(\theta) = n\lambda \tag{2.5}$$

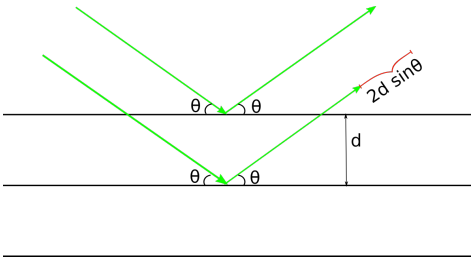

Figure 2.2: Sketch of Bragg diffraction on lattice planes.

The idea is shown in figure 2.2, where the lines represents periodic lattice planes with a distance d. The beam of some wave enters the crystal with an angle θ and are reflected by the lattice plane. Since the wave can be reflected at different planes, they obtain different phases which leads to constructive and destructive interference. When the phase difference are an integer number of the wavelength, the result is constructive interference and this is expressed in equation 2.5. This law offers a very simplified

explanation of diffraction in crystals. It explains how they originate in the periodicity of the lattice and how diffraction produce a pattern of sharp peaks that represents this periodicity. It can also be used to find the lattice planes periodicities when the wavelength of the beam is known. However, the law does not offer any information on the intensity of the reflected beam, or on the basis of atoms at each lattice point.

Laue Equations and Ewalds Sphere

To generalize the Bragg's law, the lattice planes must be replaced by the crystal specimen, as in figure 2.3(a). In addition, the intensity I must be introduced as proportional to the absolute square of a scattering amplitude, $I \propto |F|^2$. Using the same arguments as for Bragg's law, the phase difference between two waves reflected at two points a distance $\mathbf{r}$ away from each other are $(\mathbf{k} - \mathbf{k}') \cdot \mathbf{r}$. From each volume element dV, the amplitude of the scattering wave is then to be proportional to a scattering density, $\rho(\mathbf{r})$, so in total we then have for the scattering amplitude:

$$F = \int dV \rho(\mathbf{r}) e^{i(\mathbf{k}-\mathbf{k}')\cdot\mathbf{r}} \tag{2.6}$$

This is essentially the Fourier transform (FT) of $\rho(\mathbf{r})$. An important consequence of this is that the FT of any function, $F(\mathbf{k})$, obeys the following equation: $F(\mathbf{k}) = F^*(-\mathbf{k})$. Combining this with the fact that intensity is proportional to the absolute square (ignoring that one side is the complex conjugate) the result is $I(\mathbf{k}) = I(-\mathbf{k})$, meaning the intensity is always centrosymmetric, a property also known as Friedel's law. It should also be mentioned here that the scattering density is different for different types of waves. X-rays only scatter on the electron cloud and thus the electron density $n(\mathbf{r})$ is used, electrons scatter on the entire electrostatic potential $V(\mathbf{r})$ (see section 2.2.3 for specific treatment) and neutrons scatter on the nucleus spin structure. Inserting equation 2.3 in equation 2.6 and substituting electron density for the scattering density, the resulting scattering amplitude is:

$$F_{\mathbf{G}} = \sum_{\mathbf{G}} \int dV \rho_{\mathbf{G}} e^{i(\mathbf{G}-\Delta\mathbf{k})\cdot\mathbf{r}} \tag{2.7}$$

Since the integral only contains one term dependent on $\mathbf{r}$, and this is contained within the phase factor, it will average to zero unless the exponent goes to zero. This gives the diffraction condition: $\Delta\mathbf{k} = \mathbf{G}$. This condition is central to diffraction experiments, and is visualized by the Ewalds sphere construction in figure 2.3(b). In the schematic, the sphere constructed from the the ingoing and outgoing wave vectors must overlap with points in the reciprocal space for diffraction to occur. For electron diffraction in TEM, the wavelength is very short and hence the Ewald sphere is very flat. In addition, diffraction may also occur without perfect overlap since the reciprocal points are extended in the direction of the beam (i.e. relrods) due to the limited size of the sample in the beam direction. The condition is modified by the deviation parameter $\mathbf{s}$,

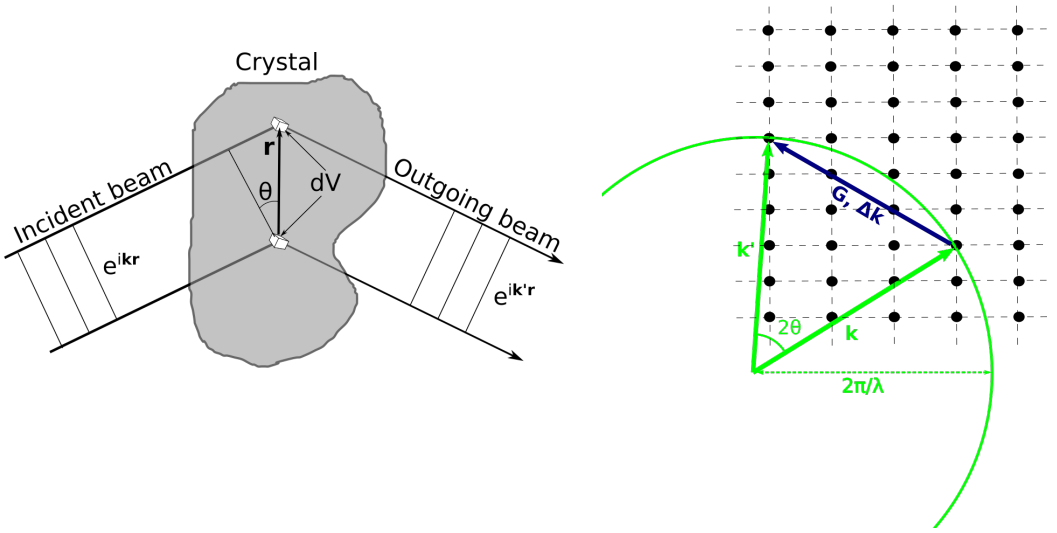

(a) (b)

Figure 2.3: (a) Sketch of general diffraction of crystal from plane waves entering crystal with wave vector **k** and exiting (diffracted) with wave vector **k'**. (b) Ewalds sphere (green) and a reciprocal lattice representing diffraction condition of plane waves entering crystal with wave vector **k** and exiting (diffracted) with wave vector **k'**.

so that $\Delta k = \mathbf{G} + \mathbf{s}$. The intensity of the beam does however decrease sharply with increasing $\mathbf{s}$ for a specimen with thickness t:

$$I_G(s) \sim \frac{sin^2(\pi ts)}{(\pi s)^2} \tag{2.8}$$

The consequences of this will be discussed in the section on contrast in TEM imaging (section 2.2.4). Since the Ewalds sphere can overlap at multiple point, the zero-order Laue zone (ZOLZ), first-order Laue zone (FOLZ) and higher-order Laue zone (HOLZ) are terms for the first, second or higher time a point has overlapped with the sphere. Restricting the analysis to elastic scattering (no energy loss), the diffraction condition becomes:

$$(\mathbf{k} + \mathbf{G})^2 = k^2 \quad \text{or} \quad 2\mathbf{k} \cdot \mathbf{G} = G^2 \tag{2.9}$$

From these general equations for the diffraction condition, Bragg's law can be derived. Another set of equations that be derived from the first diffraction condition, is the Laue equations. They are found by multiplying each side with the translational vectors $\mathbf{a}, \mathbf{b}, \mathbf{c}$:

$$\mathbf{a} \cdot \mathbf{\Delta k} = 2\pi h, \quad \mathbf{b} \cdot \mathbf{\Delta k} = 2\pi k, \quad \mathbf{c} \cdot \mathbf{\Delta k} = 2\pi l \tag{2.10}$$

This set of equations emphasizes that the change in wave vector, $\Delta\mathbf{k}$, in the direction and multiplied with each lattice parameter must be an integer multiple of 2π. All the equations above take into account the conditions for diffraction to occur with measurable

intensity, and the most important takeaway is the diffraction condition which states that the change in wave vector must be a point in reciprocal space. However, they leave out the difference between different atoms and their placement in the basis. While two different elements may both satisfy diffraction at some point, they do not necessarily scatter at equal intensity or interfere constructively.

2.1.3 Atomic Form Factor and Structure Factor

When considering a structure such as $CaTiO_3$ in figure 2.1(b), there are three different atoms that must be accounted for by three different atomic form factors. Each will have a different electron density in equation 2.6, and as such the scattering amplitude must be different for each. First, the equation are rewritten into $F_{\mathbf{G}} = NS_{\mathbf{G}}$ for a crystal of N unit cells, where $S_{\mathbf{G}}$ is called the structure factor and $\Delta\mathbf{k}$ has been replaced by $\mathbf{G}$ due to the diffraction condition (defined section above). Furthermore, the scattering density and structure factor can be written as a sum over the basis (atoms labelled by j):

$$S_{\mathbf{G}} = \sum_j F_j = \sum_j \int dV \rho_j(\mathbf{r} - \mathbf{r_j}) e^{-i\mathbf{G}\cdot\mathbf{r}} \tag{2.11}$$

Since it's only the difference $\mathbf{r} - \mathbf{r_j}$ that is important when considering a single basis, we redefine it as $\mathbf{r'}$, and define the integral as the atomic form factor, f_j:

$$f_j = \int dV \rho_j(\mathbf{r'}) e^{-i\mathbf{G}\cdot\mathbf{r'}} \tag{2.12}$$

This new factor is then an atomic property, unique for different atoms and must be used in structures such as $CaTiO_3$. Combining equation 2.11 and 2.12, the result are the equation for the structure factor used to find the scattering strength:

$$S_{\mathbf{G}} = \sum_j f_j e^{-i\mathbf{G}\cdot\mathbf{r_j}} \tag{2.13}$$

With this equation, all atomic properties are contained in the atomic form factor, while the importance of their placement is contained in the phase factor. The structure factor is therefore the general tool to connect kinematic diffraction experiments with crystal structures. Another advantage of this is that if the interaction mechanism is not as described in section 2.1.2, this can be introduced as a modification to the atomic form factor alone, keeping much of the considerations for the structure factor the same[3].

Since the intensity is proportional to the square of the structure factor, $S_{\mathbf{G}}$, certain diffraction spots may disappear if the sum goes to zero. Expanding the exponent of equation 2.13 by using equation 2.4, the result is:

$$\mathbf{G} \cdot \mathbf{r_j} = 2\pi(hx_j + ky_j + lz_j) \tag{2.14}$$

[3]The calculation for electron scattering is done in section 2.2.3, but similar calculations can be done for other waves such as X-rays and neutrons while keeping reflection conditions the same.

If we consider the FCC lattice with a single atom as basis, it has identical atoms at $(000, 0\frac{1}{2}\frac{1}{2}, \frac{1}{2}0\frac{1}{2}, \frac{1}{2}\frac{1}{2}0)$, and then the structure factor becomes:

$$S(hkl) = f[1 + e^{-i\pi(k+l)} + e^{-i\pi(h+l)} + e^{-i\pi(h+k)}] \tag{2.15}$$

From this the kinematic reflection conditions can be worked out, and they state that reflections/diffraction can only occur if all hkl are either odd or even. For instance, the reflection (100) is forbidden for diffraction of FCC crystals. When indexing a diffraction pattern (DP) in a TEM, this is important to remember, as the first (closest) diffraction spot may be (200) instead of (100) and the lattice parameter may be calculated to twice the actual size. However, due to dynamical scattering effects kinematically forbidden reflections might be present, but the kinematic approach might be more illustrative.

2.1.4 Dynamical Theory of Diffraction

Mathematical Framework for Dynamical Theory

In section 2.1.2 the goal was to represent single diffraction events (kinematic diffraction) which is the simplest case as the incoming and outgoing beam is the only concern. However, if multiple diffraction events[4] (dynamic diffraction) is to be considered then the time-independent Schrödinger equation including the periodic potential must be solved, so the propagation of electrons through the crystal can be treated on a more general basis. While dynamical theory is much more time consuming than the kinematic theory above, it is a vital part of electron diffraction techniques (section 2.2.5) and also needed to understand how simulations for electron microscopy works. It also allows for a more detailed and excact analysis which is not restricted to Friedel's law. Here, the main interest is the TEM so assumptions only relevant for a high voltage (200 kV) electron microscope will be made, and absorption is not included in the deduction below.

To begin with, the quantum mechanical formulation of crystals must be introduced, and there are primarily two ways of representing electron wave functions. The difference comes from using two different sets of orthogonal basis, one for reciprocal space and one for real space. The first method is the beam representation, which is most analogous to the previous section as it uses the reciprocal space basis of $\{\Phi_{\mathbf{g}}(\mathbf{r})\}$ (amplitudes $\{\phi_{\mathbf{g}}\}$), where each diffracted beam is represented by a single wave function with the same wave vector magnitude, but different orientation. This is most suited for treating the electrons in vacuum (i.e. constant potential) as the boundary conditions are easily interpreted and also for defining the problem of dynamical diffraction. In the opposite case, the Bloch wave representation uses wave functions $\{\Psi_{\mathbf{k}'}(\mathbf{r})\}$ (amplitudes $\{\psi_{\mathbf{k}'}\}$) where each wave function is a Bloch function given by Bloch's theorem: $\Psi_{\mathbf{k}'}(\mathbf{r}) = u(\mathbf{r})e^{i\mathbf{k}'\cdot\mathbf{r}}$, where k' is a spatial wave vector including the electron wave vector, $\mathbf{k}$, as well as a contribution from the periodic lattice, and $u(\mathbf{r})$ is a function with the same periodicity as the lattice. This representation is based on the periodic potential of ideal crystals and the Bloch

[4]Multiple diffraction events means that once electrons have been scattered from the direct beam, they are diffracted again, either to a new diffracted beam or back to the direct beam.

functions are eigenfunctions for the crystal. The amplitudes are also constant, and the representation is therefore suited for dealing with electron propagation inside the material. The total wave function in either representation is then a weighted sum of the wave function amplitudes combined with a phase factor, which make up the basis.

The Schrödinger equation in the crystal has the following form, with E as the acceleration voltage of the electron, $V(\mathbf{r})$ as the electrostatic potential and the wave vector $\mathbf{k}$:

$$-\frac{\hbar^2}{2m}\nabla^2\Psi(\mathbf{r}) + V(\mathbf{r})\Psi(\mathbf{r}) = E\Psi(\mathbf{r}), \quad \frac{\hbar^2 k^2}{2m} = E \tag{2.16}$$

Both the wave function and the potential energy should follow the periodicity of the lattice, and it is therefore useful to represent them using the Fourier series and the reciprocal lattice vectors, $\mathbf{g}$:

$$V(\mathbf{r}) = \sum_{\mathbf{g}\neq 0} U_{\mathbf{g}}\, e^{i\mathbf{g}\cdot\mathbf{r}} + U_0 \tag{2.17}$$

$$\Phi(\mathbf{r}) = \sum_{\mathbf{g}} \phi_{\mathbf{g}}(z)\, e^{i(\mathbf{g}+\mathbf{k})\cdot\mathbf{r}} \tag{2.18}$$

U_0 is the average potential energy of the lattice[5], and $U_{\mathbf{g}}$ and $\psi_{\mathbf{g}}$ are the Fourier coefficients for the crystal potential and the wave function (in the beam representation). The latter depends on the distance, z, into the material because the energy moves from the direct beam to the diffracted as the electrons go deeper into the material. In addition, once the electron enters the solid they experience the average potential energy and thus the kinetic energy changes, which can be represented by replacing the wave vector $\mathbf{k}$ with a modified χ. Using energy conservation, we find that $E_{solid} - E_{vacuum} = U_0$ with the formula for E_{vacuum} as in equation 2.16. Inserting the Fourier series into the Schrödinger equation along with a modified wave vector, we are left with:

$$\begin{aligned}\sum_{\mathbf{g}} \left((k_x + g_x)^2 + (k_y + g_y)^2 + k_z^2 - \chi^2 + \frac{2m}{\hbar^2}U_0) \right) \phi_{\mathbf{g}}(z) e^{i(\mathbf{k}+\mathbf{g})\cdot\mathbf{r}} \\ - \sum_{\mathbf{g}} \left(2ik_z \frac{\partial^2 \phi_{\mathbf{g}}}{\partial z^2} \right) e^{i(\mathbf{k}+\mathbf{g})\cdot\mathbf{r}} + \frac{2m}{\hbar^2} \sum_{\mathbf{g}'} \sum_{\mathbf{g}''} \phi_{\mathbf{g}'}(z) e^{i(\mathbf{k}+\mathbf{g}')\cdot\mathbf{r}}\, U_{\mathbf{g}''}\, e^{i\mathbf{g}''\cdot\mathbf{r}} = 0\end{aligned} \tag{2.19}$$

Next, the equation can be simplified by multiplying all terms with a factor of $\exp(-i(\mathbf{k}+\mathbf{g})\cdot\mathbf{r})$ and integrating over all space. All the terms in the sum will go to zero except the case where exponent is equal to the exponent in the multiplied factor. Shortening the equation further by using energy conservation, $k^2 - \chi^2 = 2mU_0/\hbar^2$ and obtain:

$$(2k_x g_x + g_x^2 + 2k_y g_y + g_y^2)\phi_{\mathbf{g}} - 2ik_z \frac{\partial \phi_{\mathbf{g}}}{\partial z} - \frac{\partial^2 \phi_{\mathbf{g}}}{\partial z^2} + \frac{2m}{\hbar^2} \left(\sum_{\mathbf{g}'\neq\mathbf{g}} \phi_{\mathbf{g}'}(z) U_{g-g'} \right) \tag{2.20}$$

[5]This is a negative value due to the positive ion cores, indicating that the electrons experience an attractive potential and therefore speeding them up inside the crystal.

The summation goes over all g' unless $g - g'$ goes to zero (that is the average potential energy U_0), and the term inside the summation goes to show how the crystal potential "mixes" up the different beams. Alternatively, the summation couples pairs of beams with a strength depending on the Fourier coefficients of the crystal potential. Furthermore, by assuming that the Fourier coefficients changes slowly with the distance into the material, the double derivative can be ignored and the result is a differential equation for each of the beams, diffracted and direct:

$$\frac{\partial \phi_{\mathbf{g}}}{\partial z} = i\left(\frac{k_x^2 - (k_x + g_x)^2 + k_y^2 - (k_y + g_y)^2}{2k_z}\right)\phi_{\mathbf{g}} - \frac{i2m}{\hbar^2 2k_z}\left(\sum_{\mathbf{g}' \neq \mathbf{g}} \phi_{\mathbf{g}'}(z) U_{g-g'}\right) \tag{2.21}$$

This is then a set of coupled differential equations (one for each $\mathbf{g}$) for the beam amplitudes, derived with only a few assumptions from the Schrödinger's equation, but separated into multiple equations. Furthermore, two key parameters, the extinction distance, $\xi_{\mathbf{g}-\mathbf{g}'}$, and the deviation parameter, $s_{\mathbf{g}}$, are defined as:

$$\frac{1}{\xi_{\mathbf{g}-\mathbf{g}'}} = -\frac{2m}{\hbar^2 k_z} U_{\mathbf{g}-\mathbf{g}'}\,, \quad s_{\mathbf{g}} = \frac{k_x^2 - (k_x + g_x)^2 + k_y^2 - (k_y + g_y)^2}{2k_z} \tag{2.22}$$

The deviation parameter introduced here is the same as in equation 2.8, except here it is explained in terms of equations. Both the extinction and deviation parameter will be reappear in section 2.2.4 as they are central to contrast effects. With these two parameters, equation 2.21 can be rewritten on a simpler form:

$$\frac{\partial \phi_{\mathbf{g}}}{\partial z} = i s_{\mathbf{g}} \phi_{\mathbf{g}}(z) + \sum_{\mathbf{g} \neq \mathbf{g}'} \frac{i}{2\xi_{\mathbf{g}-\mathbf{g}'}} \phi_{\mathbf{g}'}(z) \tag{2.23}$$

This set of equations for each beam are the dynamical coupling equations, or the "Howie-Whelan-Darwin" equations for dynamical diffraction. These form the central idea for diffraction without strict assumptions like the kinematic assumption, and are the most handy to use for simulations. These equations are however too complicated to be solved by hand, so the next point is to extract the central idea and relate to known cases.

Kinematic Diffraction

To relate equation 2.23 to the much simpler kinematic diffraction of section 2.1.2 and to extract the most important dynamical effects, the equations should be simplified. The first case to consider is when the only contribution to the diffracted beams come from the direct beam (double diffraction occurs when one diffracted beam contributes to another diffracted beam). Equation 2.23 then takes the form:

$$\frac{\partial \phi_{\mathbf{g}}}{\partial z} = i s_{\mathbf{g}} \phi_{\mathbf{g}}(z) + \frac{i}{2\xi_{\mathbf{g}}} \phi_0(z) \tag{2.24}$$

Assuming that the direction beam is constant throughout the material[6], and it can be set to 1 to make the wave functions normalized. In addition, with the deviation parameter present, the different wave functions $\phi_{\mathbf{g}}$ are no longer restricted to a specific $\mathbf{g}$, but instead to $\mathbf{g} + \mathbf{s_g}$. Introducing this into the original wave function, equation 2.18, the change caused by the deviation parameter is an additional phase factor $e^{i\mathbf{s_g}z}$. The new wave function, $\psi_{\mathbf{g}} = \phi_{\mathbf{g}} e^{-i\mathbf{s_g}z}$, is then to be inserted into equation 2.24, and this equation can then be solved over a single unit cell with lattice parameter a by linearizing it:

$$\Delta\psi_{\mathbf{g}} = \frac{ia}{2\xi_{\mathbf{g}}} e^{-i\mathbf{s_g}z} \tag{2.25}$$

This is proportional to the scattering strength or structure factor defined in equation 2.13, if the deviation parameter is assumed to be zero. While this derivation only used one dimension, it can be shown that the structure factor that was derived in three dimensions can be introduced as follows using the volume V of the unit cell, Bragg angle θ and the electron wavelength λ:

$$\Delta\psi_{\mathbf{g}} = \frac{i\lambda}{2\pi V} S_{\mathbf{g}} e^{i\mathbf{s_g}z}, \quad S_{\mathbf{g}} = \frac{\pi V cos(\theta_B)}{\lambda \xi_{\mathbf{g}}} \tag{2.26}$$

Furthermore, the equation can be generalized to include other unit cells in a column by summing over them with different values for z. This equation is however the general kinematic diffraction equation, although derived through the use of the deviation and extinction parameters instead of the Ewald sphere and structure factor. By doing so, the derivation becomes more cumbersome, but also give more insight into the physical origin of the parameters.

Multi-Beam Theory of Diffraction

Equation 2.23 shows the general outline of dynamical diffraction, and the most convenient way of solving the problem is by rewriting it to a matrix problem:

$$\frac{\partial \underline{\phi}(z)}{\partial z} = i\underline{\mathbf{A}}\underline{\phi}(z), \quad \underline{\mathbf{A}} = \begin{bmatrix} 0 & \frac{1}{2\xi_{-\mathbf{g}}} & \frac{1}{2\xi_{-\mathbf{2g}}} & \cdots \\ \frac{1}{2\xi_{\mathbf{g}}} & s_{\mathbf{g}} & \frac{1}{2\xi_{-\mathbf{g}}} & \cdots \\ \frac{1}{2\xi_{\mathbf{2g}}} & \frac{1}{2\xi_{\mathbf{g}}} & s_{\mathbf{2g}} & \cdots \\ \vdots & \vdots & \vdots & \ddots \end{bmatrix} \tag{2.27}$$

The solution is then on the form:

$$\underline{\phi}(z) = e^{i\underline{\mathbf{A}}z}\underline{\phi}(0) \tag{2.28}$$

The incident wave vector, $z = 0$, is simply the direct beam (all the other beams are zero), while the beam at $z = t$ is the outgoing wave leaving the specimen. To solve this problem, there are two widely used approaches: the Bloch wave method and the multislice

[6]This is a good approximation for thin materials, where the direct beam is much stronger than the diffracted and can be approximated to 1 throughout the process.

method. The multislice method consists of dividing the specimen into multiple segments of thickness Δz and approximating the solution at each segment. Mathematically, this is equivalent of rewriting equation 2.28 into:

$$e^{i\underline{\mathbf{A}}z} = [e^{i\underline{\mathbf{A}}\Delta z}]^n \tag{2.29}$$

Since the matrix $\underline{\mathbf{A}}$ consists of the deviation parameter and the extinction parameter, both available from the crystal potential and orientation of the sample, the matrix can be found. It is also common to separate the diagonal and off-diagonal elements, as they depend on the deviation parameter and the extinction parameter, respectively. One advantage of the multislice method is that it allows for separating segments of the specimen containing different structure. For instance if a defect is present, it can be considered by using segments with a different matrix $\underline{\mathbf{A}}$ at the location of the defect while using the matrix for perfect crystal elsewhere. The multislice method is the most widely used mainly due to its efficiency, scaling with the number of beams included as $N\,log(N)$, but the Bloch wave method is more accurate with more computations, scaling as N^3. The Bloch wave method takes a different approach, and diagonalizes the matrix in the Bloch wave basis to solve the equation, $\underline{\mathbf{A}} = \underline{\mathbf{PDP}}^{-1}$. Equation 2.28 can then be written as:

$$\underline{\phi}(z) = \underline{\mathbf{P}} \begin{bmatrix} e^{i\gamma^{(1)}z} & 0 \\ 0 & e^{i\gamma^{(2)}z} \end{bmatrix} \underline{\mathbf{P}}^{-1}\underline{\phi}(0) \tag{2.30}$$

where $\gamma^{(i)}$ are the eigenvalues of $\underline{\mathbf{A}}$ and the columns of $\underline{\mathbf{P}}$ are the eigenvectors. This method will be used for two- and three-beam approximations to gain insight into dynamical concepts (see the section below), and also for simulations throughout the thesis and so it will be discussed in more detail.

Bloch wave Formalism

Earlier, the wave functions for different beams, $\phi_{\mathbf{g}}$, were used to represent different modes ($\mathbf{g}$'s) of electrons propagating in the crystal. Instead, the Bloch wave formalism uses different modes using different spatial wave vectors, $\mathbf{k} + \gamma^{(i)}$. The first term is the electron wave vector, while the second term is a wave vector of the periodic potential, which is different for each Bloch wave. Furthermore, it is also common to simplify the diffraction problem by only considering the direct beam and a single diffracted beam, $\mathbf{g}$, which is called the "two-beam dynamical theory". The resulting wave function in the beam representation and the Bloch wave formalism then becomes:

$$\begin{aligned} \Phi_0(\mathbf{r}) = \frac{\phi_0(z)}{\sqrt{V}}\, e^{i\mathbf{k_0}\cdot\mathbf{r}}, \quad \Phi_{\mathbf{g}}(\mathbf{r}) = \frac{\phi_{\mathbf{g}}(z)}{\sqrt{V}}\, e^{i\mathbf{k_g}\cdot\mathbf{r}} \quad \text{(beam representation)} \\ \Psi^{(1)}(\mathbf{r}) = \frac{\psi^{(1)}}{\sqrt{V}}\, e^{i(\mathbf{k}+\gamma^{(1)}\hat{z})\cdot\mathbf{r}}, \quad \Psi^{(2)}(\mathbf{r}) = \frac{\psi^{(2)}}{\sqrt{V}}\, e^{i(\mathbf{k}+\gamma^{(2)}\hat{z})\cdot\mathbf{r}} \quad \text{(Bloch wave)} \end{aligned} \tag{2.31}$$

As both formulations constitute an orthonormal basis, a transformation between them is possible, and the relation between the two representations are as follows:

$$\underline{\phi}(z) = \underline{\mathbf{C}} \begin{bmatrix} e^{i\gamma^{(1)}z} & 0 \\ 0 & e^{i\gamma^{(2)}z} \end{bmatrix} \underline{\psi}, \quad \underline{\mathbf{C}} = \begin{bmatrix} C_0^{(1)} & C_0^{(2)} \\ C_{\mathbf{g}}^{(1)} & C_{\mathbf{g}}^{(2)} \end{bmatrix}, \quad \underline{\psi} = \begin{bmatrix} \psi^{(1)} \\ \psi^{(2)} \end{bmatrix}, \quad \underline{\phi}(z) = \begin{bmatrix} \phi_0(z) \\ \phi_{\mathbf{g}}(z) \end{bmatrix} \tag{2.32}$$

This transformation also works the opposite way by inverting the matrices, replacing $\underline{\mathbf{C}}$ with $\underline{\mathbf{C}^{-1}}$, and γ with $-\gamma$.

While the Bloch wave formalism can be used for obtaining a solution to the Schrödinger equation, the formalisms is not an intuitive description of the electron as it leaves or enters the material. The beam representation is more directly related to the diffraction pattern, thus the goal is to find the transformation matrix $\underline{\mathbf{C}}$ which relates the two representations and combine results from both representations to gain a solution. Once the transformation matrix is known, replacing $\underline{\psi}$ with the incident wave $\underline{\phi}(0)$ in the expression for $\underline{\phi}(z)$, resulting in an equation relating the incident wave and the electron wave at depth z using only a scattering matrix $\underline{\mathbf{S}}$. Using the thickness of the material, t, $\underline{\phi}(t)$ becomes the electron wave as it leaves the specimen (i.e. the outgoing wave) and the resulting relation between the incident and outgoing states becomes:

$$\underline{\phi}(t) = \underline{\mathbf{C}} \begin{bmatrix} e^{i\gamma^{(1)}z} & \dots & 0 \\ \vdots & \ddots & \vdots \\ 0 & \dots & e^{i\gamma^{(N)}z} \end{bmatrix} \underline{\mathbf{C}}^{-1} \underline{\phi}(0) = \underline{\mathbf{S}} \underline{\phi}(0) \tag{2.33}$$

This is exactly the same equation as equation 2.28, where $\underline{\mathbf{P}}$ has been replaced by the transformation matrix $\underline{\mathbf{C}}$. Using the Bloch wave representation is therefore equivalent to diagonalizing the matrix $\underline{\mathbf{A}}$. The next step is then to find the scattering matrix $\underline{\mathbf{S}}$ or $\underline{\mathbf{C}}$ using both representations and solving the Schrödinger equation. In this case, N Bloch waves are assumed to contribute to the diffraction pattern. Restricting the analysis to two and three beams is easier and can be done by hand to show the key features of the analysis. On the other hand, this approach can be used for creating simulations of diffraction, as a higher number of beams taken into consideration only improves the accuracy.

Two-beam Dynamical Diffraction

The two beam approximation restricts equation 2.23 to the direct beam and one diffracted beam, $\mathbf{g}$. The solution in the beam representation is then assumed to take the form of Bloch waves:

$$\phi_0(z) = C_0^{\gamma} e^{i\gamma z}, \quad \phi_{\mathbf{g}}(z) = C_{\mathbf{g}}^{\gamma} e^{i\gamma z} \tag{2.34}$$

Inserting this back into equation 2.23 for two beams, and the result is two equations that can give the ratio between the two amplitudes C_0^{γ} and $C_{\mathbf{g}}^{\gamma}$ and γ, which can then be found to be:

$$\gamma^{(1),(2)} = \frac{s_{\mathbf{g}}}{2} \left(1 \pm \sqrt{1 + (s_{\mathbf{g}}\xi_{\mathbf{g}})^{-2}} \right), \quad \frac{C_{\mathbf{g}}^{\gamma}}{C_0^{\gamma}} = 2\gamma\xi_{\mathbf{g}} \tag{2.35}$$

Inserting the two solutions for γ into the amplitude ratio, the result is two new equations for the ratios:

$$\frac{C_{\mathbf{g}}^{(1)}}{C_{\mathbf{0}}^{(1)}} = \xi_{\mathbf{g}} s_{\mathbf{g}} + \sqrt{\xi_{\mathbf{g}}^2 s_{\mathbf{g}}^2 + 1}\,, \quad \frac{C_{\mathbf{g}}^{(2)}}{C_{\mathbf{0}}^{(2)}} = \xi_{\mathbf{g}} s_{\mathbf{g}} - \sqrt{\xi_{\mathbf{g}}^2 s_{\mathbf{g}}^2 + 1} \tag{2.36}$$

As in equation 2.32, the requirement for transforming from the beam representation to the Bloch wave representation was that each beam could be represented by both Bloch waves with different wave vectors and coefficients. These four new coefficients will then allow the transformation as two Bloch waves using wave vectors $\gamma^{(1)}$ and $\gamma^{(2)}$ are associated with separate amplitudes, $C_{0,\mathbf{g}}^{(1,2)}$. Alternatively, the eigenvectors and eigenvalues of $\underline{\mathbf{A}}$ can be found to gain the same information, by solving the equation:

$$\underline{\mathbf{A}}\mathbf{C} = \gamma\mathbf{C} \quad \text{or} \quad \begin{bmatrix} 0 & \frac{1}{\xi_{-\mathbf{g}}} \\ \frac{1}{\xi_{\mathbf{g}}} & s_{\mathbf{g}} \end{bmatrix} \begin{bmatrix} C_0^{\gamma} \\ C_{\mathbf{g}}^{\gamma} \end{bmatrix} = \gamma \begin{bmatrix} C_0^{\gamma} \\ C_{\mathbf{g}}^{\gamma} \end{bmatrix} \tag{2.37}$$

However, only ratios are found so far and the last part is then to apply the boundary conditions and normalization requirement to find the values for each coefficient separately. First, a dimensionless extinction distance β is introduced to simplify the problem, $\beta = cot^{-1}(s_{\mathbf{g}}\xi_{\mathbf{g}})$. This rewriting along with some algebraic tricks, transforms equation 2.36 into:

$$\frac{C_{\mathbf{g}}^{(1)}}{C_0^{(1)}} = cot(\beta/2)\,, \quad \frac{C_{\mathbf{g}}^{(2)}}{C_0^{(2)}} = -tan(\beta/2) \tag{2.38}$$

The individual coefficients can then be easily found:

$$C_0^{(1)} = sin(\beta/2)\,, \quad C_0^{(2)} = cos(\beta/2)\,, \quad C_{\mathbf{g}}^{(1)} = cos(\beta/2)\,, \quad C_{\mathbf{g}}^{(2)} = -sin(\beta/2) \tag{2.39}$$

It can also be confirmed that they satisfy the normalization condition: $|C_{\mathbf{g}}^{(1)}|^2 + |C_{\mathbf{g}}^{(2)}|^2 = 1$, and likewise for direct beam. Although these coefficients can be inserted directly into the scattering matrix, omitting the Bloch wave formalism, it is instructive to show why it is a vital part of the derivation. The boundary conditions on the incident wave is that the amplitude of the diffracted beam is zero, while the direct beam is 1. This gives an expression for the Bloch waves:

$$\underline{\psi} = \begin{bmatrix} e^{-i\gamma^{(1)}z} & 0 \\ 0 & e^{-i\gamma^{(2)}z} \end{bmatrix} \underline{\mathbf{C}}^{-1} \begin{bmatrix} \phi_0(z=0) \\ \phi_{\mathbf{g}}(z=0) \end{bmatrix} = \begin{bmatrix} sin(\beta/2) \\ cos(\beta/2) \end{bmatrix} \tag{2.40}$$

The key behind using the Bloch wave formalism was mentioned in the beginning of the section on dynamical theory, and that is the fact that Bloch waves have constant amplitudes through the material. This allows the outgoing wave to be set equal to the Bloch waves in equation 2.40, with the transformation in equation 2.32:

$$\underline{\phi}(z) = \underline{\mathbf{C}} \begin{bmatrix} e^{i\gamma^{(1)}z} & 0 \\ 0 & e^{i\gamma^{(2)}z} \end{bmatrix} \underline{\psi} = \begin{bmatrix} sin^2(\beta/2)e^{i\gamma^{(1)}z} + cos^2(\beta/2)e^{i\gamma^{(2)}z} \\ sin(\beta)(e^{i\gamma^{(1)}z} - e^{i\gamma^{(2)}z}) \end{bmatrix} \tag{2.41}$$

Using the expressions for $\gamma^{(1)}$ and $\gamma^{(2)}$ from equation 2.35, the resulting wave function of the outgoing electron in the beam representation can be expressed entirely on the deviation parameter and the extinction parameter. However, now that the wave function is found, the actual quantity of interest can also be found, namely the intensity:

$$I_{\mathbf{g}} = \frac{1}{V}\phi_{\mathbf{g}}\phi_{\mathbf{g}}^{*} = \frac{1}{V(s_{eff}\xi_{\mathbf{g}})^2} sin^2\left(s_{eff}z/2\right) , \quad s_{eff} = s_{\mathbf{g}}\sqrt{1+(s_{\mathbf{g}}\xi_{\mathbf{g}})^{-2}} = \gamma^{(1)} - \gamma^{(2)} \tag{2.42}$$

The effective deviation parameter, s_{eff}, is introduced here to simplify the expression. This expression is the dynamical diffraction in its simplest form, i.e. by only considering two beams. At the same time, it is also instructive as it shows how the intensity can vary for a single diffracted beam depending on the effective deviation parameter and the thickness alone.

Two-beam Dynamical Diffraction with Weak Beams

As more beams are included, the problem becomes more complicated and the matrix formulation as in equation 2.37 is needed. Generally, for three beams, **o**, **g** and **h** (**o** being the direct beam), equation 2.33 gives the solution and the eigenvectors and eigenvalues are found by diagonalizing $\underline{\mathbf{A}}$:

$$\begin{bmatrix} 0 & \frac{1}{2\xi_{-\mathbf{g}}} & \frac{1}{2\xi_{-\mathbf{h}}} \\ \frac{1}{2\xi_{\mathbf{g}}} & s_{\mathbf{g}} & \frac{1}{2\xi_{\mathbf{g}-\mathbf{h}}} \\ \frac{1}{2\xi_{\mathbf{h}}} & \frac{1}{2\xi_{\mathbf{h}-\mathbf{g}}} & s_{\mathbf{h}} \end{bmatrix} \begin{bmatrix} C_{\mathbf{o}} \\ C_{\mathbf{g}} \\ C_{\mathbf{h}} \end{bmatrix} = \gamma \begin{bmatrix} C_{\mathbf{o}} \\ C_{\mathbf{g}} \\ C_{\mathbf{h}} \end{bmatrix} , \quad |\underline{\mathbf{A}} - \gamma\underline{\mathbf{I}}| = 0 \tag{2.43}$$

The determinant finds the eigenvalues, but the resulting cubic equation is too complicated to extract interesting features of the three-beam case. To avoid dealing with this equation, the problem of multiple beams can be simplified in one of two ways. The first is to restrict the analysis to crystals with specific symmetry like centrosymmetry where the solution can be found exactly, while the other method is to treat the third beam, **h**, through perturbation theory while assuming its contribution is weak compared to **o** and **g**. Since the main interest of the thesis is non-centrosymmetric crystals, symmetry can not be restricted so the only approximation of interest is through perturbation theory.

The key assumption for regarding a beam, **h**, as "weak" is that its diagonal term of the matrix above is much larger than off-diagonal elements of other beams, $s_{\mathbf{h}} >> \left|\frac{1}{2\xi_{\mathbf{g}}}\right|$. Likewise, $s_{\mathbf{g}}$ must be comparable with $\left|\frac{1}{2\xi_{\mathbf{g}}}\right|$ to be treated as a strong beam. Assuming the system has only two strong beams, but many weaker beams, matrix multiplication of the matrix above yields the following equation for the coefficients $C_{\mathbf{h}}$:

$$C_{\mathbf{h}} = \frac{\sum_{\mathbf{h}-\mathbf{h}'} C_{\mathbf{h}'}/2\xi_{\mathbf{h}-\mathbf{h}'}}{s_{\mathbf{h}} - \gamma} \approx -\frac{C_{\mathbf{o}}/2\xi_{\mathbf{h}} + C_{\mathbf{g}}/2\xi_{\mathbf{h}-\mathbf{g}}}{s_{\mathbf{h}}} \tag{2.44}$$

The initial matrix with the solution can then be reduced from a 3x3 matrix to a 2x2

matrix and the solution comes from a quadratic equation instead of a cubic:

$$\begin{bmatrix} s_{\mathbf{o}}^{eff} - \gamma & \frac{1}{2\xi_{-\mathbf{g}}^{eff}} \\ \frac{1}{2\xi_{\mathbf{g}}^{eff}} & s_{\mathbf{g}}^{eff} - \gamma \end{bmatrix} = \begin{bmatrix} C_{\mathbf{o}} \\ C_{\mathbf{g}} \end{bmatrix} \tag{2.45}$$

with effective parameters defined as:

$$s_{\mathbf{g}}^{eff} = s_{\mathbf{g}} - \sum_{\mathbf{h}} \frac{1}{s_{\mathbf{h}}|\xi_{\mathbf{g}-\mathbf{h}}|^2}\,, \quad s_{\mathbf{o}}^{eff} = -\sum_{\mathbf{h}} \frac{1}{s_{\mathbf{h}}|\xi_{\mathbf{h}}|^2}\,, \quad \frac{1}{2\xi_{\mathbf{g}}^{eff}} = \frac{1}{2\xi_{\mathbf{g}}} - \sum_{\mathbf{h}} \frac{1}{4 s_{\mathbf{h}} \xi_{\mathbf{h}} \xi_{\mathbf{h}-\mathbf{g}}} \tag{2.46}$$

By introducing the effective parameters, the results from the two-beam case above remain with only an exchange of parameters. With these new parameters, equation 2.42 are modified to:

$$I_{\mathbf{g}}(t) = \frac{1}{V|2\xi_{\mathbf{g}}^{eff}|^2\omega^2} sin(wz/2)\,, \quad \omega = \sqrt{\left(s_{\mathbf{g}}^{eff} - s_{\mathbf{o}}^{eff}\right)^2 + \frac{1}{|2\xi_{\mathbf{g}}^{eff}|^2}} \tag{2.47}$$

The effect of adding weak beams to the two-beam theory leads to two new effects. In the two-beam case, the term inside the sine function had a maximum for $s_{\mathbf{g}} = 0$. This is no longer the case as it is shifted due to the effect of weak beams through $s_{\mathbf{o}}$. In addition, the extinction parameter now depends on the orientation through the deviation parameter. In conclusion, it is important to realize that scattering is mainly dynamic and to predict the intensity correctly it is necessary to use dynamical theory. There are several TEM techniques that are highly sensitive to small variations in deviation parameter where simulations including dynamical theory is necessary, while other techniques can to some extent be understood by the kinematic approach alone.

2.2 Transmission Electron Microscopy

The following section is based on the book by Williams and Carter, *Transmission Electron Microscopy*[16], unless explicitly stated otherwise.

2.2.1 Introduction

Studying materials in TEM can be a time consuming effort, since specimen preparation can become difficult as the specimen must be electron transparent and are thus best below 100 nm thickness. Although not the first equipment to be used, the TEM makes it possible to gain high resolution structural detail. Besides visualizing atomic structures through imaging, diffraction and spectroscopy experiments offer even more information about the details of the sample's structure.

When the ordinary visible light microscope (VLM) uses light around with a wavelength around 550 nm, the resolution is given by the Rayleigh criterion and numerical aperture (NA), $\delta = 0.61\lambda/NA$, to be around 300 nm. Should a system posses detail below 300 nm, they would not be distinguishable in the optical microscope. In such

cases, the electron microscope is one option. The electrons have a de Broglie wavelength determined by the electron momentum, p, and the planck constant h:

$$\lambda = \frac{h}{p} \tag{2.48}$$

For electrons accelerated by 200 kV, the wavelength then becomes 0.0251 Å. The Rayleigh criterion is not used for electrons, but replaced by 1.22λ, so the fundamental resolution limit for 200 kV electrons becomes 0.0306 Å. Unfortunately, no TEM can reach this limit due to lens aberrations and instabilities.

The two main aberrations in a TEM lens is spherical and chromatic aberrations. State of the art TEM's are now equipped with a spherical aberration corrector, increasing the resolution from around 2.3 Å to sub Å at 200 kV, but chromatic aberrations can still form a limitation. The electron-optic set-up will however allow us to switch between real and reciprocal space (image and diffraction), which offer supplementary information and makes the TEM the most versatile tool for materials physics.

2.2.2 Microscope Design

The overview of the TEM and its components are shown in figure 2.4. The electron beam is created by the source, the electron gun, and accelerated down into the column. The column is where we find the lens system and specimen. The first contact the electron beam makes in the column is the condenser lenses, followed by the specimen, then the objective lens, then the intermediate lenses and lastly the projector lens. Finally, the beam enters the viewing chamber where it either hits the camera or fluorescent screen. In addition, there are three main apertures: the condenser aperture, objective aperture and selected-area aperture. An understanding of all these components, both in a theoretical and practical point of view, is essential to operating a TEM.

Electron Gun

In figure 2.5(a), a sketch of a thermionic electron gun is shown. The filament, usually made of LaB_6, is heated and the thermally excited electrons are accelerated by the large voltage difference (several hundred kV) between the cathode and anode. In addition, a small negative voltage is applied to the Wehnelt cylinder to obtain a controllable beam[7]. Another possible electron gun is the field-emission gun (FEG), where a material like tungsten is shaped into extremely sharp (radius $< 0.1\,\mu m$) needle tips. Since electric fields are inversely dependent on the size (for spherical objects), the electric field strength at the tip ensures that the tunnelling barrier is lowered enough to emit an electron beam. It's worth noting that the gun cross-over in figure 2.5(a) can be shifted up or down by increasing or decreasing the lens focusing power of the Wehnelt cylinder to reduce or increase the beam intensity, referred to as the spot size.

[7]Since the Wehnelt cylinder causes the beam to converge, it is in reality the first electron lens in a TEM.

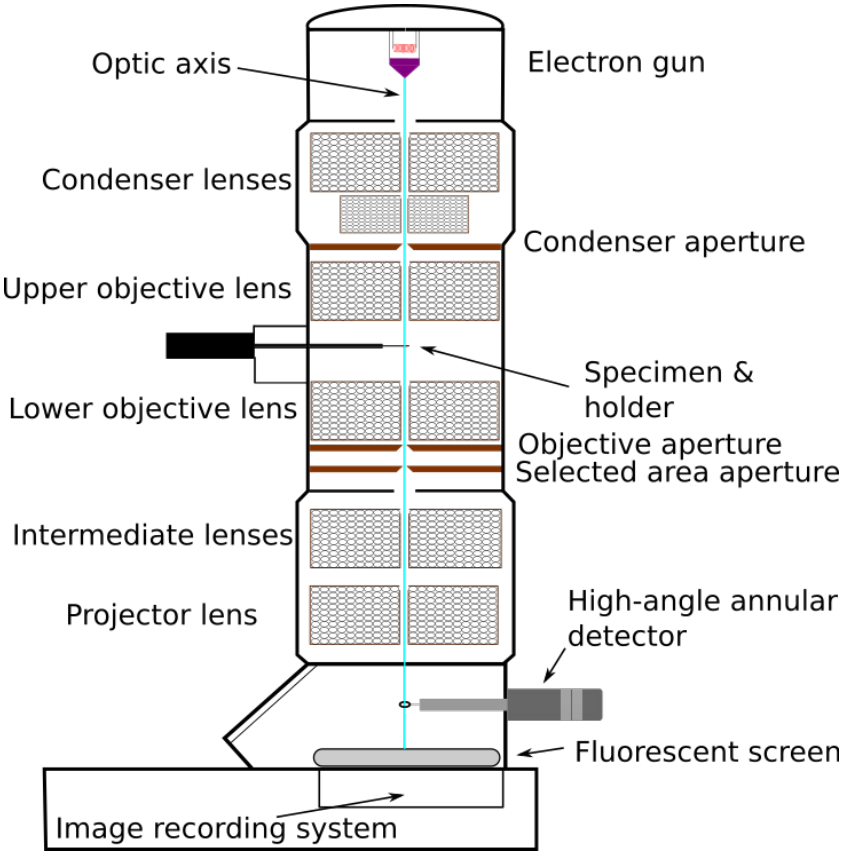

Figure 2.4: Schematic of a TEM column with major components labelled.

Electron Lenses

The general function of any lens is to either focus or disperse a beam that passes through it, in a controllable way. In the case of optical light, convex transparent medium with a refractive index larger than that of vacuum is used to focus the beam. For electrons however, the lens is several electromagnetic coils and the lens is only converging.

A current is sent through the coils, causing a magnetic field to surround them. Placing several of them tightly together, like in figure 2.5(b), makes it possible to create a uniform magnetic field (only varied by distance from optical axis). The electrons passing by will either be attracted or repulsed depending on the direction of the current. In the figure, a focusing lens is showed where the magnetic field is weakest at the optical axis, and increases in strength when moving towards the sides of the pole piece. The repulsive force on the electrons therefore increases as they move further away from the optical axis, and thus focuses the beam. In order to keep the magnetic field contained to only a small gap, they are contained in an iron cylinder (pole piece) with a hole (bore) through the optical axis.

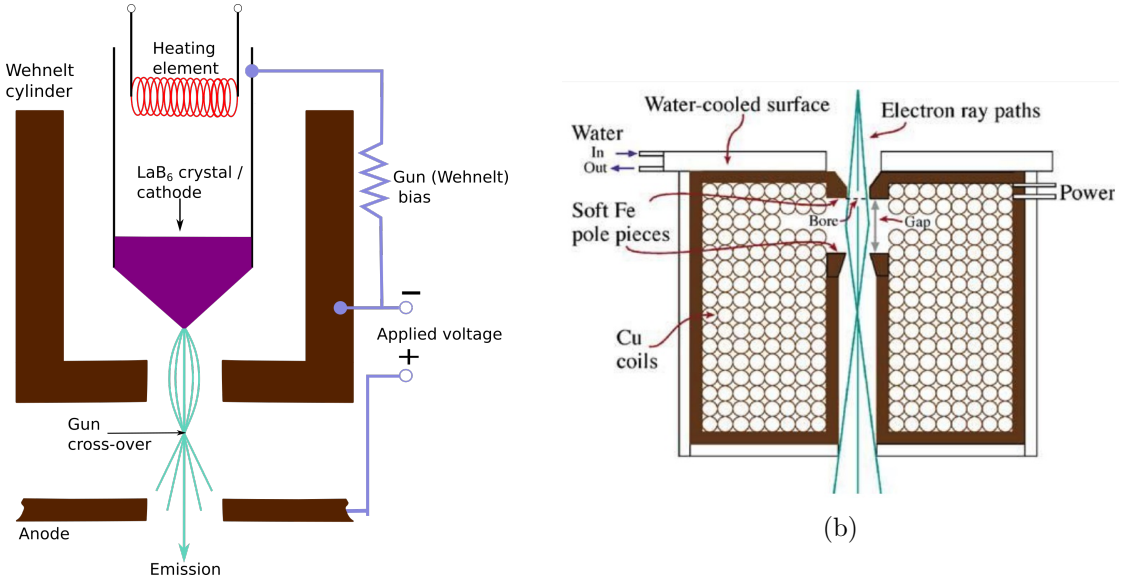

Figure 2.5: (a) Schematic of a thermionic electron gun. Image is adapted from [16]. (b) Schematic of an electron lens. Image is taken from [16]

TEM operation

The microscope is assembled by a combination of optical elements divided into three segments: the illumination system, the objective lens/stage and the imaging system. Each segment consists of lenses and an aperture, and can be described by a single function or purpose. In addition, pairs of deflection coils are used to tilt and shift the beam, and a stigmator is used to control the roundness of the beam (not included in figure 2.4). Figures 2.10 and 2.6 shows the major components in action, using different lens strengths and apertures to control the beam and operation through the column, starting from the top.

The first component is the illumination system (condenser part), responsible for taking the electrons from the gun to the specimen in a broad (parallel) or focused (convergent) beam with a convergence angle α. This is illustrated in figure 2.6, where the condenser lenses C1 and C2 and the upper objective lens (sometimes called C3 or c/o) combine to illuminate the specimen. The first condenser lens controls the spot size of the beam by determining how much of the beam should be sent to C2. This lens controls the brightness/convergence of the beam. The upper objective lens combined with C2 makes it possible to use the same convergence angle with different probe sizes, useful for convergent beam techniques (see section 2.2.5). A condenser mini-lens (not included in figure 2.4) is sometimes used to improve the parallelism of the beam. In addition, an aperture (a hole in the diaphragm) called the condenser aperture is inserted as well to make the improve the beam quality (shape, aberrations) at the cost of intensity. This

aperture (and all the others) is simply a metal plate, usually made from Pt or Mo, with a circular hole in the center.

The objective lens and stage is the heart of the TEM. The upper objective lens is located above to control the illumination. The holder containing the specimen is inserted below, and the lower objective lens is positioned below the specimen. The (lower) objective lens collects the electrons emitted from the specimen, and form the DP at the back focal plane (BFP) where the objective aperture can be placed. This aperture can be used to select certain diffraction spots, for dark-field (DF) or bright-field (BF) imaging (see section 2.2.5). Further down the optical axis, the image plane is found at the intermediate stage, where the selected area diffraction (SAD) aperture is placed. Since this is the image plane, of the objective lens the aperture selects out a virtual area of the image that is used to create a DP. The spherical aberration comes into play here (see section below).

The last component is the image system. It consists of the intermediate lenses and the projector lens, and the purpose of these is to magnify the objective plane of the intermediate lens onto the screen. The strength of the intermediate lenses will then decide whether the DP or image plane should be displayed on the screen as displayed in figure 2.10, and it is possible to switch between the two operations using only a single button. In practice, this switching and the large range of magnification is accomplished by using three intermediate lenses instead of one. Instead of a fluorescent screen a charge-coupled device (CCD) camera are sometimes used allowing image processing to capture more details.

Aberrations

The spherical aberration comes as result of lenses focusing rays differently depending on their distance from the optical axis. The rays closest to the center (optic axis) are focused more strongly than the rays further away from the optical axis. The effect is that points in the image plane of the objective lens becomes distorted and spread over a spherical disk instead of a point. When the large spread is magnified by the imaging system, the picture is more blurred than it could have been. To reduce this spread in focus point, an aperture is inserted, limiting the angular spread. However, see section 2.2.1, this is equivalent to reducing the NA and thereby the ultimate diffraction limited resolution. The radius of the disk resulting from the spread at point of minimum distortion is:

$$r_{sph} = C_s \beta^3 \tag{2.49}$$

The β is the maximum angle of collection while the C_s is a constant called the aberration constant. The lens specific C_s can be partly countered by defocussing. By working at a slight under focus, called Scherzer defocus, a higher resolution can be obtained. By resolution the point resolution is meant, up to which detail can be directly interpreted. Beyond this point the contrast vary and image simulations are required to interpret the contrast. A modern TEM can have a C_s corrector, in which non-round lenses are used that induce other aberrations that balance the Cs (effectively control it). Still the total object lens characteristics like aberrations determine the final obtainable resolution.

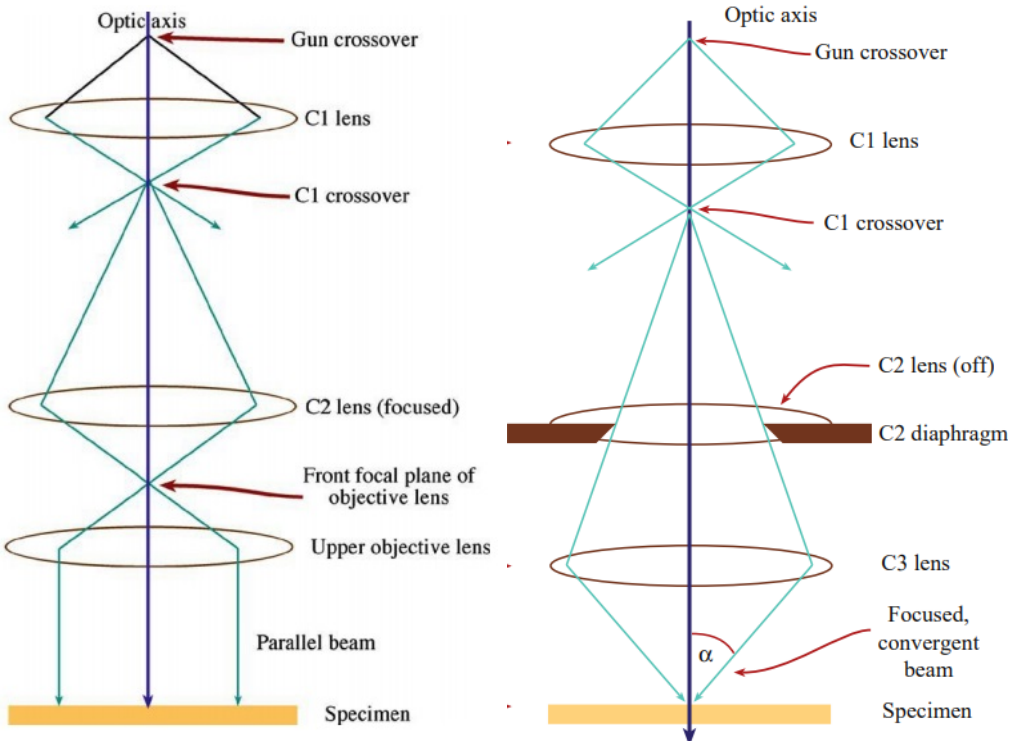

(a) (b)

Figure 2.6: Schematic of two modes in TEM. (a) The TEM in parallel beam mode, used to illuminate the whole specimen simultaneously. (b) The TEM in convergent beam mode, used to illuminate ony a small portion of the sepcimen. Images is taken from [16].

The other lens imperfection that also degrades the final resolution is the chromatic aberration. This aberration is smaller than the spherical aberration, but if the TEM is C_s corrected then this is the next limitation. While the electron beam are set to a certain energy, it is not monochromatic[8]. In the same way as the lenses focus the rays differently depending on the distance from the optical axis, they also focus differently depending on the electron energy. Lower energy electrons are focused more strongly than the higher energy electrons. The points in the image plane becomes disks with a radius:

$$r_{chr} = C_c \frac{\Delta E}{E_0} \beta \tag{2.50}$$

ΔE is the variation in beam energy E_0 and C_c is the chromatic aberration constant. The difference in beam energy becomes larger as the specimen becomes thicker, and the aberration increases as well. It is also worth noting that this aberration is proportional to β, while the spherical aberration is proportional to β^3. Reducing the maximum collection angle is therefore far more effective at reducing spherical aberration than

[8]For a 200 kV FEG, the variation of the beam energy is usually smaller than 1 eV.

chromatic aberration.

Another lens imperfection that works differently than the two above, but also must be corrected for is astigmatism. The effect is that the beam becomes elliptical instead of round. Two causes for this arises in the pole pieces in the lenses which can be asymmetrical, and microstructural variations in the soft-iron cause local magnetic field. Apertures can also cause astigmatism if they are not centered perfectly on the optic axis, or if they are not clean and contamination deflects the beam. Astigmatism is however easy to adjust for, by installing stigmators (octopoles) which introduce compensating fields to adjust the beam shape.

2.2.3 Electron Interaction

When electrons hit with the specimen the interaction can be either elastic (keep energy) or inelastic (loose energy). The elastic scattering[9] are described by the general theory in section 2.1.2 and is similar to the treatment of photons. This scattering is the main interaction for thin samples and high energy, and the main signal for DP's and imaging. The inelastic interaction is however more intriguing, as it can result in a numerous processes. Figure 2.7 shows the signals produced from electron-specimen interaction that is used in this thesis, although only a few is used in TEM. These are the elastically and inelastically scattered electrons indicated in red that are transmitted through the specimen. The coherent elastic signals are the main source in conventional TEM, while the incoherent electrons are used in scanning TEM (section 2.2.6). The difference lies in the wave nature of the electrons, where coherently scattered electrons are in phase with each other whilst the incoherently scattered electrons is not. In addition to transmission, electrons can also be reflected or backscattered, and be generated inside the specimen as ionization products and emitted as secondary electrons. Both of these are important for the scanning electron microscope (section 2.3). Characteristic X-ray signals indicated in green are also generated and can be used for compositional analysis by energy or wavelength dispersive spectroscopy. It varies from specimen to specimen when the different signals should be considered, but some points can be made. Since inelastic scattering often include several scattering events, it is heavily dependent on the thickness of the specimen. The same goes for backscattered electrons; they are more likely as the specimen becomes thicker or the beam energy becomes weaker. This implies that thin specimen will generate more elastic and less inelastic scattering than the thicker counterparts.

Elastic scattering of electrons

Since the electron is an negatively charged particle, it scatters on all the electric fields of the atoms. These originate in either the large electron clouds or the tightly bound nucleus, and the closer to the nucleus the electrons gets the stronger it will be scattered. Thus, low-angle scattering ($<3^\circ$) is due to electron-cloud scattering while the higher

[9] All interaction between electrons and specimen is called scattering, but we reserve the term diffraction for the elastic interaction when $\mathbf{G} = \Delta k$

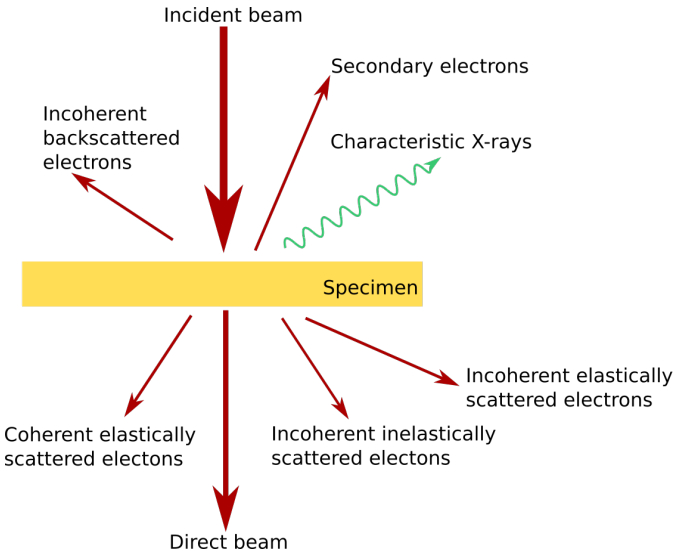

Figure 2.7: The signals produced by electron scattering used in this thesis. The signals indicated in red are electrons while the green signal is X-rays.

angle scattering is due to electron-nucleus interaction. Returning to the theory in section 2.1.3, to describe the scattering of a single atom the atomic form factor is used. Taking both the electron cloud and nucleus into account and using the total electrostatic potential as the scattering density, the atomic form factor can be showed to have the following form:

$$f(\theta) = \frac{\left(1 + \frac{E_0}{m_0 c^2}\right)}{8\pi^2 a_0} \left(\frac{\lambda}{sin\frac{\theta}{2}}\right)^2 (Z - f_x) \tag{2.51}$$

Where E_0 is the beam energy, m_0 is the mass of the electrons, c is the speed of light, a_0 is the Bohr radius, λ is the electron wavelength and θ is the scattering angle. The last term is the difference between nucleus attraction and cloud repulsion, where Z is the atomic number and f_x is the scattering factor for X-rays as in equation 2.12 with the electron density as the scattering density. This equation is called the Mott-Bethe formula, derived from fundamental quantum mechanical principles using the Born approximation. In this case, the scattering problem can be solved from the Schrödinger equation by only considering the incident and outgoing electron waves. The Born approximation then assumes that a first-order solution in perturbation theory is sufficient. Two important predictions from this equation is that the scattering strength will decay for increasing angles, and that heavier elements scatter more strongly than light elements. While the dynamical theory in section 2.1.4 gives a thorough understanding of the processes that form intensity into distinct reflections owing to the crystal structure, equation 2.12 gives insight to scattering at the atomic level. Combined, these two sections completes the picture for elastic diffraction.

Inelastic scattering of electrons

As illustrated in figure 2.7, inelastic interactions give rise to important effects from the electron-specimen interaction. The processes can be categorized into X-ray generating processes, processes that generate other electrons and processes due to collective interactions with multiple atoms. The X-rays are either Bremsstrahlung X-rays (white or continuous) or characteristic X-rays, and the latter are the most relevant for this work. Energy-dispersive X-ray spectroscopy (EDX) is possible through these characteristic X-rays, and EDX is a routinely used spectroscopy technique. The incoming electron, with more than sufficient energy, can ionize an atom in the the sample by transfer a core electron (say K shell). This hole is filled by an electron from a higher shell (L or M). The energy difference between the two levels can then be released as an X-ray with the same energy. Hence by measuring that energy the wavelength is also found:

$$\lambda = \frac{hc}{E} \tag{2.52}$$

With the planck's constant h and speed of light c known, the X-ray wavelengths are characteristic for atoms by only depending the interatomic transition energies E, and thus allows the specific transition or atom to be identified.

2.2.4 Image Contrast and Defects

Contrast

The lenses under the BFP convert the intensity variations in the BFP to intensity variation in the recording plane. Interpreting the contrast within an image is extracting the information on the sample, but to interpret the contrast it must be understood. Contrast can be defined as the relative difference in intensity between two areas[10]:

$$C = \frac{\Delta I}{I} \tag{2.53}$$

Furthermore, TEM image contrast can be divided into two categories: phase contrast and amplitude contrast. Both types contribute to images at all times, but the specific techniques used often tend to favour one type of contrast. Combining different forms of contrast by combining different imaging techniques can then give a better understanding of the sample studied. Phase contrast is the basis for HRTEM imaging, while the amplitude contrast is important for interpreting BF and DF images, where basically a single beam is selected by the aperture in the BFP. The amplitude contrast can then be divided further into diffraction contrast and mass-thickness contrast.

The mass-thickness contrast is formed by incoherent elastic scattered electrons. This type of scattering is heavily dependent on the atomic number and the thickness of the sample, and is confined to small angles ($< 5°$). It depends on thickness simply because a thicker specimen (and heavy elements) will scatter more than a thin specimen (and light

[10]Later in the thesis when this equation is be used it will be expressed in percentage.

elements). If an objective aperture is used, scattering is on average outside the aperture opening and the BF image will appear dark. Mass-thickness contrast is always present, but only the dominant contrast form in amorphous specimens.

Diffraction contrast are due to the structural considerations presented in section 2.1.2. This elastic coherent scattering governed by the structure factor forms the DP, which is fixed for crystal structures and orientations. If parts of the specimen (grains, defects etc.) have different diffraction conditions, for instance orientation or d_{hkl}-spacing, than the surroundings the objective aperture can be used to exclude or include certain reflections with certain intensities when forming the image (see section 2.2.5 on DF imaging). A contrast will then form between areas depending on their diffraction conditions.

Both types of amplitude contrast are formed by intensity variations in a single beam. When both direct beam and diffracted beams are used, another contrast arises which is the phase contrast. In general, it is the contrast formed by interference between multiple beam and the interference pattern (strongly dependent on the difference in phase of the recorded wave) allows indirect visualization of the atomic structure. The simplest case is then the two-beam theory in section 2.1.4, except here it is the intensity of the total wave function of equation 2.18 that is of interest. Both direct beam and diffracted beams have their wave functions expressed by equation 2.41 in the two-beam theory, and the intensity of the total wave functions therefore becomes:

$$I = K_1(\xi_{\mathbf{g}}, s_{\mathbf{g}}) - K_2(\xi_{\mathbf{g}}, s_{\mathbf{g}}) sin(\mathbf{r} \cdot \mathbf{g} - \pi st) \tag{2.54}$$

The two K_i are complicated functions involving the deviation and extinction parameters and can be found explicitly from the equations on dynamical theory. However, the central idea of this equation is to explain variations in the plane of the specimen, not quantitative intensity measurements which would be inaccurate for realistic cases with more than two beams. Qualitatively however, it explains how two beams interfere to form fringes normal to the direction of the diffracted beam. By also including equation 2.4, it is confirmed that the fringes from equation 2.54 are separated by the distance of the atomic planes. These fringes can therefore be interpreted as atomic planes, although in reality they are only the effect of two beams interfering. Including more beams will then lead to more interference and eventually a picture that can resemble the atomic structure. By assuming that each wave is equal in amplitude, equation 2.18 can be easily be extended to the multi-beam case and the total intensity is illustrated for two, four and nine beams in figure 2.8.

The figure illustrates how multiple beams combine to form an image that can resemble the atomic structure with the same periodicity and symmetry, but with some key features not preserved. For instance, the dark crossovers for four beams could be interpreted as atoms. However, in the nine beam case these dark crossovers turn into more sharply defined bright spots. This leads to two important conclusions on phase contrast. First, more beams further out in reciprocal space leads to a higher resolution. Second, the phase contrast can not be interpreted directly since there are too many effects at play simultaneously. Adding or removing beams can have the same effect as changing the amplitudes on each beam or the frequency inside the sine function in equation 2.54.

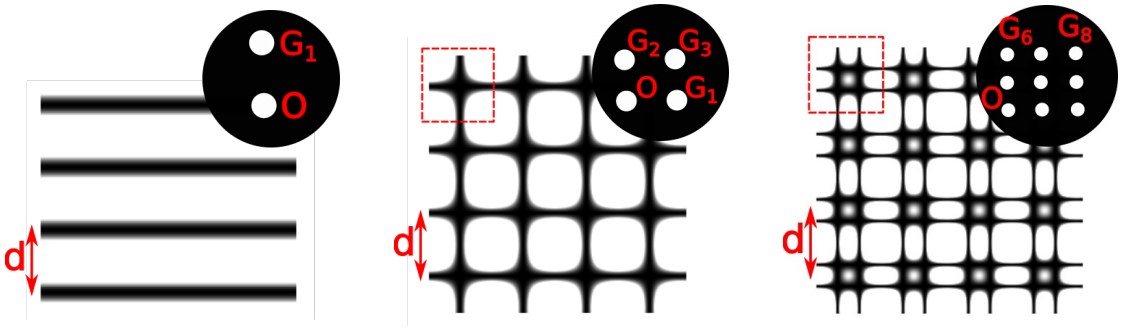

(a) (b) (c)

Figure 2.8: Simulation of interference from multiple beams with equal amplitude for a cubic crystal structure, with the selected beams in the top right corner. The distance d between fringes are the same as between atomic planes, but the crossover point (red square) change contrast depending on the number of beams involved. (a), (b) and (c) shows the case for 2, 4 and 9 beams, respectively.

This means that changing the deviation parameter, extinction distance or thickness can lead to additional interference effects. This type of contrast and the resulting effects is still vital to consider when discussing high resolution imaging later in section 2.2.5.

The contrast mechanisms explained above forms the basis for most imaging, but a final point on contrast is the occurrence on fringes. These occur frequently in crystals, and can be explained from the two-beam dynamical theory in section 2.1.4. The central idea is found by considering equation 2.42 and the definition of the extinction parameter for a material with thickness t:

$$I_{\mathbf{g}}(s,t) \sim \frac{sin^2(\pi t s_{eff})}{V(\xi_{\mathbf{g}}\pi s_{eff})^2}, \quad s_{eff} = \sqrt{s^2 + \frac{1}{\xi_{\mathbf{G}}^2}}, \quad \xi_{\mathbf{g}} = \frac{\pi V_c cos\theta_B}{\lambda S_{\mathbf{g}}} \tag{2.55}$$

These formulas predict that if the structure factor, effective deviation parameter or the thickness changes, then so does the intensity in a reflection. The result is a visible image contrast that varies as a sine function, and these fringes can hold a great deal of information. Should the material experience bending, then the reciprocal space bends and the deviation parameter as well, leading to bending fringes. This contrast can also change rapidly during tilting and is not a static effect. In addition, local strain also cause changes to the deviation parameter which also leads to similar fringes. Thickness changes has the same effect as changes in the deviation parameter and are called thickness fringes. They are a common sight in wedge shaped structures where the thickness changes linearly[11]. Both effects are illustrated in figure 2.9. Phase contrast can also give fringes not associated with atomic planes such as Moire and Fresnel contrast, but these will not be used in the rest of the report.

[11]This is also a common sight in optical microscopes in the same specimens. Light passing through the specimen at different thicknesses pick up different phases which lead to constructive and destructive interference.

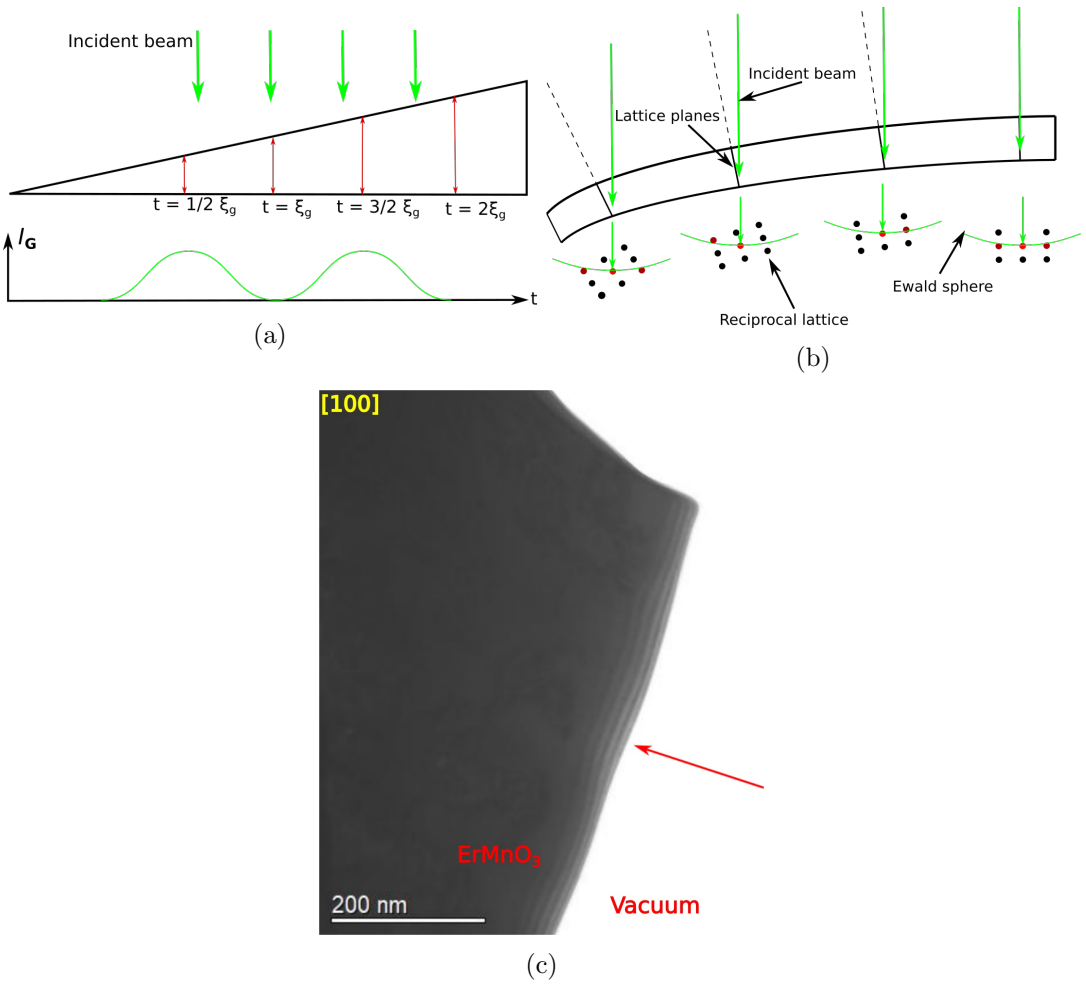

Figure 2.9: (a) Schematic of how variation in thickness due to a wedge shaped crystal causes the change in intensity in the graph below from equation 2.55. The values for the thickness assumes deviation parameter is zero. Image adapted from [16]. (b) Schematic of how bending causes change in the deviation parameter. As the lattice planes are rotated, the reciprocal lattice points are rotated out of the Ewald's sphere and the deviation parameter changes. (c) Thickness fringes in a real sample. In this case, an $ErMnO_3$ crystal which is mechanically polished into a wedge. Red arrow indicate the fringes.

Defects and their Contrast

Crystalline defects can have a considerable effect on the macroscopic properties such as mechanical strength and charge transport properties. The most important of these

defects are planar defects[12], or interfaces internal or external to the crystalline which separates two microstructures. As stated in section 2.1.1, ideal crystallines are infinite so any interface that breaks the translation symmetry must be considered a defect to the crystal. External interfaces simply means the surface of the crystal, while internal interfaces are grain boundaries, translation boundaries or phase boundaries.

The translation boundaries are the most strict class of boundaries. They require that the structure on both side of the boundaries are distinguished by a translation only. An example of this are stacking faults, where a lattice plane is shifted with respect to its neighbouring plane, or a periodic lattice stacking is abrupted. In an FCC structure, the lattice planes along the [111] direction are stacked as ABCABC, meaning structures A, B and C differ only by a translation. An interruption in this stacking order, for instance ABCAB<u>A</u>BC, is thus an example of stacking fault.

If a rotation of the structure is also allowed through the interface, the defect is called a grain boundary. Both sides of the interface must now be the same structure, but related by a shift and/or rotation with respect to each other. More generally, the grain boundary are classified into low angle and high angle groups. The low angle boundaries consists of a small rotation and multiple arrays of dislocations, while in the high angle boundaries the two grains shares several lattice sites and a reciprocal fraction of sites, Σ, is often used to describe them. This class includes the stacking fault described above, but also includes other defects such as twin boundary defects and anti-phase boundary. The twin boundary defect consist of two grains on each side of the twin that is a mirror to one another, while an anti-phase boundary is the interface when two regions are out of phase with each other. This can be a simple shift such as the stacking fault, but not necessarily confined to a single lattice plane. It can also come in the form of a 180° rotation. While not usually described as a crystallographic defect, domains in ferroelectrics (see section 2.4) are also separated by an interface called domain walls, over which a rotation takes place. In the case of $ErMnO_3$ and $Pb_5Ge_3O_{11}$, the difference between two domains consist of a 180° rotation across the domain wall or interface.

The defects described can be visualized by using a diffraction contrast in the form of fringes, making them visible in the TEM. This can occur if the defect induces strain, a local bending around a defect, giving the same effect as the bending contrast described above. If the defect is only a translation or rotation between two regions, then the contrast can be explained from the structure factor in equation 2.13. Should a region becomes distorted by a translation $\mathbf{R}$ with respect to another region, then a phase difference $\mathbf{G}\cdot\mathbf{R}$ arises inside the summation for each. Variations in the diffracted intensity or diffraction conditions leads to contrast in imaging. However, should the interface only consist of a 180° rotation like in the domain structure of $ErMnO_3$, diffraction conditions may be almost identical and not produce any contrast (see section 2.1.2 on Friedel's law). Visualizing domains may therefore require specialized TEM techniques (see section below).

Phase boundaries are the last internal interface defect. Similar to the grain bound-

[12]Point defects such as those associated with doping are also important for the properties, but challenging to detect in a TEM and not discussed further in this work.

aries, these interfaces allow for the two grains to have different orientation and also be translated with respect to each other. In addition to this, the phase boundaries also allow for different structures and/or chemistry of the two structures. This results in completely different behaviour of the two structures since they can have different reflection conditions and distances in reciprocal space. The diffraction contrast is then also different.

In addition to planar defects, line defects can be of importance. These are dislocations of the crystal structure along a line, meaning they are a translation boundary, but contained within a single column of atoms. In other words, a single lattice plane disappears or ends inside the crystal, leaving a strain field around the edge. To represent them, the burgers vectors, **b**, are often used which contain the magnitude and direction of the dislocation. It can furthermore be showed that if the burgers vector are perpendicular to a beam, **g**, then the defect will not show any contrast when selecting this beam. This can be utilized to find two distinct beams for which the defects shows no contrast, and then the vector product of the two beams is the direction of the burgers vector as well as the dislocation.

2.2.5 Conventional TEM Techniques

BF and DF Imaging

As mentioned earlier, the two basic operations of the TEM is diffraction and imaging. The switch between the modes are illustrated in figure 2.10, but it should be pointed out that the two are connected, and an understanding of both techniques is often required to perform just imaging.

When the imaging operation is wanted, the image plane of the objective lens must be magnified by the imaging system, and projected onto the screen. This is accomplished by using a strength on the intermediate lens that places the objective lens' image plane in the objective plane of the intermediate lens. While this enables the most basic technique, imaging is often divided into three more practical techniques: BF, DF and high-resolution TEM (HRTEM). Both DF and BF are techniques that uses the objective aperture to enhance the contrast of the region of interest when the details of the lattice is not of interest. Since the objective aperture remove certain diffraction spots, it will reduce the phase contrast while enhancing the amplitude contrast.

When phase contrast and lattice details is not important, the objective aperture can be used to get sharper images (more contrast) by cutting out the small signal noise from multiple reflections, which is the basic principle for BF and DF imaging. In BF, the objective aperture is centered around the central spot, allowing only a certain number of diffraction spots to be used or just the direct beam, as illustrated in figure 2.11(a). By selecting the direct beam only, phase contrast is cut out entirely and the remaining image contrast originates solely in amplitude contrast. This allows for inspection of thickness and crystal orientation separately from the phase contrast that is more difficult to interpret.

The objective aperture could also be centered around a reflection while excluding the

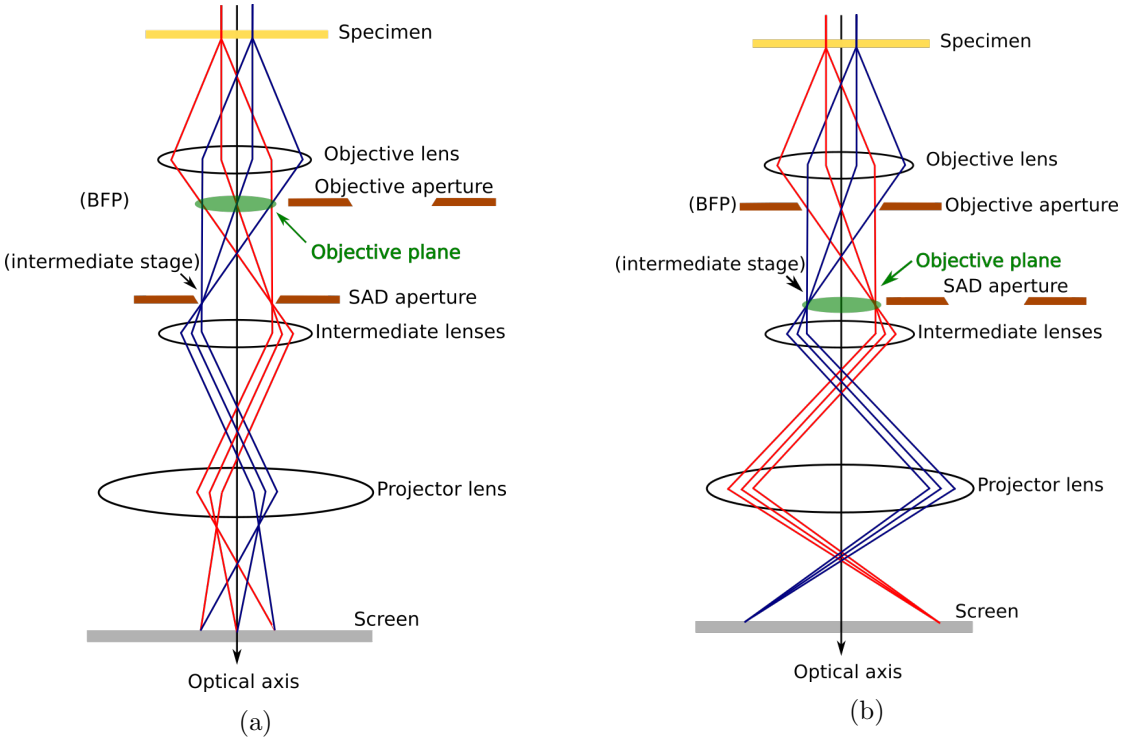

Figure 2.10: Schematic of the two basic operations in a TEM: (a) diffraction and (b) imaging. The switching is primarily due to a change in the intermediate lenses strengths. The objective plane of the intermediate lenses (green plane) is magnified to the screen, and the two modes are obtained by shifting this plane between the back focal plane and image plane of the objective lens. Different apertures are also used in the two modes.

direct beam, as illustrated in figure 2.11(b). This is DF imaging, and is distinguished from BF mainly by the selected reflection. They can however be used obtain different information based on this difference, especially important for specimens with multiple grains of different orientation. Since the direct beam is insensitive to which reflection spot it loses intensity, different grains might not be distinguishable if they diffract equally much intensity away from the direct beam. In DF, a contrast between different grains can be accomplished by selecting a diffraction spot belonging to the diffraction conditions of a single grain only. This grain and others that shares the selected reflection spot, will then yield an inverse amplitude contrast while the other grains becomes dark. The reflection should also be centered at the optical axis by tilting the incoming beam to reduce aberration effects, called centered DF.

Besides imaging different grains, DF can reveal interfaces separating domains which differ only by a rotation if the crystal is non-centrosymmetric. According to the kinemtic theory of diffraction as described in section 2.1.2, Friedel's law ensures that the diffraction pattern is centrosymmetric, implying that a 180° rotation of the crystal would not yield a different diffraction pattern. However, the dynamic theory in section 2.1.4 does not

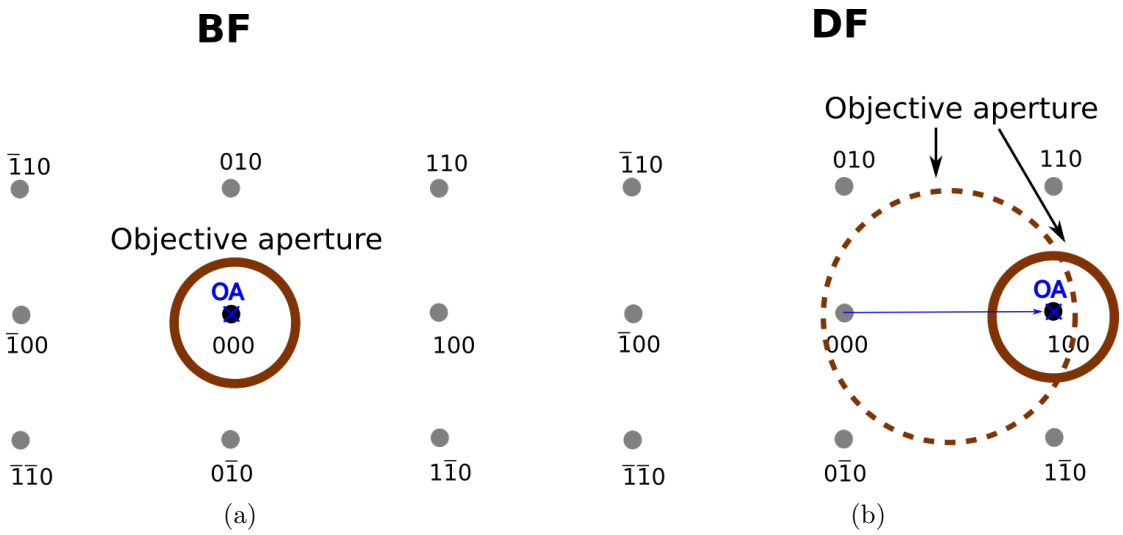

Figure 2.11: The figure shows an indexed DP viewed along the optic axis and the schematic of the BF/DF concept; using the objective aperture to select a single diffraction spot. (a) BF: selecting direct beam and excluding the other reflections. (b) DF: selecting the (100) reflection, excluding the others. The reflection is also centered at the optical axis (OA, marked by blue cross). Dotted line represents a larger aperture that include the (100) spot and the direct beam. Images are adapted from [16].

follow the same assumption. Looking at equation 2.23, the diffracted intensities violates Friedel's law due to multiple scattering events whenever the ectinction length is not centrosymmetric. The extinction length is in turn inversely proportional to the fourier components of the crystal potential in equation 2.17, which is not centrosymmetric for ferroelectrics. Therefore, any selected reflection might result in a contrast between regions that are simply rotated with respect to one another, a useful property when imaging ferroelectrics or other non-centrosymmetric features[27].

HRTEM

Using phase contrast to gain HRTEM images is easy to obtain, but also more tricky to interpret than the BF and DF images. In fact, to fully understand the image both the periodic potential and the precise thickness of the specimen must be known. Since this is not realistic, a specific formalism unique to HRTEM is used as a compromise to extract as much information as possible.

The specimen and image are represented with two functions $f(\mathbf{r})$ and $g(\mathbf{r})$ that contain the intensity amplitude. Since the image function is a mapping of the specimen by some function $h(\mathbf{r})$, the relation between image and specimen can be written as the convolution between the mapping and the specimen:

$$g(\mathbf{r}) = \int f(\mathbf{r}')h(\mathbf{r}-\mathbf{r}')d\mathbf{r}' = (f \otimes h)(\mathbf{r}) \tag{2.56}$$

In principle, the mapping transforms points in the specimen to extended disks in the image. Both convolutions and periodic functions are better described with the FT, and so $g(\mathbf{r}), f(\mathbf{r})$ and $h(\mathbf{r})$ is represented with their FT's; $G(\mathbf{u}), F(\mathbf{u})$ and $H(\mathbf{u})$ where $\mathbf{u}$ is the reciprocal lattice vector or the spatial frequency of the crystal (same as in equation 2.3). Equation 2.56 can then be written as:

$$G(\mathbf{u}) = F(\mathbf{u})H(\mathbf{u}) \tag{2.57}$$

Furthermore, in reciprocal space the mapping function $H(\mathbf{u})$ can be written as the multiplication of its contributing factors. These are the aperture function $A(\mathbf{u})$, the envelope function $E(\mathbf{u})$ and the aberration function $B(\mathbf{u})$. The aperture function removes beams that falls on the outside of the objective aperture. The envelope function takes into account chromatic aberrations which cause beams at larger angles to loose intensity and therefore works in the same manner as the aberration function by limiting the number of beams included. The aberration function then takes into account lens aberrations, and can be shown to take the form:

$$B(\mathbf{u}) = e^{i\chi(\mathbf{u})}\,, \quad \chi(\mathbf{u}) = \pi\Delta f\lambda u^2 + \frac{1}{2}\pi C_s\lambda^3 u^4 \tag{2.58}$$

C_s is the spherical aberrations, Δf is the defocus and λ is the electron wavelength.

Returning to the specimen function, it can be represented as:

$$f(x,y) = e^{-i\phi_t(x,y)} \tag{2.59}$$

The only difference between two points in the specimen is how they generate different phases in the electron wave function. This representation is called the phase-object approximation (POA) and in general is only valid for thin specimens. The phase change, ϕ_t only depends on the 2D projection of the crystal potential, which can be expressed as:

$$V_t(x,y) = \int_0^t V(x,y,z)dz \tag{2.60}$$

The reason thickness is an important factor for the phase change is that the electrons experience a different average potential inside the crystal compared to in vacuum, which leads to a speed or wavelength difference between vacuum and the crystal. The phase change through a slice dz of the specimen then becomes:

$$d\phi = 2\pi\frac{dz}{\lambda'} - 2\pi\frac{dz}{\lambda} = \frac{\pi}{\lambda E}V(x,y,z)dz\,, \quad \lambda = \frac{h}{\sqrt{2meE}}\,, \quad \lambda' = \frac{h}{\sqrt{2me(E+V(x,y,z))}} \tag{2.61}$$

where λ' is the wavelength inside the crystal. The total phase shift is then obtained by integrating out the z-dependence and collecting all prefactors in the interaction constant σ:

$$\phi_t = \sigma\int_0^t V(x,y,z)dz = \sigma V_t(x,y) \tag{2.62}$$

An change in the specimen equation can occur as a result of absorption, which can be included into equation 2.59 by multiplying it with an exponentially decaying function with absorption function $\mu(x, y)$ as the exponent. The final specimen function is then:

$$f(x, y) = e^{-i\sigma V_t(x,y)-\mu(x,y)} \tag{2.63}$$

A clear relation between the specimen function and the potential can be made in the case where the specimen is very thin ($V_t << 1$), and is called the weak POA (WPOA). First-order series expansion is then valid, while neglecting absorption, and the specimen functions becomes linearly related to the crystal potential:

$$f(x, y) = 1 - i\sigma V_t(x, y) \tag{2.64}$$

Using this result into the original equation for image formation, equation 2.56, and assuming the mapping function is on the form e^{iy}, then only imaginary parts of the mapping functions can contribute to the final intensity when neglecting terms with σ^2 (assumed σ is small). Since the aberration function is the only function with an imaginary component, it is rewritten to $2sin(\chi(\mathbf{u}))$. The new mapping function is often called the objective lens transfer function, $T(\mathbf{u})$, it is only valid in the WPOA approximation and takes the form:

$$T(\mathbf{u}) = A(\mathbf{u})E(\mathbf{u})2sin(\chi(\mathbf{u})) \tag{2.65}$$

Whenever this function becomes negative, then atom centers appear dark on a bright background, and the opposite case happens for a positive transfer function. While not exactly the same case as in figure 2.8, the analogy is clear: contrast in HRTEM changes depending on the microscope settings. Furthermore, the sine function can go to zero for several values of $\mathbf{u}$ and there is no detail in the image. This also implies that the transfer function may have different signs for different reciprocal vectors, so the first root of the transfer function, $\mathbf{u_1}$, sets the limit for when we are allowed to directly interpret the image. In order to make direct interpretation of the image possible with maximum resolution, the goal is then to make this root as large as possible and cut off the transfer function for larger values (while keeping the transfer function as large as possible). Cutting off larger reflections is easily done with the objective aperture, but controlling the transfer function up to this point is more tricky. Mainly, $\chi(\mathbf{u})$ in equation 2.58 must be controlled and it contains three parameters; defocus, spherical aberrations and the wavelength. The last two are fixed for microscopes used in conventional TEM, but the defocus can be varied.

Varying the defocus to control the aberration function in equation 2.58 is central to maximizing information in HRTEM. From the equation, it is clear that for small $\mathbf{u}$, the defocus term is leading, while for larger $\mathbf{u}$ the second term including spherical aberrations take over. The second term is however positive, so a negative defocus may in fact reduce the effect of aberrations, and extend the first root. Reducing too far will however lead to additional roots before $\mathbf{u_1}$ and the optimal defocus is called the Scherzer defocus. At this defocus, spherical aberrations is balanced by a specific negative defocus:

$$\Delta f_{Sch} = -1.2(C_s\lambda)^{\frac{1}{2}} \tag{2.66}$$

At this defocus value, the resolution limit of the microscope is defined and represents the best setting for extracting information intuitively[13].

Diffraction in TEM

By reducing the strength of the intermediate lens while in imaging mode (figure 2.10), the back focal plane of the objective lens can instead be placed in the objective plane of the intermediate lens. Now, by using a parallel beam a DP consisting of bright spots will be projected onto the screen for diffraction experiments as in figure 2.14(a). These bright spots originate in elastic scattering and will then represent the reciprocal space of the lattice as described in section 2.1.2. While electron diffraction is primarily dynamic, a parallel beam will only permit a single direction for the electrons. This means that the Ewald's sphere overlaps with each reflection only for a single value for the deviation parameter and much of the theory in section 2.1.4 becomes irrelevant. Therefore, the DP is best described from equation 2.6, as single scattering events (kinematic). This also means that this diffraction pattern will always be centrosymmetric, even if the crystal is not, and not very sensitive to small tilting and thickness as dynamical theory suggests. In addition to elastic scattering, inelastic scattering can be important for diffraction, but in this case it is discarded as noise. Furthermore, the SAD aperture is used in diffraction mode to select out an area in the specimen to be illuminated, hence selected area diffraction (SAED). If the whole specimen was used all the time, the diffraction pattern could have been flooded with multiple DP's and impossible to interpret.

If the specimen is thick enough, there will be a large number of electrons scattered incoherently in the forward direction. If this incident beam of incoherent electrons travel at a scattering angle to another lattice plane hkl, then they will be scattered again (dynamic scattering). Since the beam also comes from several angles, diffraction occurs as a cone on the screen as in figure 2.12. The surface of this cone now represents the possible angles for diffraction, and is called the Kossel cone. Where the Kossel cone and the Ewald's sphere overlaps (diffraction condition satisfied) a line is drawn on the screen in the DP called a Kikuchi line for a particular lattice place hkl. Combining all the lattice planes of the crystal gives the Kikuchi map. This map will then contain Kikuchi lines for every lattice plane, and therefore contain the same symmetry elements as the crystal itself, making it possible to orient the sample according to the appearance of the map.

Most the arguments for using parallel beam diffraction and the SA aperture are the same arguments one could use for motivating not using parallel diffraction. It does not include dynamical effects, it is not very sensitive to the exact orientation or thickness and it can probe large regions simultaneously. If these conditions are wanted, the analysis are greatly simplified and parallel diffraction will do the trick. However, if the goal is to study small regions or to study dynamical effects to reveal non-centrosymmetric properties such as polarization, then the convergent beam diffraction (CBED) technique

[13]This is a different limit than the one stated in section 2.2.1, which only took into account whether two points could be distinguished or not.

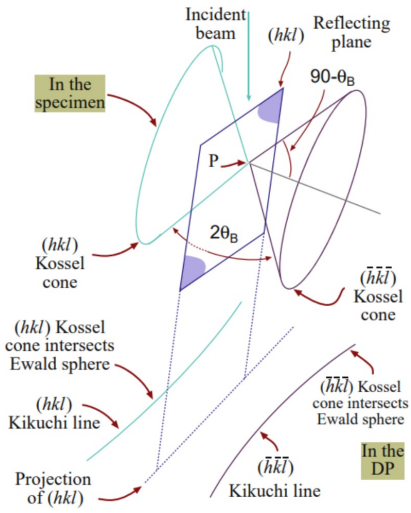

Figure 2.12: Schematic of Kikuchi pattern origin. Image is taken from [16].

is the correct tool. The technique is used in diffraction mode, same as in SAED, but the beam is converged into small spot with a specific convergence angle α and the SA aperture is not used.

Revisiting the Ewald's sphere in figure 2.3(b), the picture can be extended to include the CBED technique. Converging the beam means in principle that electrons will enter from all angles within a 2α degree cone, and the Ewald's sphere must then be considered for each direction (equivalent to tilting the direct beam around the center spot). The result is that the diffraction pattern will consists of disks with a radius equal to the convergence angle while representing a range of values for the deviation parameter. If the disks are small and separated far apart the pattern is called a Kossel-Möllenstedt pattern, while almost complete overlap of the disks is called a Kossel pattern.

To illustrate, figure 2.13 shows the ideal two-beam case, where the diffracted beam g perfectly overlaps with the Ewald's sphere for SAED, and thus the deviation parameter is zero at the center of the cone (the only point used in SAED). From the center, the deviation parameter increases approximately linearly with the angle θ away from the optical axis until θ reaches the convergence angle; $S_{\mathbf{g}} = \mathbf{g}\delta\theta$. Furthermore, the deviation parameter is positive to the left and negative to the right, and fringes consistent with equation 2.42 wil then appear in the image. In a two-beam or 1D case, these fringes should be vertical, although the more realistic multi-beam and 2D case suggests fringes are possible in all directions. Equation **??** for the multi-beam approximation also indicates that a displaced center is possible (not exact Bragg condition), so the only prediction we can make of the intensity distribution inside the CBED disks is that it will vary with a periodicity depending on the local thickness, deviation and extinction parameter of the specimen. However, it is worth noting that a bright features in the diffracted disks must originate in dark features in other disks (intensity must come from somewhere). In the simplest two-beam case, fringes can then be associated with specific

diffraction conditions and be used for measuring parameters such as thickness. So for most situations simulations are required for interpreting the intensity variations inside the CBED patterns accurately.

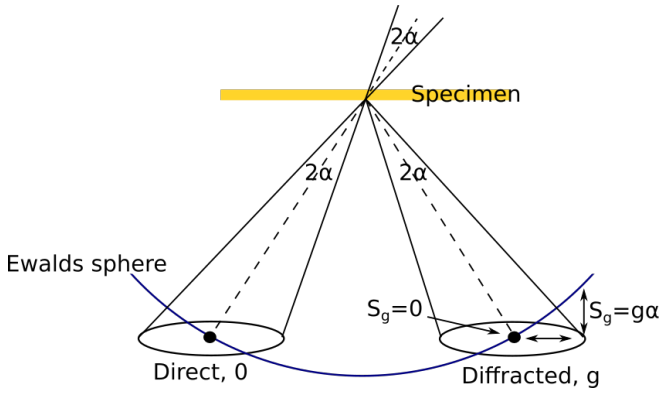

Figure 2.13: Schematic of the diffraction condition in the CBED case compared to the parallel case (stripled line). Spots turn into disks with a variety of deviation parameters that display dynamical features clearly. Note that the figure shows only the two-beam case, with perfect overlap between center of diffracted cone and Ewald's sphere. Normally the zero value for the deviation parameter are located outside the disk center.

An additional effect of broadening of the Ewald's sphere is the increased chance for intercepting HOLZ spots, and so sharp lines called HOLZ lines are often seen in CBED disks. Unlike the centrosymmetric single scattering event forming spots in SAD and disks in CBED, the HOLZ lines contain 3D information, and can therefore show the true symmetry of the specimen. In the case of figure 2.14, a threefold symmetry is shown by the HOLZ lines while the Kikuchi lines, SAD and CBED patterns shows a six-fold symmetry. Incoherently scattered electrons also have an increased chance of being diffracted, so kikuchi lines are more likely to appear in the CBED patterns that SAED pattern.

2.2.6 Scanning Transmission Electron Microscopy

Obtaining local information on the atomic structure is always a challenge, and the two technique discussed so far that could offer this is the HRTEM and CBED techniques. Both have a similar problem and that is they both require simulations to properly interpret, which assumes the structure is already known. Studying a new, potentially unknown structure, may require direct visualization of the atomic structure which scanning transmission electron microscopy (STEM) can offer.

Basic Principles

The basic principle of STEM is illustrated in figure 2.15(a). The beam is formed into a very fine probe (from 0.2 to 2 nm) by the condenser lens and upper objective lens

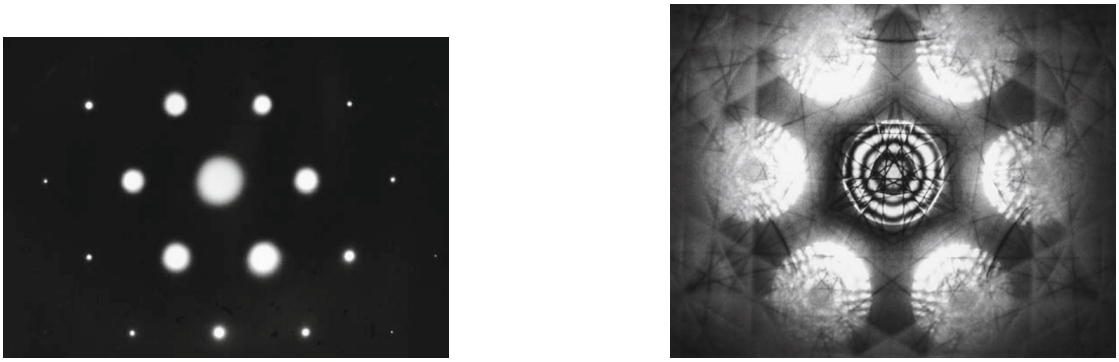

(a) (b)

Figure 2.14: (a) SAD pattern in the [111] direction in Si. The size of the reflections are not perfectly symmetric, indicating that DP is slighty off the zone-axis. (b) CBED pattern of [111] Si. Images are taken from [16].

and a CBED pattern is formed at BFP of the intermediate lens same as in diffraction mode (figure 2.10(a)). The probe is then scanned across the specimen by the deflection coils. With a specific step size, the probe stops for a given time at a point (x, y) and the intensity is recorded by dedicated STEM detectors below the specimen. The distance, or effective distance as formed by the intermediate lenses (camera length) together with the detector size, determine what range of scattered electrons are recorded. Different scattering angles give different contrast/information. The scan continues until an image can be formed based on measured intensity at each point, in contrast to conventional TEM where the whole image is formed simultaneously. This approach comes with three main advantages. First, the fine probe allows for very small regions to be probed separately while the scanning makes it more efficient than manually selecting region, and also distribute the dose differently. Second, the resolution of STEM is limited solely by the probe quality which only depends on the condenser lens and not the imaging system. So chromatic aberration which only appear after the beam hits the specimen, is therefore absent in STEM. Spherical aberration and astigmatism still distorts the image as in HRTEM. Third, additional contrast which gives additional information can be obtained. These different signal ranges can also be collected simultaneously. One downside to STEM is that images take a long time to form and hence distortions (drift, noise, vibrations) can affect the image.

STEM Imaging

STEM detectors select a range of the diffraction pattern to form the images, and the two common choices are high-angle annular dark-field STEM (HAADF-STEM) and bright-field STEM (BF-STEM) (see figure 2.15(b)). The HAADF detector uses an annular detector that collects the incoherent high-angle scattering, but a coherent CBED pattern can also be formed and collected with small condenser apertures and larger cam-

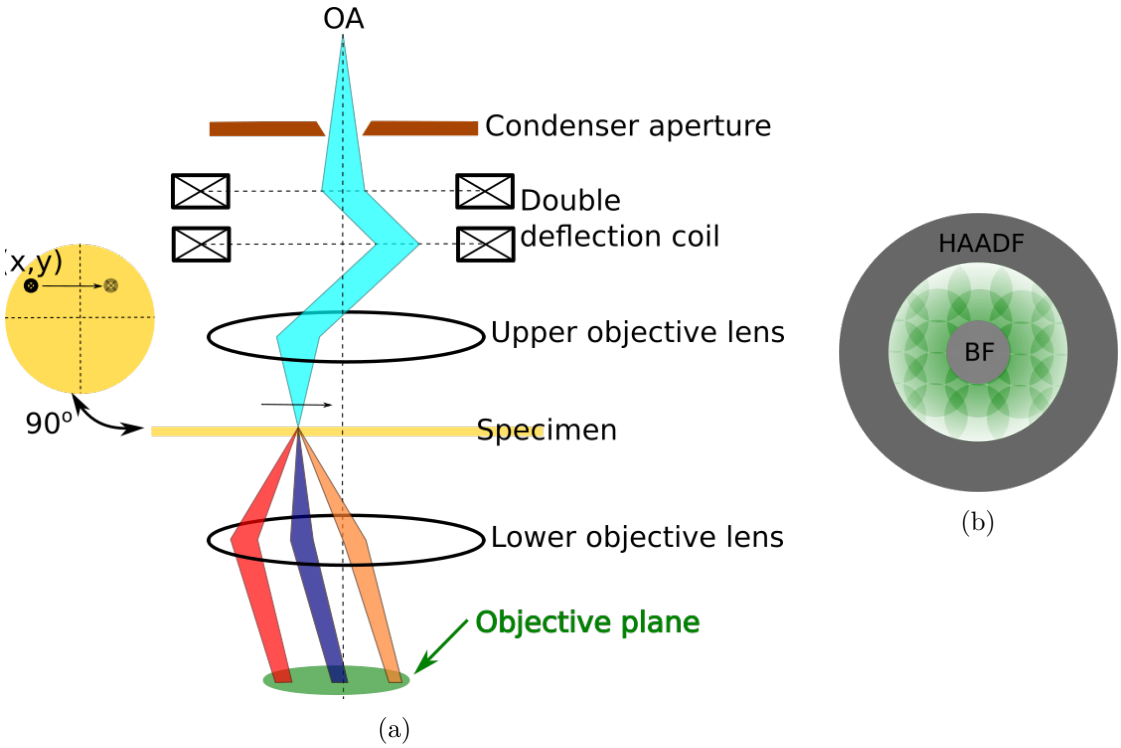

Figure 2.15: Schematic of (a) STEM operation and (b) STEM detectors (seen from the direction of the beam with CBED disks inside). The beam is converged onto the specimen at a location (x, y) and a CBED pattern forms in the BFP of the intermediate system analogously to the diffraction technique in figure 2.10(a). Total intensity over one of the two detectors is then recorded and saved as the value of one pixel. A scan over an area then results in an image.

era lengths. The BF detector on the other hand reads the direct beam and low-angle diffracted beams. Other shapes or part of the diffraction pattern can be used, for instance a segment of the annular detector.

While HRTEM requires simulations to interpret, STEM images are far easier to understand. When the probe passes over an atom column the scattered beams gain intensity and the direct beam loses intensity. The BF signal will thus weakened while the ADF signal is strengthened, and the contrast is then directly related to the atomic positions. In ADF-STEM, bright spots in the images (high value pixels) is therefore the position of an atomic column. Using an annular detector also eliminates the role of symmetry, and since the high-angle diffracted beams are more sensitive to the atomic number there is also a strong Z-contrast (equation 2.51). Finally, since the HAADF-STEM detector is insensitive to phase contrast (incoherent scattering), also the overview images are more easily interpreted and can often be useful for isolating particular features from interference effects.

HAADF-STEM is in general a complementary technique to HRTEM, but the ad-

vantages usually outweigh the disadvantages. When the diffracted signals are directly detected, there is no phase contrast to worry about (incoherent signals), and atoms on STEM images are in fact atoms with the exact placement the image indicates (this is not the case in HRTEM). In addition, with crystal structures as $ErMnO_3$ and $Pb_5Ge_3O_{11}$ the Z-contrast from HAADF-STEM is especially useful as the heavy elements can be separated from the lighter elements making the unit cells easily identifiable. At the same time this is a disadvantage if the light elements are important to capture.

The scanning and longer frame time will introduce noise limiting resolution and image quality, but the SmartAlign software can be used to overcome this[28][29]. Instead of taking a single long scan, the software takes several quick scans (between 20 and 100) which separately does not include any significant noise. The software first performs a rigid registration, where the offset in each image from the prior is found and the stack is then summed up and averaged after correcting for the offset. The second step is a non-rigid registration where offsets inside each frame is corrected for. The software matches the gradients inside each frame and compares them to find how the features inside each frame has moved, before correcting it and averaging over the frames. In total, both drift and noise between the scans and within is corrected for.

Additional Approaches and Aspects

The STEM technique has advantages besides high-resolution imaging and other techniques that does not use the STEM detectors can still benefit from the efficiency of a scanning probe. Probing a small area with a more intense and slightly larger probe than in imaging (1.5 nm) and simultaneously recording the EDX signal gives analytical information in addition to the CBED pattern from the scattered electrons. Scanning the probe without using the STEM detectors can then be used to create an image based on EDX (EDX-STEM) signals instead of scattering, and creating maps with EDX data enables a more efficient way of obtaining analytcial information in multiple areas. Likewise, recording the CBED pattern with the CCD camera instead of the STEM detectors gives a map of CBED patterns in a technique called Scanning CBED (SCBED)[30][31]. If there is a particular feature the CBED pattern of interest, i.e. direction of the **c**-axis, this can then be obtained at several points in short time and be combined with software for analysing the patterns simultaneously. One challenge is the large convergence angle, which in STEM is usually higher than in conventional CBED, and can lead to disk overlap. In addition, the direct beam can be displaced from the center to enhance the contrast from specific regions of the CBED pattern similar to the DF technique in a technique called off-axis STEM.

2.3 Scanning Electron Microscopy

The scanning electron microscope (SEM) is a versatile microscope for surface studies that is highly complementary to the TEM. The two electron based instruments are similar in many ways especially when it concerns the lens system above the specimen

that forms the electron probe, but they use different signals produced by the direct beam with different contrast mechanisms to form images. Applying SEM can therefore reveal features hidden in the TEM, and more specifically, ferroelectric domains can show a contrast difference when directly imaging the surface. This section is based on chapter 4 of the book by Michler[32] if not otherwise stated.

The idea of the SEM is similar to the STEM; the beam is converged into a fine probe (5-10 Å) and scanned across the sample, and the signal from the detector is stored for every position to reconstruct an image. The design of the instrument is similar to the the STEM design in figure 2.15(a), but an additional aperture is inserted after the upper objective lens, and only a few SEM's have a BF and ADF STEM detectors to record transmitted electrons as in figure 2.15(b)[14]. However, the SEM is based around two signals not typically used in the TEM. These are the backscattered and secondary electrons (BSE and SE) as mentioned in section 2.2.3 and illustrated in figure 2.16. In addition, since a SEM is not based on transmission they operate at a lower voltage, usually below 30 keV and down to 0.5 keV.

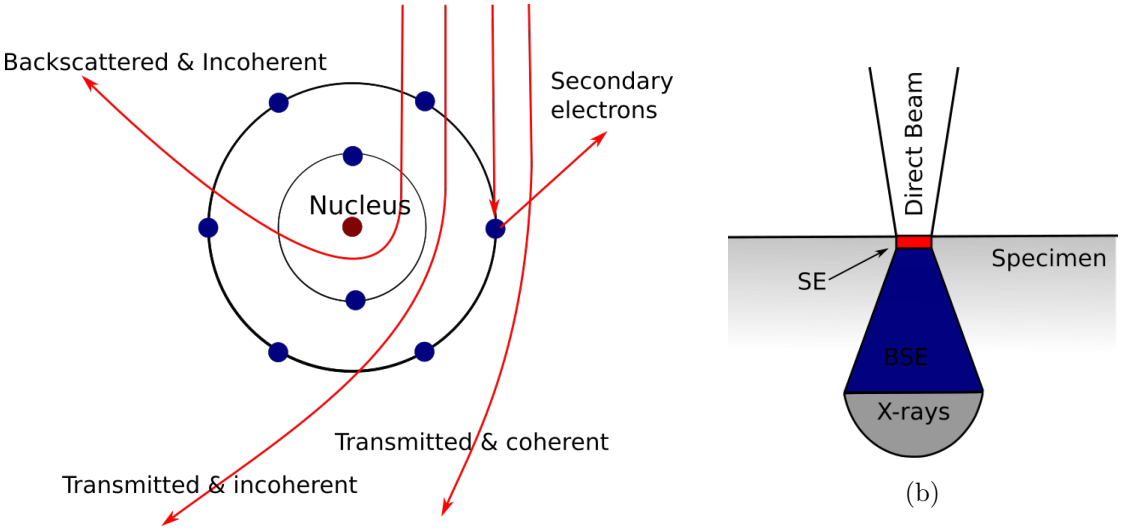

Figure 2.16: (a) the different signals produced by the direct beam and their relation to coherency and scattering angle. (b) depth of penetration and generation into the specimen for the different signals.

The backscattered electrons can be considered as reflected electrons, and have insufficient energy to be transmitted through the specimen. They are still elastically scattered, but are incoherent due to multiple scattering events before being able to exit the specimen. Secondary electrons is the most commonly used signal for SEM's, and is based on electrons that are generated from the direct beam. Whenever the atoms are exposed to

[14]These instruments are called S(T)EM where the "T" for transmission is in parenthesis to distinguish these instruments from the STEM technique in a TEM.

high energy radiation, electrons can accumulate energy until it exceeds the work function of the specimen at which point they are emitted. Most SEM's are usually equipped with detectors for both signals, as they show different contrast due to their different origin.

Understanding the contrast in more detail is critical, and the main idea is illustrated in figure 2.16(b), where the depth and volume of the signal generation is shown. As the direct beam enters the specimen it generates secondary electrons, but only with a small amount of energy. Thus, only those electrons close to the surface are able to be emitted and detected/contribute to the image. This is major advantage as it allows us to probe the surface of the specimen alone with a high resolution. Flat regions can also be distinguished from curved regions as the curves imply a larger surface and more emitting secondary electrons. On the other hand, back-scattered electrons are generated from a much larger region which reduces the resolution and makes the images less surface sensitive. Edges will also result in less back-scattering. Both signals are sensitive to the atomic number, but back-scattered electrons more so than the secondary electrons, which makes the images suitable for elemental analysis. These two signals can also be acquired simultaneously and compared. Subtracting the BSE signal from the SE signal removes any compositional features, and we are left with topological images. Alternatively, the two signals can be summed up for compositional information, since topological variations have opposite contrast. In general secondary electrons are used for topological contrast and backscattered electrons are used for elemental contrast.

Besides controlling the signal, source another option when using the SEM is adjusting the beam energy. The generation volume of figure 2.16(b) increases with the beam energy which reduces the resolution, but the abberation is also reduced which can in turn increase the resolution. Since the interaction volume is smaller for high-Z materials, these can benefit from increased energy and reduced abberations while the opposite is the case for low-Z materials. In addition, if the beam energy changes, so does the charging of the specimen. For most bulk materials, the specimen decharges at energies below 2 keV and above a few hundred eV. The reason is that low energy electron does not have the energy to produce SE, and high energy electrons penetrate too far into the material for generated SE to be emitted into vacuum. Above the range where the specimen decharges, it builds up negative charge instead and the electron probe will become deflected causing problems for imaging. Postive charging does not cause as much of a problem. Finding the excact values at which the material does not accumulates negative charge can therefore be important for insulating samples. In condutive samples this is not a problem as long as the material is grounded, but the yield of these materials are also smaller so larger acquisition times may be needed[33].

A final point to mention when it comes to contrast in the SEM is how ferroelectric domains will display contrast (see section 2.4 on ferroelectricity). Multiple articles report that the ferroelectric domains are directly visible in the SEM as opposite domains have different emission currents[17][35][9]. This has been explained from the pyroelectric effect, as heating the specimen with the electron beams lead to different electrostatic potentials for the opposite domains, hence leading to different emission currents making the domains visible.

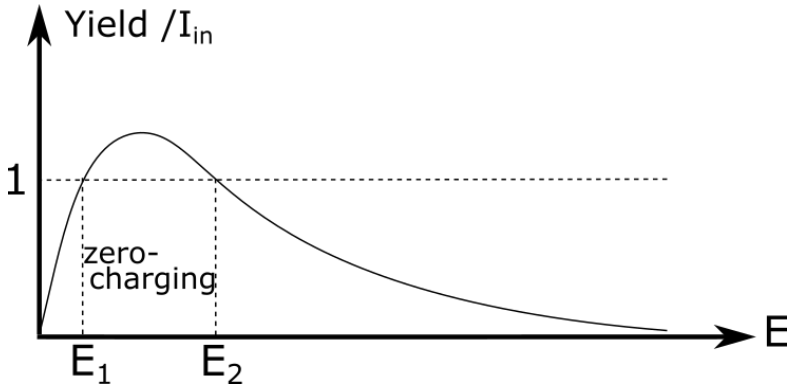

Figure 2.17: Schematic of the yield (output intensity) of a material in a SEM, divided by the input current. Between E_1 and E_2 the material is emitting more than is deposited and is positively charging. Figure is redrawn from [34].

2.4 Ferroelectricity

The theory on phase transitions and landau theory is based on the book from Kittel[22], and the basics of ferroelectrics is based on the review paper from Catalan, Seidel, Ramesh & Scott[6], while the more detailed mechanisms are based on the review paper from Barone and Picozzi[36] and the review paper from Manfred, Lottermoser, Meier & Trassin[37]. The details on the ferroelectric mechanisms in $ErMnO_3$ are based on a paper from Holtz et al.[5] and will be covered in more detail as well as the domain structure. There is however limited research done for $Pb_5Ge_3O_{11}$ and much is still unknown, but a brief discussion the phase transition will be given based on a paper by Iwata[38] and Baikie[39], as well as larger section on the domain structure mostly based on a paper by Shur[11].

2.4.1 Ferroelectric Crystals and Macroscopic Behavior

Ferroelectric crystals have at least one characteric property in common; a spontaneous polarization is present below the Curie temperature T_c (Néel temperature for ferromagnetism). Above the Curie temperature the material is in a paraelectric phase without a net polarization when no electric field is applied. In addition to forming spontaneous dipole moments the crystal forms domains with a net polarization, which on a macroscopic scale cancel each other out. The reason is that aligning the dipoles parallel to each other might be energetically favourable at the microscopic scale, but the net polarization is not be favourable and thus the domains seek to neutralize it. The interfaces between each domain, the domain walls, cost in turn more energy than the bulk structure and are also avoided as much as possible. The domain formation is thus a trade-off between the energetically costly domain walls and the macroscopic polarization[6].

These domains will however create a different response to an external electric field than the paraelectric phase which only aligns the dipoles weakly along the applied field.

When the ferroelectric crystal is exposed to an electric field, the previous domain formation is not necessarily favourable any more, as the field causes polarization directions parallel to the applied field to become more energetically favourable than the opposite domains. The hysteresis loop in figure 2.18 illustrates this response of the domains to external electric fields, which is central to the study of ferroics. Beginning in point 4, the crystal is brought out of equilibrium by an electric field until it reaches saturation at point 2 where all the domains are aligned with the electric field and the increasing field is just stretching the dipoles. Removing the applied electric field, the polarization decreases, but remains non-zero at point 3 since a net polarization (remnant polarization, P_r) is present and thus favours a certain direction even when the applied electric field is removed. By reversing the applied electric field (point 1)[15], the domains can be flipped into a new saturation region.

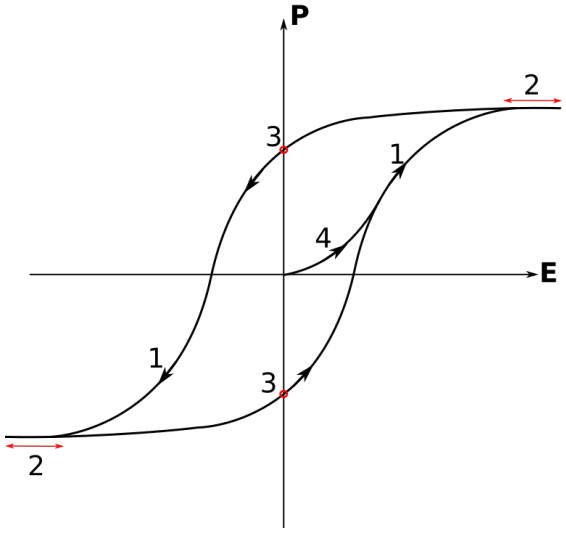

Figure 2.18: A hysteresis loop of a ferroelectric crystal with multiple domains showing the polarization response to an applied electric field. The numbers indicate specific behaviour: 1, the alignment of domains into the direction of the electric field; 2, saturation region where all domains are aligned with the electric field; 3, points where the electric field is zero, but net polarization remains; 4, same as 1, but for a crystal without net polarization.

A similar hysteresis loop exists for ferromagnetic materials and both ferromagnetics and ferroelectrics can be used for memory applications in electronics, since the two states at point 3 remains without any external field and the material can thus be considered a two-state device. In fact, much of the theory regarding the ferroeletricity can be generalized by replacing the polarization with an order parameter η.

[15]The electrical field required to reduce the polarization to zero is called the coercive field.

2.4.2 Ferroelectric Domain Structures

As stated above, the competition between domains and domain walls is the key to understanding ferroelectric domain structures. To better quantify the dimensions involved with domain formation, some basic theory ferroelectrics should be presented. To simplify the problem, thin films with anti-parallel domains are mainly considered, and the domain formation is then expressed through Kittel's law:

$$w = \sqrt{\frac{\sigma}{U}d} \tag{2.67}$$

where w is the width of the domains, σ is the energy density per area of the domain wall, U is the volume energy density of the domain and d is the thickness of the film in the direction of the polarization. Strictly speaking, this law only applies to one type of domain structure, but it leads to a prediction in most materials that are important to remember: as the sample size decreases in the direction of the polarization, the domains becomes smaller and more domain walls occur. This prediction holds until a critical thickness is reached where the ferroelectricity disappears altogether. Usually, this happens as the size of the domains approach the size of the sample.

While Kittel's law assumes domain walls with zero or negligible thickness, real domain walls have a finite thickness δ. This thickness can also be expressed through the same quantities as in Kittel's law:

$$\frac{w^2}{\delta d} = G \tag{2.68}$$

where G is parameter which is only weakly dependent on the material classes, and lies around 1.765. This law is then quite useful, as it allows the size of domain walls to be measured based on the size of the domains.

Both these laws were originally derived for very simple systems, anti-parallel 180° domains in thin films, but they have shown remarkable universality. Numerous adjustments or modifications to Kittel's law have been made to fit specific material classes and more complex domain structures, such as nanodots, nanowires and 3D systems. Irregular domain walls for instance where the wall is not straight, have successfully been explained by replacing strict relations with probability distributions for the domain wall size and finding the parameters for specific materials. These irregular domain walls occur when the domain structure is pinned down by defects, altering the energy budget of the domain walls.

2.4.3 Phase Transitions and Landau Theory

As mentioned in section 2.1.1, due to Neumanns principle there can be no spontaneous polarization for crystals that possess inversion symmetry. Ferroelectric crystals thus require lower symmetry than paraelectric crystals, but even more important is that both properties can be found in the same material when heating or cooling past the Curie temperature. To accomplish this the material must then undergo a structural phase transition from a high symmetry structure at the paraelectric phase to a lower

symmetry at the ferroelectric phase. The exact mechanism that cause this symmetry breaking will be discussed in section 2.4.4.

These phase transitions are of 2nd order, while the more common transitions between two states of matter (i.e. liquid to solid) are of 1st order. The major physical difference between the two is that 1st order transitions happens discontinuously for the order parameter (and the entropy) and involve release or absorption of latent heat, see figure 2.19(a). The second order requires that the order parameter (and the entropy) varies continuously between the two states, and thus without any exchange of heat. To give a phenomenological explanation for such transitions, the Landau theory is used and polarization is replaced with an order parameter to generalize the theory[16].

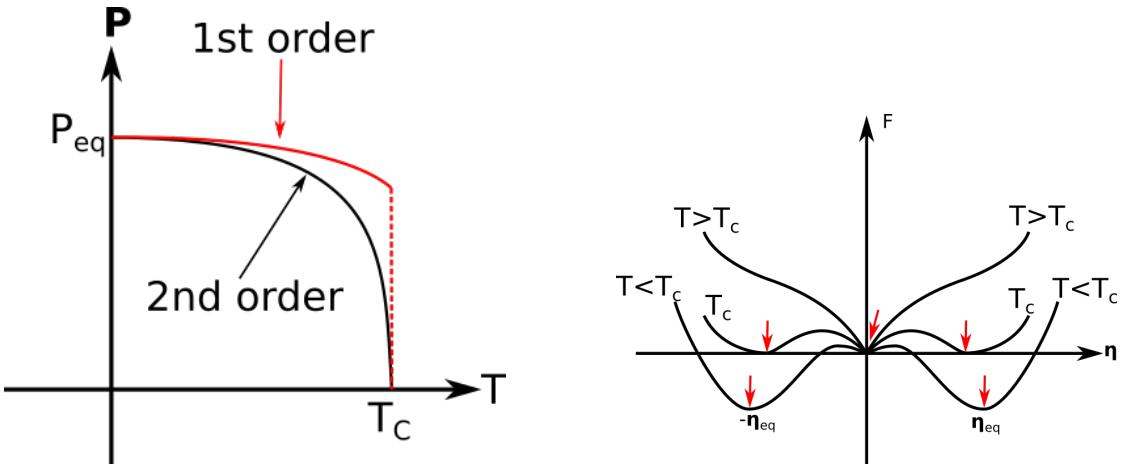

(a) (b)

Figure 2.19: (a) Schematic of polarization as a function of temperature when close to a phase transition. The red line illustrates a typical discontinuous behaviour of 1st order phase transitions, while the black line illustrates the continuous 2nd order transitions. (b) Schematic of the free energy as depicted in the Landau theory for temperature above, equal and below the phase transition temperature. Minimas or equilibrium points are indicated with red arrow.

All systems however require that the free energy, F, is minimized when the order parameter is zero above Curie temperature, and non-zero below Curie temperature. A series expansion of the free energy around the Curie temperature is therefore proposed:

$$F(\Theta; T, \eta) = -\Theta\eta + g_0 + \frac{1}{2}g_2\eta^2 + \frac{1}{4}g_4\eta^4 + \frac{1}{6}g_6\eta^6 + ... \tag{2.69}$$

The coefficients g_n are temperature dependent, and the odd terms are excluded since the free energy should be symmetric with respect to the direction of the order parameter without an external field, Θ. The first term includes just that, the effect of an external

[16]Phase transitions in other systems such as the transition in superconductors between the superconducting state and the metallic follows the same theory.

field on the free energy. To find the equilibrium values of the order parameter, we must then look for the minimum value for the free energy:

$$\frac{\partial F}{\partial \eta} = 0 = -\Theta + g_2\eta + g_4\eta^3 + g_6\eta^5 + ... \tag{2.70}$$

To obtain an ordered state, the coefficient g_2 should pass through zero at some temperature below T_c. It can therefore be expressed as $g_2 = \gamma(T - T_c)$ and γ is a positive constant. If g_4 is assumed to be positive, then above T_c, there are only positive contributions and the g_6 term can be neglected. Below T_c, there is a balance between the negative g_2 and positive g_4, and g_6 still does not add anything new to the dynamics and can thus be ignored completely. This leaves us with the equilibrium value in the absence of an external field from equations 2.69 and 2.70 with negative g_2:

$$\eta_{eq}^2 = \frac{\gamma}{g_4}\left(T_c - T\right), \quad T < T_c \tag{2.71}$$

The solution for a positive g_2 is $\eta = 0$, which was our initial requirement of no ordering above T_c. All equilibrium points for T above, equal and below the transition temperature is indicated in figure 2.19(b).

While the Landau theory presented offers a phenomenological explanation for the phase transitions, it does not cover the actual mechanisms for ferroelectricity to happen, or for the free energy to be minimized for non-zero polarizations.

2.4.4 Ferroelectric Mechanisms

The macroscopic properties of ferroelectrics explained in sections 2.4.1 and 2.4.2 are general rules for all ferroelectrics. The details on the microscopic origin is however more complex and different for each type of material systems, so a general treatment must be presented for clarity. In addition, the exact ferroelectric origin for material classes of interest, $ErMnO_3$ and $Pb_5Ge_3O_{11}$, is explained as specific examples (and as far as understood to date). $ErMnO_3$ has been thoroughly investigated and the ferroelectric origin is understood by now, but much of the mechanisms at play in $Pb_5Ge_3O_{11}$ is not yet unveiled.

Ferroelectricity can originate in one of two set of mechanisms. The first and most important for this thesis is through ionic displacements. This requires a structural deformation, as when a phonon freezes making the atomic displacement from the phonon permanent, thereby reducing the symmetry and breaking inversion symmetry as well as creating a polar state. The other set of mechanisms does not involve structural rearrangements, but instead a rearrangement of the electronic structure into breaking centrosymmetry and causing a polar state. Furthermore, we also distinguish between proper and improper ferroelectrics. As mentioned in section 2.4.3, the order parameter changes from zero to non-zero under a phase transition, but additional parameters can also change. If the polarization is the primary order parameter for the transitions, such as in $BaTiO_3$, the result is a proper ferroelectric. Otherwise, where polarization is a by-product of another ordering (i.e. magnetization or structural), the result is an

improper ferroelectric. Both the proper and improper mechanisms are relevant for this thesis as the hexagonal manganites ($RMnO_3$, R = Er, Y, Sc, Dy, Ho, Tm, Yb, Lu) are improper ferroelectrics while $Pb_5Ge_3O_{11}$ is a proper ferroelectric. The separation between proper and improper is perhaps the most useful (compared to structural vs electronic mechanisms), but within this separation there are five distinct mechanisms identified so far.

Two of the five mechanisms belong to conventional proper ferroelectrics. The first is the anisotropic hybridization of the transition metal cation with its surrounding anions, leading to an off-centered displacement. In the conventional cubic perovskites, including the prototype ferroelectric $BaTiO_3$, the transition is marked by such a displacement of the center atom when it hybridizes with the oxygen atom in the direction of the polarization. Figure 2.20 illustrates the transition from cubic and paraelectric ((a)) to tetragonal and ferroelectric ((b)) for $BaTiO_3$. The second mechanism for proper ferroelectrics is the lone pair mechanism and can be found in materials such as $BiFeO_3$. In this case, unbonded valence electrons distribute anisotropically around the host ion, causing a polarization.

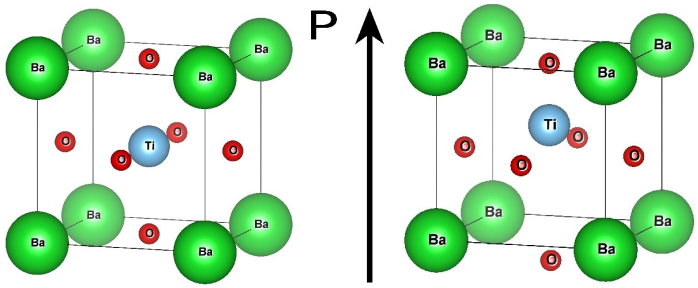

Figure 2.20: (a) Illustration of the cubic ($Pm\bar{3}m$) structure of $BaTiO_3$ above 403 K in the paraelectric phase. (b) Illustration of the tetragonal (P4mm) ferroelectric phase of $BaTiO_3$. The O atoms are shifted downwards while the Ti atom is shifted upwards, creating a dipole moment or polarization upwards. The displacement is exaggerated for illustrative purposes.

The three remaining ferroelectric mechanisms then belong to the improper ferroelectrics. The first of these are magnetically induced ferroelectricity found in $CaMn_7O_{12}$, where ferroelectricity occurs as a by-product of the magnetic ordering, although very weakly ($\sim 0.3\,\mu Ccm^{-2}$). The second mechanism is the charge ordering ferroelectricity, where valence electrons distribute anisotropically around the host ion leading to a dipole moment. The third, and most important for thesis, is the geometric ferroelectricity present in the hexagonal manganites.

The geometrical ferroelectricity is somewhat similar to the ferroelectricity in the perovskites, by the fact that both mechanisms are displacive. However, unlike the perovskite mechanism, the displacement for geometrical ferroelectricity does not originate in changes in the chemical bondings, but due to geometrical constraints. These geo-

metrical constraints are often rotations and tilting of the anions, leading to a net force acting on the cation pushing it into a polar state. The exact transition is different for each material, but the key element that makes this an improper ferroelectricity is that the original distortions in the material is the symmetry lowering event without causing polarization. The distortions following a specific phonon mode, P_1, must be non-polar and break inversion symmetry, but also unstable. Another stable phonon mode, P_2, which is both stable, polar and energetically unfavourable alone must be coupled to P_1 and the combination of these two modes results in a stable ferroelectric phase. However, since the polar mode is not the driving force behind the transition, the ferroelectricity becomes improper.

2.4.5 Ferroelectricity in $ErMnO_3$

Figure 2.21 shows the transition for the hexagonal manganites, from the paraelectric to ferroelectric phase. As mentioned above, the polarization is not the driving order parameter, but a by-product of another ordering parameter that cause the polar state to ermerge. In this case, the ordering parameter is a non-polar and unstable K_3[17] phonon causing the MnO_5 bypyramid tilting as it freezes, leading to inversion symmetry breaking. No polarization emerges due to the tilting however, but instead from freezing of a Γ_2^- phonon which shifts the Er atoms into the polar state[40][41]. This also begins to motivate the use of CBED discussed in section 2.1.2, since revealing the true symmetry would tell the direction of the ionic shift and polarization.

When the symmetry is reduced the first phonon mode, K_3, causing the tilting in the bipyramids, a new unit cell must be made. Since tilting two out three bypyramids breaks translation symmetry from one bipyramid to the next, the new unit cell must then consist of three bipyramids. This is called structural trimerization and has six possible permutations; three pyramids where one is not moved and two is tilting leads to three permutations, and tilting in and out gives an additional three. Furthermore, the in/out tilting determines the possible polarization directions, so the Γ_2^- phonon are unable to introduce new domains. Instead, they are forced the push the Er atoms into a specific pattern as in figure 2.21(b) ($\uparrow\uparrow\downarrow$, $\downarrow\downarrow\uparrow$), with a specific polarization direction (up, down). Summarized; the improper nature in $ErMnO_3$ originates in a K_3 phonon causing the MnO_5 bipyramids to tilt and create domains based on in/out tilting. The polarization emerges from a Γ_2^- phonon which adopts this domain pattern, by shifting Er atoms into the polar state allowed by the local bipyramid tilting.

The structural phase transitions is however not enough to describe the ferroelectic behaviour, as mentioned in section 2.4.2 the material also forms domains. In a proper ferroelectric, all domains must structure their polarization direction so the free energy from the polarization is minimized. In the case of figure 2.22(a) the domains align themself to minimize the net polarization. Domains that accumulate charges at the domain walls (head-to-head and tail-to-tail) such as in figure 2.22(b) should be unstable

[17] The K and Γ notation refers to the wavevector directions in the Brillouin zone; Γ is the center and K is the $< 100 >$ directions. The superscript and subscript refers to one particular phonon mode.

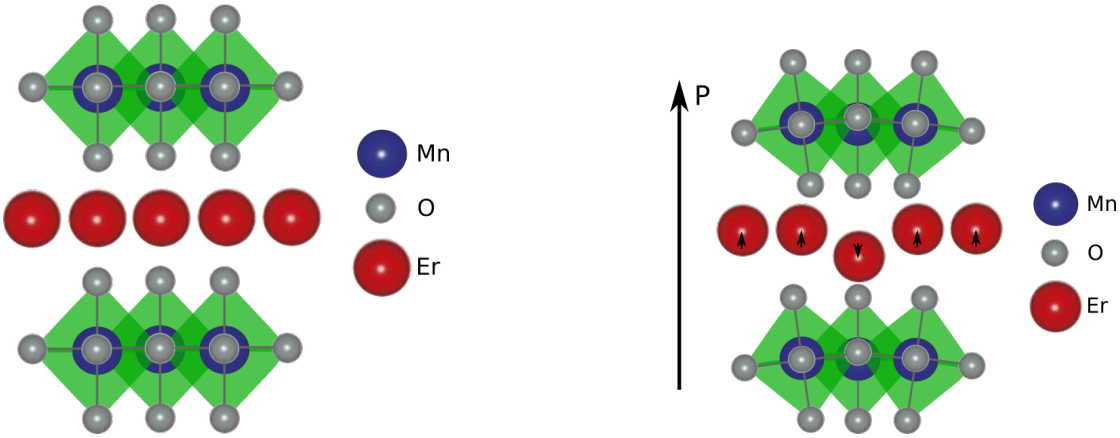

(a) (b)

Figure 2.21: The [100] direction of $ErMnO_3$ before and after phase transition at 1470 K. (a) The paraelectric phase $P6_3/mmc$. (b) The ferroelectic phase $P6_3cm$ with polarization upwards. The difference is summarized as tilting in the MnO_5 bipyramids and displacement of Er along the **c**-axis.

as they cost more energy due to the divergent electrostatic field than the neutral domain walls[6].

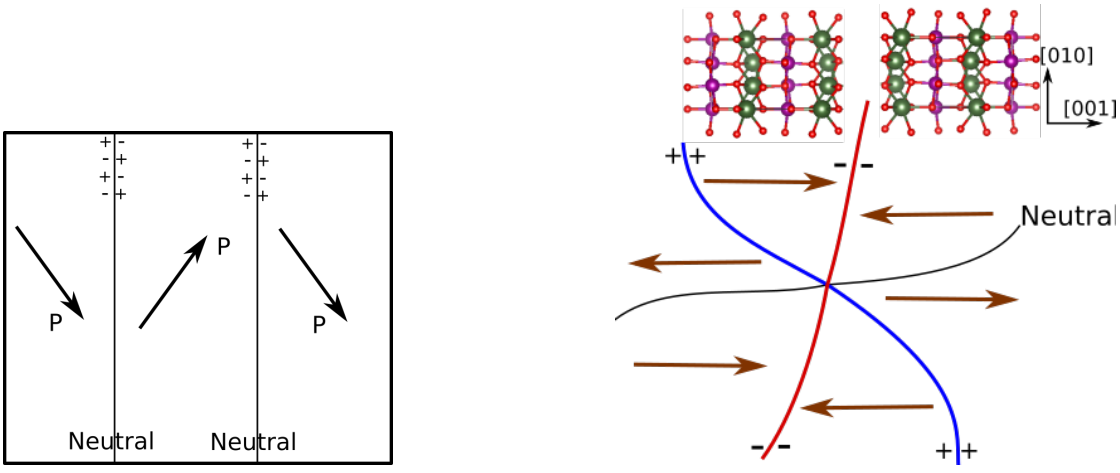

(a) (b)

Figure 2.22: (a) Schematic of neutral domain walls typically found in proper ferroelectrics such as $BaTiO_3$. (b) Neutral domain walls indicated in black, red indicates the head-to-head negatively charged wall and blue indicated the positively charged tail-to-tail domain wall. Brown arrows indicate polarization direction. The crystal orientation is flipped 180° across the domain wall with a part of the unit cell shown at each side. The sixfold symmetry and polarization directions is taken from [4].

As a consequence of the improper ferroelectricity in $ErMnO_3$, the domain structure will include vortices that enforce stable charged domain walls throughout the material. A vortex is illustrated in figure 2.22(b), which occurs wherever domain walls intersect and consists of all six domains from the trimerization. These are protected in the sense that they can not be removed or shifted by an electric field in the same way as the domain walls. They are also isotropic (found in all directions), even though the crystal does not posses the same symmetry in all directions. Due to the geometry of the vortices where domain walls intersect, two domain walls must be positively charged, two are negatively charged and two are neutral, as illustrated in figure 2.22(b). Since the vortices are locked in place, these charged domain walls are completely stable and always present in the domain structure[7], although they can still be moved with electrical fields. This one of the reasons for the huge interest in the material, as the charged domain walls display either enhanced or transistor-like conductivity[4]. Having this functionality present in topology that can be altered at any time, makes the domain walls even more intriguing. It is also important to note of that these domain walls are a product of both improper ferroelectricity and the geometry of the vortices.

2.4.6 Ferroelectricity in $Pb_5Ge_3O_{11}$

The transition from paraelectric to ferroelectric in $Pb_5Ge_3O_{11}$ consists of a range of displacements in most the atoms in the unit cell, and due to the size of the unit cell, the stacking of layers in figure 2.25 is most suitable to describe the transition.

In the parelectric phase, the structure can be explained by stacking two α layers and one β layer perfectly on top of each other with corner connected GeO_4 tetrahedons (forming the double tetrahedas), as described in section 2.6. As the temperature is decreased to the critical temperature, the tetrahedas and double tetrahedas experience tilting and twisting leading to the formation of the structure in figure 2.25(c)[38]. This mechanism is attributed to the instability of a soft TO phonon leading to a permanent displacement in one of the oxygen atoms of the GeO_4 tetrahedons. The transformation of the Ge and O structures then leads to shifts in the Pb atoms, causing the twisting of the trigonal prisms into metaprism leading to the polar state. Although this transformation is characterized as a displacive transition, previous articles are not clear on whether this is a proper or improper transition. The polarization does however originate in the Pb displacements triggered by the displacement of the GeO_4 tetrahedas which causes an optical active material, which in turn is triggered by one of the corner oxygen atoms of the same tetrahedas.

Regarding the domain structure, it can be seen to be either irregular or straight with 180° domains (polarization along the **c**-axis), and there are no intersection of the domain walls causing the domains to be enclosed loops[42]. However, with 180° domains and enclosed domains, at some point the polarization vectors must point head-to-head and tail-to-tail leading to charged walls whcih is unsual for a proper ferroelectric. In addition, the domain structure is particularly susceptible to damage from electron beams[9]. The domain structure is therefore categorized in to a starting domain structure (SDS) and a free domain structure (FDS), where the latter is primarily the SDS deformed or pinned

down by defects formed by strong electric fields (10-15 kV/cm). An important difference between two structures is that the domain walls of the FDS are irregular and mainly neutral, while the SDS contains straight and at some points charged domain walls that are screened by charges located in traps. While not reported, the presence of charged domain walls could imply a similar functionality as as seen with $ErMnO_3$. However, these domain walls are only reported in the SDS, so extra care must be taken to ensure this domain structure is maintained throughout the experiments.

2.5 $ErMnO_3$

$ErMnO_3$ have been mentioned several times in the previous chapters (chapters 1, 2.2.4 and 2.4.4), and several figures have been shown that reflect different aspects of the materials properties (see figures 2.9(c), 2.22(b) and 2.21). Still, no rigorous treatment has been made, and so the following chapter will go into detail on the systematic description of the crystal needed to interpret the results.

$ErMnO_3$ belongs to a class of functional materials called the hexagonal manganites (h-$R$$MnO_3$) which posess a range of interesting properties such as ferroelectricity, ferromagnetism, superconductivity, gigantic magnetoresistance, and some may couple to form new unexplored functionalities[43]. The various manganites (R = Er, Y, Sc, Dy, Ho, Tm, Yb, Lu) are quantitatively different (different T_N, T_C), but share the geometric ferroelectricity described in section 2.4.4. Since the ferroelectric properties are the main concerns, the first point to bring up is the phase transitions.

In the case of $ErMnO_3$, it undergoes two important phase transitions. The first occurs at 1470 K and the crystal changes from paraelectric ($P6_3/mmc$, space group 194) to ferroelectric ($P6_3cm$, space group 186) with a weak remnant polarization of around $6\,\mu Ccm^{-2}$, where both phases are hexagonal structures and the transition is illustrated in figure 2.21[5][18]. The second phase transition occurs at 79 K and changes the crystal from paramagnetic to ferromagnetic[5][44][19]. At room temperature it is therefore ferroelectric, with a unit cell as in figure 2.23. The polarization is best illustrated in terms of ionic displacement along the <100> directions, as in figure 2.21(b), and the polarization always points antiparallel with the **c**-axis. From these directions it can be found easily depending on the pattern of the Er atoms; if two out of three points up, then the polarization does too. This easily recognizable pattern ($\uparrow\uparrow\downarrow$, $\downarrow\downarrow\uparrow$) favours a plane-view of the <100> directions when it comes to sample preparations (chapter 3.2).

Since it is a hexagonal lattice, the lattice vectors are therefore as described in table 2.1, with the **c**-axis standing perpendicular to the **a** and **b** axis, which have a 120° degree angle between them. The length of **a, b** are 0.61 nm, and the length of **c** is 1.14 nm[45], with the primitive unit cell and its basis is listed in table 2.2[45]. It is also worth noting the symmetry of the crystal. The six-fold rotation symmetry along the **c**-axis allows us to only consider one of the six faces of the crystal as they are symmetrical (i.e. the [100]

[18] For comparison, the prototype ferroelectrics $BaTiO_3$ and $PbTiO_3$ has a remnant polarization of $25\,\mu Ccm^{-2}$ and $75\,\mu Ccm^{-2}$, respectively[41].

[19] This transition does not involve a change in space group.

and [010] directions are 120° apart and are therefore identical viewing directions). The two highest symmetry directions at one face are [100] and [210], which is in the direction of the corners and the center of the face. Any direction between these two can also be considered, but the other directions can always be represented by a direction lying between [100] and [210].

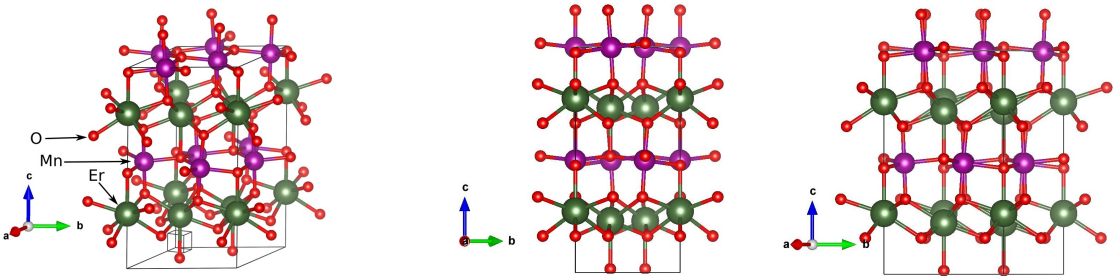

(a) (b) (c)

Figure 2.23: Schematic of the $ErMnO_3$ unit cell at room temperature at (a) the standarized direction, (b) the [100] direction and (c) the [210] direction.

Table 2.2: The primitive unit cell of $ErMnO_3$ with the placement the atoms inside the basis[46].

Atom	**a**	**b**	**c**
Er(1)	1/3	2/3	0.0435
Er(2)	0	0	0
Mn	0.3355	0	0.2747
O(1)	0.3070	0	0.1097
O(2)	0.3614	0	0.4377
O(3)	1/3	2/3	0.2549
O(4)	0	0	0.2705

The structure factor can then be calculated from equations 2.13 and 2.14, but since there are seven atoms to consider (three different elements), it will not give clear answers to the extinction rules. The $[0k0]$ is an exception though, as most atoms have zero y-components in the unit cell. The structure factor S_{0k0} then takes the form;

$$S_{0k0} = f_{Er} \cdot e^{-4i\pi k/3} + f_{Er} + f_{Mn} + f_O + f_O + f_O \cdot e^{-4i\pi k/3} + f_O \tag{2.72}$$

As the intensity is proportional to the absolute square of the structure factor, it is then proportional to:

$$|S_{0k0}|^2 = A^2 + B^2 + ABcos(4k\pi/3), \quad A = f_{Er} + f_{Mn}, \quad B = f_{Er} + f_{Mn} + 3f_O \tag{2.73}$$

This last equation reaches maximas for every k-value divisible by three, meaning the 000, 003, 006 reflections will become more bright than the ones in between, making the DP easily recognisable and the **c**-direction with it.

Simulations from the *JEMS* software showing the diffraction pattern from both parallell and conergent beam conditions along the <100> directions is shown in figure 2.24 for a thickness of 100 nm. The intensity of the reflections are represented by the size and opacity (darker means more intensity), and we can immediately find that the odd reflections along **c** is missing or forbidden. From the simulations, it is clear that polarization can not be found completely from kinematic SAED (figure 2.24(a)) as it is symmetric both perpendicular and parallell to the **c**-axis[16]. The orientation can however be found easily in the [100] direction, and the use of CBED (section 2.2.5) can give the actual direction of the **c**-axis (and thus polarization) as the contrast within the disks are not centrosymmetric. Especially the 004 and 00$\bar{4}$ disks in the simulation in figure 2.24(b) convey the most different contrast and can be used later for determining polarization. The CBED simulations are however extremely sensitive to variations in tilting around the zone axis, as can be illustrated by tilting just 0.1° degree off the [100] zone (see Appendix C).

(a)

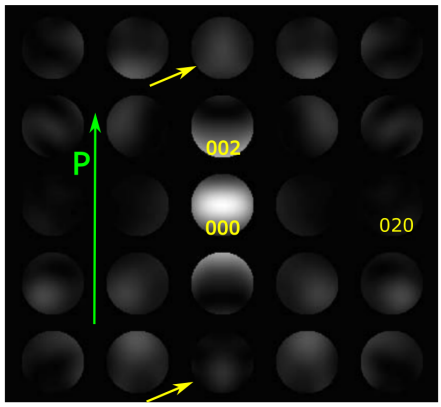

(b)

Figure 2.24: Simulation of diffraction pattern at 100 nm thickness from the *JEMS* software. (a) SAED along the <100> directions. The intensity of the reflections are represented by the size and opacity (darker means more intensity). (b) CBED simluations at 100 nm thickness along the same direction with spots turned into disks with non-centrosymmetric contrast inside. Only three disks are indexed to give the orientation and thus the polarization (green arrow), otherwise it follows the same as (a). The notable contrast difference in the 004 and 00$\bar{4}$ disks is indicated by yellow arrows.

2.6 $Pb_5Ge_3O_{11}$

$Pb_5Ge_3O_{11}$ or lead germanate is the second material that is studied in this thesis. Therefore, the necessary information and background regarding its ferroelectric properties and crystal structure is addressed here.

The ferroelectric domain structure in this material has been studied quite thoroughly by using optical light, X-rays and the SEM[12][11]. The domain structure was found to be irregular, and consisting of enclosed 180° domains with polarization along the **c**-axis, and early work was motivated by the different optical rotary power of opposite domains[13]. The phase transition occurs at 460 K with a remnant polarization of $4.6\,\mu Ccm^{-2}$[47], and changes the space group from $P\bar{6}$ (paraelectric) P3 (ferroelectric)[20]. The material is also found to have a large bandgap at 2.6 eV, making it nearly transparent as well as insulating[48].

Lead germanate does not belong to a class of similar materials as $ErMnO_3$, although the crystal structure can be described from a apatite polysomatic series[39]. Using this more general framework for describing the crystal is useful due to the complexity of the unit cell, and to simplify the discussion on phase transitions. The polysomatic series is based around apatite modules $A_{5N}B_{3N}O_{9N+6}X_\delta$, with different compositions of A, B and X atoms with different length N. The case for N = 3 is called the apatite polysomes ganomalites, and is the class that $Pb_5Ge_3O_{11}$ belongs to, although a general treatment of the $A_{5N}B_{3N}O_{9N+6}X_\delta$ module is more useful to begin with.

The modules can be divided into a framework consisting of BO_4 tetrahedras that are corner-connected to A^FO_6 triangular prisms, as well as isolated A^T atoms[21]. By combining these structures into a layer and stacking them on top of each other along the **c**-axis crystal lattice is formed. Furthermore, in an hexagonal unit cell there are two possible ways of combining the modules into layers (α and β) as illustrated in figure 2.25(a), where the only difference lies in how the components are oriented with respect to each other. This is however an idealized situation, since the real crystal lattice also contain a twist in the A^FO_6 triangular prism when two different layers meet, leading to a metaprism in addition to a rotation of the tetrahedras (figure 2.25(c)). Figure 2.25(b) shows an example of a stacking sequence $\alpha\alpha\beta\alpha\alpha\beta$ in the ideal case, and figure 2.25(c) shows the real structure with the interface boundaries and resulting twisting. This particular stacking, $\beta(\alpha\alpha\beta)^N\alpha$ is the principle form of $Pb_5Ge_3O_{11}$ and other ganomalite structures, and is more useful to work with than the unit cell.

Representing the structure in terms of the unit cell could also be done however, and the unit cell is shown in figure 2.26 with the atomic placements as in table (ref). In the ferroelectric phase, it is a primitive hexagonal structure (space group P3) as described from table 2.1, with $\mathbf{a} = \mathbf{b} = 1.03$ nm and $\mathbf{c} = 1.07$ nm. The two zone axes [100] and [001] is represented in figures (b) and (c), with the remaining high-symmetry zone axis, [010] being identical to [100]. Along the **c**-axis, there is a three-fold symmetry, which results in a six-fold symmetry in the DP due to Friedel's law (section 2.1.2). It is worth noting that due to the appearence of the unit cell, the direction of the **c**-axis is not easily determined from the atomic placements, and so high resolution techniques are not necessarily suited to reveal details on the domain structure, even with an abberation corrected microscope. The (100) planes are also cleavage planes, which can make the

[20]Space group $P\bar{6}$ is number 174 and P3 is number 143.

[21]The *F* stands for framework, while the *T* stands for tunnel, indicating they are played inside the tunnel of a larger structure.

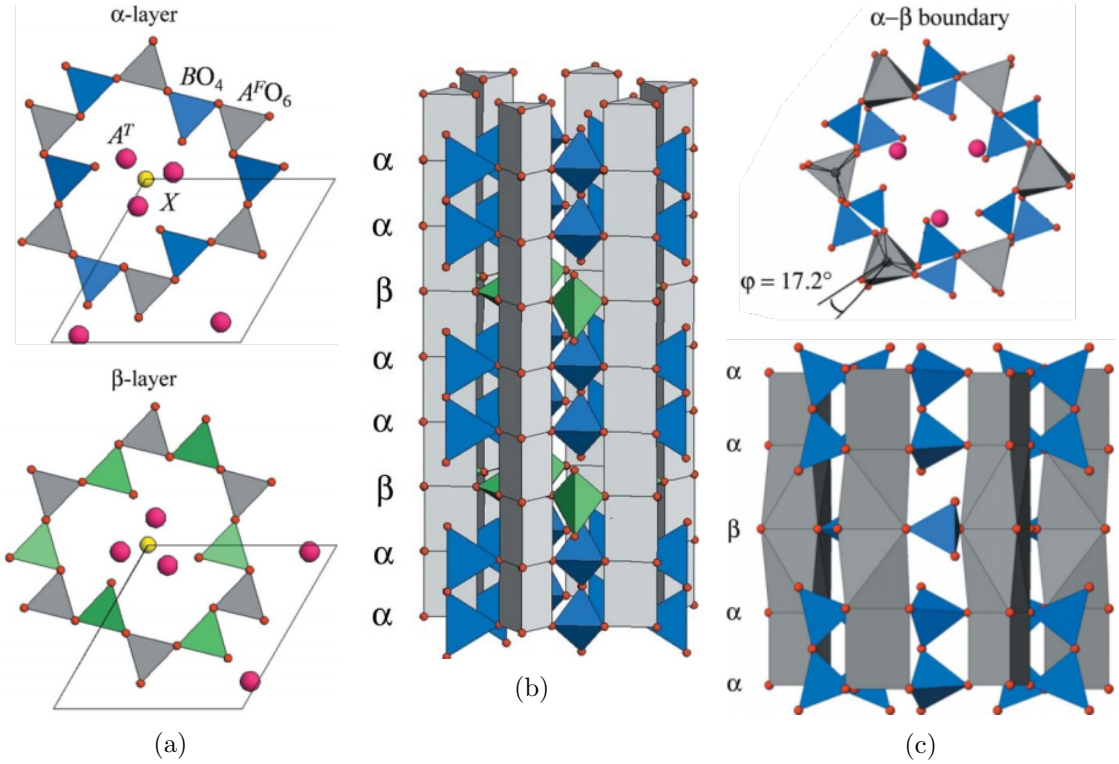

Figure 2.25: (a) The two types of layers of the polysomatic apatite series along the **c**-axis. (a) The ideal stacking sequence for N= 3, which is the ganomalite series that includes $Pb_5Ge_3O_{11}$. Images are taken from [39].

[100] direction favourable for preparing samples[49]. The structure factor can in principle

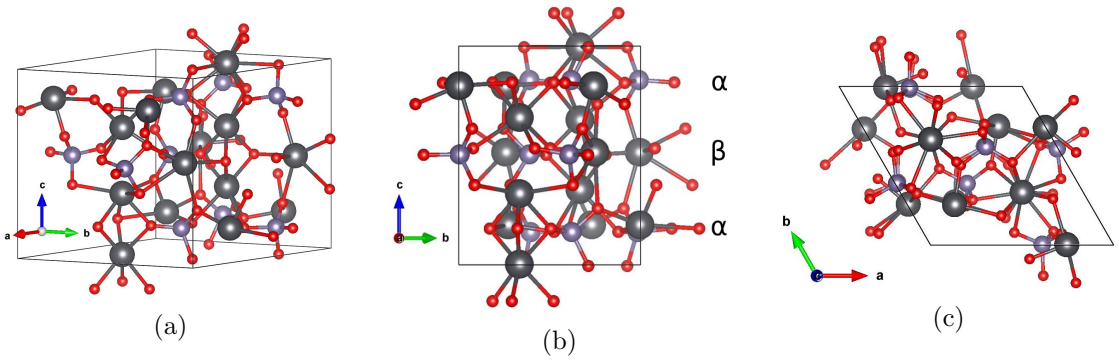

Figure 2.26: The unit cell of $Pb_5Ge_3O_{11}$ along (a) the standard orientation, (b) the [100] direction and (c) the [001] direction.

be derived for this material as well, but due to the number of atoms in the unit cell this is challenging, even with simplifications as was done for $ErMnO_3$. Simulations on

Table 2.3: The primitive unit cell of $Pb_5Ge_3O_{11}$ in the ferroelectric phase with the placement the atoms inside the basis[50].

Atom	**a**	**b**	**c**	Atom	**a**	**b**	**c**
Pb(1)	0.269	0.272	0.183	O(1)	0.093	0.328	0.258
Pb(2)	0.258	0.255	0.819	O(2)	0.087	0.325	0.735
Pb(3)	0.333	0.667	0.345	O(3)	0.122	0.597	0.151
Pb(4)	0.333	0.667	0.663	O(4)	0.087	0.584	0.832
Pb(5)	0.667	0.333	0.326	O(5)	0.829	0.323	0.166
Pb(6)	0.667	0.333	0.674	O(6)	0.814	0.292	0.834
Pb(7)	0.333	0.667	0.997	O(7)	0.073	0.360	0.995
Pb(8)	0.667	0.333	0.003	O(8)	0.288	0.481	0.503
Pb(9)	0.251	0.993	0.515	O(9)	0.582	0.503	0.533
Ge(1)	0.017	0.395	0.150	O(10)	0.372	0.285	0.365
Ge(2)	0.009	0.389	0.845	O(11)	0.320	0.247	0.623
Ge(3)	0.393	0.388	0.505				

SAED and CBED diffraction from *JEMS* is therefore shown in figure 2.27 along the [100] direction. Same as for $ErMnO_3$, there is a repeating pattern of two weak and one strong reflection, except here it lies along the **c**-axis. This repeating pattern is thought to originate in the stacking of two α layers and one β layer, just as the repeating $\uparrow\uparrow\downarrow$ pattern does in $ErMnO_3$. Furthermore, the CBED pattern in figuere 2.27(b) shows a clear asymmetry along the **c**-axis, where for instance the $02\bar{1}$ and 002 shows a clear difference to their counterparts 021 and 002. This implies the polarization direction is far easier to read from CBED and off-axis STEM techniques than in $ErMnO_3$, where the difference between disks along the **c**-axis is only weak. The disks can also be seen to contain more uniform intensity distribution than in $ErMnO_3$. Revisiting the theory on dynamical diffraction and the two beam equation in 2.42, the most likely explanation is that the extinction parameter is very small. In turn, this means fluctuations in the deviation parameter will not be as important as the effective deviation parameter is mainly determined by the large contribution from the extinction parameter. With the many beam extension in equation 2.47, the picture is complicated further so a complete insensitivity to deviation parameter shifts may not be the case. The thickness will however also be affected by a small extinction parameter and result in more frequent oscillations and amplified outside the main disk.

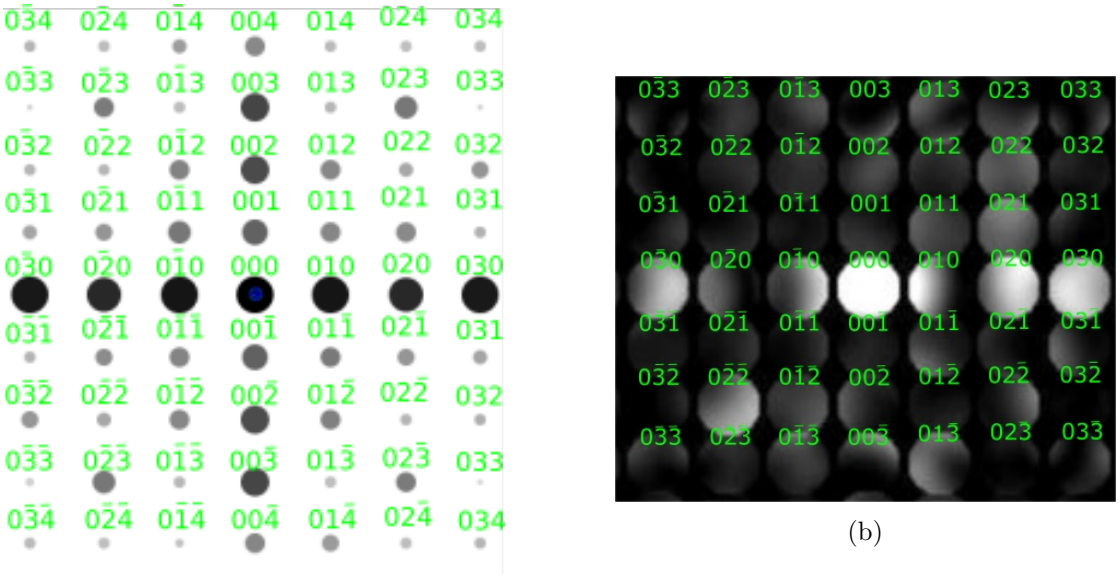

(a) (b)

Figure 2.27: Simulation of diffraction patterns at 100 nm thickness along the [100] direction from the JEMS software. (a) SAED and (b) CBED patterns. The indexing is the same, and the polarization is along the **c**-axis (green arrow). For the CBED pattern, a total of 440 reflections are used, all entering as strong reflections in the simulation.

Chapter 3

Experimental Techniques

3.1 SEM Techniques

A *Hitachi S-5500 S(T)EM* (referred to as the S-5500 microscope) and *FEI APREO SEM* (referred to as the APREO microscope) was applied to supplement the TEM results allowing for overview images of TEM specimens before and after they had been characterized in the TEM. The SEM microscopes were operated at energy values between 0.5 keV and 30 keV, specified in the images. Beam current is also varied to prevent excessive charging of the specimens, ranging from 0.5 pA to 20 µA. Typical values in this work are 1.5 keV acceleration voltage and 5 µA beam current for $ErMnO_3$, and 5 keV and 0.1 nA for $Pb_5Ge_3O_{11}$. In the S-5500 microscope only the secondary electron detector is used with a STEM holder that can use TEM grids directly. The APREO microscope did not have a holder for TEM grids, so the grids were placed in the middle of circular metal disks glued together with silver paint with a circular hole in the middle. The use of glue to holds grids in place resulted in charging effects and could not be used. This microscope also has the standard detector (the Everhart-Thornley detector or ETD) mounted far away from the specimen, so to enhance contrast and resolution the immersion mode is sometimes used. A strong magnetic and electric field is then applied to the specimen focusing the emitted electrons into the lens where an additional detector called T2 is placed. The use of immersion mode or standard mode is indicated by the T2 or ETD label in the bottom of the figure.

3.2 TEM Specimen Preparation

The main technique applied to prepare plan-view TEM samples of monocrystalline $ErMnO_3$ and $Pb_5Ge_3O_{11}$ is a mechanical tripod polishing routine, with Ar-ion milling for final thinning. Since the material was prone to break at the final stages of the polishing when the specimen are very thin, several samples were made with different orientations and slightly different procedures (see appendix A for step by step procedure). Some samples were made by polishing alone, while others were made by a combination of polishing and ion milling. The procedure is based on the work of Eberg, Monsen,

Tybell, van Helvoort & Holmestad[43]. Silver paint was applied on finished TEM specimens covering both specimen and grid if the specimen experienced charging effects in the TEM. In addition, some specimens were prepared by grinding bulk material into a powder with a pestle and mortar that is deposited onto a TEM grid. In total, 14 specimens were prepared for the TEM, categorized into four types (A, B, C and D). These included seven specimens of $Pb_5Ge_3O_{11}$, four by tripod polishing and three from powder samples, and seven specimens of $ErMnO_3$, five by tripod polishing and two from powder samples. Table 3.1 shows an overview of the specimen types made and how they are categorized.

Table 3.1: Types of specimens that is prepared, with preparation technique and intended direction of the **c**-axis.

Specimen type	Preparation method	**c**-axis orientation
A	Tripod polishing	In plane of specimen, parallell to edge
B	Tripod polishing	In plane of specimen, perpendicular to edge
C	Tripod polishing	Out of plane of the specimen
D	Pestle and mortar	Random

3.2.1 Tripod Polishing

Mechanical polishing have been shown to be advantageous over conventional milling for preparing perovskite samples, as it does not introduce significant defects, artefacts or amorphous layers[43]. In addition, this techniques makes it possible to produce larger areas ($> 1000\,\mu m^2$) of electron transparent material at a controllable varying thickness, in contrast to other conventional techniques such as Focused Ion Beam (FIB)[20][51]. It is therefore used as the main technique to obtain thin quality samples, and the outline of the procedure is illustrated in figure 3.1.

Beginning with large slabs of the material, they were cut with a *Testbourne Model 60 Low Speed Diamond Wheel Saw* using a 150 µm thick *Allied Wafering Blade* into (1-2 x $1\,mm^2$) slabs while being mounted on a glass slide with wax. The samples were then attached to a pyrex sample holder using super glue, which had already been polished flat with a 6 µm diamond-lapping film (DLF).

The samples were then polished with *Allied Multiprep System*, using DLF's with grain sizes of 15 µm, 6 µm, 3 µm, 1 µm, 0.5 µm and 0.1 µm rotating at 30 rpm[21]. Each grain size removes material about three times the size, and had to be washed away with water, except for the last three steps where *Allied GreenLube* were used. In addition, the sample was oscillating with about half a plate radius. A load of 200 g was applied during the polishing with the 15 µm, 6 µm and 3 µm DLF, but removed for smaller grain sizes to avoid edge chipping. In the final step the sample was polished with a polyurethane cloth stained with a buffered silica (SiO_2) solution with 0.02 µm sized particles (*Allied Colloidal Silica Suspension*), which was later washed off with soap and rinsed in water. Figure 3.1 shows schematically the stages of sample preparation by mechanical polishing,

with a schematic of the polishing system.

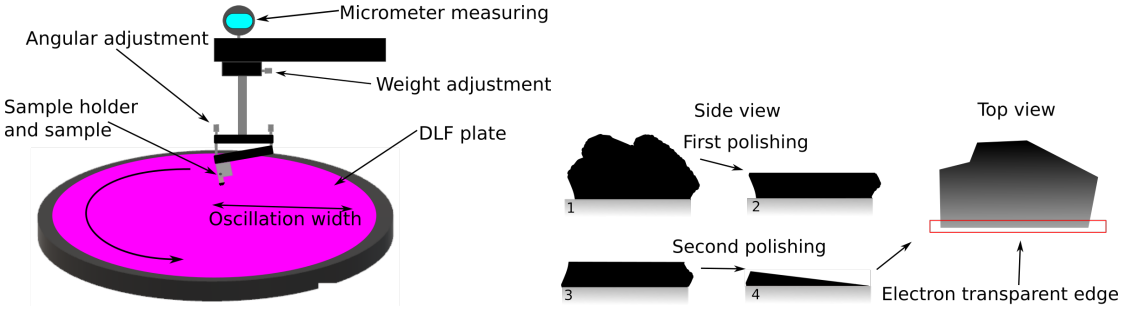

(a) (b)

Figure 3.1: (a) Schematic of a mechanical tripod polishing system. The DLF plate roates while the sample is pushed down at the plate with a certain weight and angle, oscillating about half the plate radius. (b) Side-view of the sample under the different stages of polishing; first glue onto pyrex, then polish one side, flip the sample and then polish into a wedge. Top-view image illustrates the ideal case, where the whole region of interest is electron transparent.

In figure 3.1(b), the side-view of the sample preparation is shown. The first image is of a sample glued onto the pyrex with a rough surface. It is then polished flat with the roughest 15 µm DLF, and further polished with all the smaller grain sizes to ensure a smooth surface. At each step the sample was inspected in an *ZEISS Axio Scope* visible light microscope (VLM) for scratches or edge chipping. The sample was then detached from the pyrex using acetone, then rinsed in ethanol before being attached again with the polished side facing into the pyrex as in the second and third figure.

The second side was first polished down to 500 µm using the roughest 15 µm DLF. Then an 2° angle was introduced, and the sample was polished down to 60 µm using DLF's down to 3 µm. With a 1 µm DLF, the sample was polished in steps of 30 s, until thickness fringes were visible in an optical microscope or until the edge started to chip off. 0.5 µm and 0.1 µm DLF's was then applied in steps of 15 s, until thickness fringes becomes more pronounced and scratches were reduced. Finally, 0.02 µm colloidal silica was then applied for 1 minute as the final stage of the polishing. The whole procedure is summarized in table 3.2. The specimen was then detached from the pyrex using acetone and ethanol, and placed onto a *Omniprobe Lift-out Grid* of Mo or Cu using *Biltema Quick-Epoxy* two-part glue.

3.2.2 Ion Milling

Should the sample prove to be too thick after inspecting in the TEM, then further mechanical polishing is not possible. Ion milling can however be implemented after gluing the sample to a TEM grid, and can be used to get thinner samples. There are however possibilities of introducing defects and amorphous layers to the sample that

Table 3.2: Overview of procedure for mechanical polishing.

	First side polishing		Second side polishing	
DLF	Polishing duration	Load	Polishing duration	Load
15 µm	Until flat	200 g	Down to 500 µm, then to 250 µm at 2°	200 g
6 µm	Polish off 50 µm	200 g	Down to 150 µm at 2°	200 g
3 µm	Polish off 20 µm	200 g	Down to 60 µm at 2°	200 g
1 µm	Polish off 10 µm	50 g	Steps of 30 s at 2°	0 g
0.5 µm	Polish off 0.1 µm	50 g	Steps of 15 s at 2°	0 g
0.1 µm	Polish for 15 s	50 g	Steps of 15 s at 2°	0 g
0.02 µm	Polish for 1 min	0 g	1 minute at 2°	0 g

could potentially disturb the ferroelectricity, so the method was only applied as a final effort to get electron transparent material[52].

A *Gatan precision ion polishing system-2* (PIPS II) was used, with Ar-ions accelerated to a voltage of 3.0 kV, 2.5 kV, 2.0 kV, 1.5 kV, 1.0 kV, 0.5 kV and 0.1 kV by two guns with an angle to the sample of less than 10° while cooling the sample down to 123 K. Three main milling routines were used. The first is the dual modulation mode that included an 8° angle between both guns and rotation of the specimen under constant radiation. This allows for an even milling of the specimen, but it may also blunt the edge instead of thinning. The second routine is the stationary single gun mode, where the specimen was kept stationary with the rear end of specimen towards the one gun while milling once from the top at 5° and then once from the bottom at −8°. This routine is better suited for thinning than the previous, but may cause uneven thinning since the guns may not radiate isotropically. A final routine is the single modulation mode, which is similar to the first routine, except here the guns are only active when the rear end of the specimen faces the guns. Using the same angles as for the stationary mode, this technique ensure evenly thinning of the specimen.

The exact duration of milling varied from specimen to specimen, and since the thickness have not been measured precisely it is difficult to quantify the milling rates. Therefore, rounds lasting for 7, 14 or 21 minutes were used where the specimen where checked in the TEM after each round. This was done to ensure that the specimen was not milled beyond what is necessary to avoid defects as much as possible. Each round consists of equal time spent at each voltage step (1, 2 or 3 minutes at each step), as the higher voltage steps will thin the specimen while the lower steps reduces the amorphous layer created by the first steps.

3.2.3 Pestle and Mortar

A pestle and mortar was also used to create TEM specimens. This preparation is applied due to its efficiency and cleanliness, allowing specimens to be created with electron transparent regions without introducing any contamination and surface defects (scratches or cracks) and without ion milling. Grinding and crushing a bulk sample into a powder in

isopropanol can be used to obtain small flakes (about a few micrometers wide) with a large flat surface. The isopropanol/powder solution is then dripped onto a holey carbon Cu mesh grid. After the liquid is evaporated, the particles is left on the grid with a majority aligned with the cleavage plane facing down into the grid. Since the (100) planes are cleavage planes in $Pb_5Ge_3O_{11}$, this viewing direction is most likely to appear with the **c**-axis then lying in the plane of the grid.

3.3 TEM Techniques

The TEM results were taken from one of two microscopes; a *JEOL JEM 2100* (referred to as the 2100 microscope) with a LaB_6 thermionic gun or a *JEOL JEM 2100F* (referred to as the 2100F microscope) with a FEG, both operating at 200 kV. The 2100 was equipped with a *Gatan 2k Orius* CCD camera, while the 2100F used a *Gatan 2k Ultrascan* CCD camera. In addition, EDX data was collected with a *Oxford Instruments Aztec EDX* on the 2100F and 2100 to observe contamination from the preparation stages. Some data was also replotted using Matlab. A double tilt holder with tilting ranges $\pm 30°$ were always used, and some of the samples were oxygen plasma cleaned (indicated in figure caption).

All the samples that had electron transparent regions were viewed in the TEM, but only a few images selected from various samples are shown. Conventional techniques includes HRTEM images of the amorphous layers formed by the ion milling, BF and DF images to give an overview of regions of interest, SAED patterns for finding the crystal orientation and CBED patterns for finding local polarization. As the CBED method uses a convergent beam with a convergent angle α that depends on both the condenser aperture and ALPHA knob, a certain combination of the two variables had to be tested (see Appendix B for calibration plot). The optimal combination for $ErMnO_3$ turned out to be the second smallest aperture (50 µm) with the ALPHA 7 setting in CBED mode on the 2100 micropscope, while for the 2100F microscope a good combination was not found due to apertures being either too large or too small. For $Pb_5Ge_3O_{11}$ the ideal combination was found using the 10 µm aperture on the 2100F microscope, with ALPHA 3 setting in TEM mode.

In addition to conventional techniques, STEM techniques were applied including HAADF-STEM for local high-resolution and overview information, off-axis STEM using HAADF detector for overview information on regions of interest and STEM-EDX. Some of the high-resolution HAADF-STEM images were also taken using SmartAlign.

3.4 Data Handling and Simulations

For simulations of CBED patterns, the *JEMS* software based on Bloch-wave dynamical scattering was used with varying thicknesses and laue-zone centers (referred to as tilting). In most simulations, the total number of reflections used in equation 2.33 was at 150, while around the same amount of weak beams was introduced through perturbation

theory. SAED patterns were also simulated using the same software, but unless specified these are purely kinematic.

All the images taken were also processed in *Gatan DigitalMicroscope* (DM). Mostly this was used to set the maximum and minimum intensity ranges to amplify weak contrast, but a few images were also filtered either using the DM built-in spatial filters to sharpen or smoothen the image, or by applying a bandpass filter to the FFT and displaying the inverse FFT. Any filtering is specified in the figure caption.

Chapter 4

Results and Discussion

The following chapter will present the results obtained in thesis along with a discussion. As stated in chapter 1, the two main goals of the thesis is to establish a routine for studying ferroelectricity using a correlated SEM/TEM set-up with the tripod polisher, and to investigate techniques to study the domain structure of $Pb_5Ge_3O_{11}$. Since the specimen preparation is a core part of the thesis with tripod polishing never tested before on these materials, the first section goes into detail on the routines used and the drawbacks of the different specimen types. The second section focuses on charging effects and beam damage in $Pb_5Ge_3O_{11}$, specifically on how the electron beam can degrade the specimen in different operation modes (TEM and STEM) and the critical doses for each effect. In the third section the correlated SEM/TEM routine with the tripod polisher is demonstrated on $ErMno_3$ to reach the first goal. The last section repeats the procedure on $Pb_5Ge_3O_{11}$ as far as possible to reach the second goal, but also includes techniques not necessary in $ErMnO_3$ due to the specific domain structure and charging effects.

4.1 Sample Preparation

Tripod Polishing

Since high specimen quality is vital to obtaining good TEM results and especially for techniques requiring high resolution, results from tripod polishing, crushing and grinding bulk and ion milling is important to give a thorough examination. In addition, the first two steps are the only point throughout the thesis where strain is applied to the material which can expose some of the mechanical properties. Figures 4.1(a) and 4.1(b) show two $ErMnO_3$ specimens prepared by tripod polishing of type A and B, respectively, taken during the project thesis. It was verified that the tripod method produced large areas of electron transparent material (>1500 µm edge), but with a few scratches present and significant edge chipping for type A. For this type of specimens, the edge consisting of a stair-case pattern, with elongated steps in parallel the edge compared to perpendicular to it, indicating that the material was prone to break along the **c**-axis. Type B specimens produced a different edge that was thinner and more fragmented, with little edge

chipping.

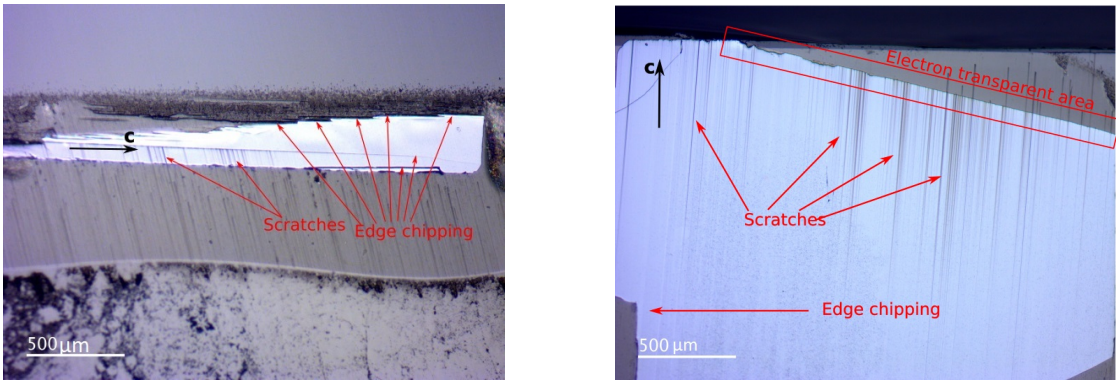

(a) (b)

Figure 4.1: VLM images of TEM specimens prepared by tripod polishing. (a) shows a type A $ErMnO_3$ specimen ($ErMnO_3$ is white due to reflection) at the final stage of tripod polishing while still glued onto the pyrex. For this type of specimens large portions of the edge broke off. (b) shows a type B $ErMnO_3$ specimen that produced large electron transparent regions. The (100) planes also lie in the plane of the specimens.

Preparing tripod specimens of $Pb_5Ge_3O_{11}$ produced a similar result as for $ErMnO_3$ and type A and B specimens are shown in figures 4.2(a) and 4.2(b), respectively. Both types have resembling features of the $ErMnO_3$ specimens; a large electron transparent edge (>1200 µm) with a significant amount of scratches present. Type B specimens shows a longer and more fragmented edge compared to the type A specimen, which was straighter and some regions indicated that the edge began to chip off bits. The yellow box in figure 4.2(a) indicate such a region, however the effect is far less pronounced than in the $ErMnO_3$ counterpart (figure 4.1(a)). Since $Pb_5Ge_3O_{11}$ has a reported cleavage plane along the (100) plane, this is the most probable cause of the edge breaking off bits, and with the similarity between the two materials, it is therefore likely that the (100) plane is also a cleavage plane in $ErMnO_3$. A more pronounced effect may stem from a lower ductility in $ErMnO_3$ compared to $Pb_5Ge_3O_{11}$, although a value for this property is unreported in both materials.

A further comparison between the two specimen types was done during the project thesis on $ErMnO_3$ as shown in figure (4.3). Figure 4.3(a) shows an overview TEM image of the edge with an SAED pattern in the bottom right corner. The edge is clearly fragmented up to a 1 µm from the edge which equals 35 nm thickness difference. With a fixed incline at 2°, thickness variations, Δt, when moving a distance L into the specimen are easily calculated using $\Delta t = tan(2°)L$. Additional peaks in the SAED pattern of the edge are found and indicate that the fragments have orientations different from the bulk crystal. In addition to the fragmented edge, there is also cleaving along the cleavage plane lying perpendicular to the edge, resulting in a cleft where contamination builds up. Figure 4.3(b) shows a close-up in the cleft, which displays small spherical particles.

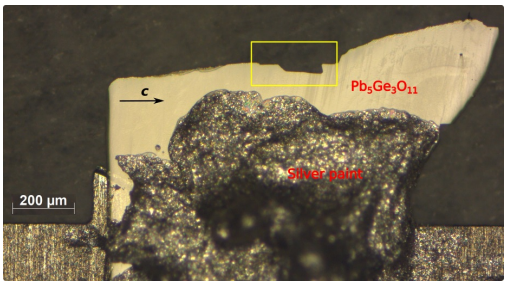

(a)

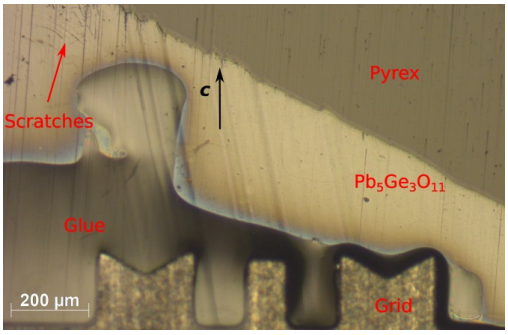

(b)

Figure 4.2: VLM images of TEM specimens prepared by tripod polishing. (a) a type A $Pb_5Ge_3O_{11}$ specimen ($Pb_5Ge_3O_{11}$ is paler than $ErMnO_3$ as it partially transparent) after it is glued onto a Mo TEM grid and after the silver paint is applied to reduce charging effects. The yellow box indicate a region suffering from edge chipping. (b) a type A $Pb_5Ge_3O_{11}$ specimen after it is glued onto the Mo grid. The entire edge in both images is usable in a TEM.

An EDS spectrum is obtained from the region in the yellow circle and compared to bulk in figure 4.3(c), which shows strong peaks for Si and O and only weak peaks for the Er and Mn elements. The colloidal silica (SiO_2) used in the tripod polishing is then the source of the contamination, and this specimen type with cleaving perpendicular to the edge is especially susceptible to storing contamination.

As a final thinning process, ion milling was frequently applied to the specimens after the tripod polishing. This procedure is not an ideal solution as it forms amorphous layers surrounding the specimen which reduces the contrast of the images. Figures 4.4(b) and 4.4(a) shows a type A $ErMnO_3$ specimen (taken during project thesis) and type C $Pb_5Ge_3O_{11}$ specimen, after ion milling. The $ErMnO_3$ specimen was milled for 7 minutes using dual modulation (see section 3.2), and a resulting amorphous layer of approximately 3.8 nm wide can be seen at the edge. The $Pb_5Ge_3O_{11}$ specimen was slightly thicker after the tripod polishing, and needed 28 minutes in two rounds, the last displayer here, using the stationary single gun mode. The first round of 14 minutes resulted in a layer around 1.5 nm, while the second resulted in a layer of approximately 4.5 nm. A complete quantification of the milling rates and resulting amorphous layer is beyond the scope of this thesis, but neither of the values given above are significant compared to the thickness of the bulk specimen which can produce HRTEM contrast even up to 100 nm thickness. The ion milling procedure is therefore deemed safe to use for both materials in rounds of 14 minutes, 2 minutes at each voltage step, with inspection in between rounds to avoid over milling.

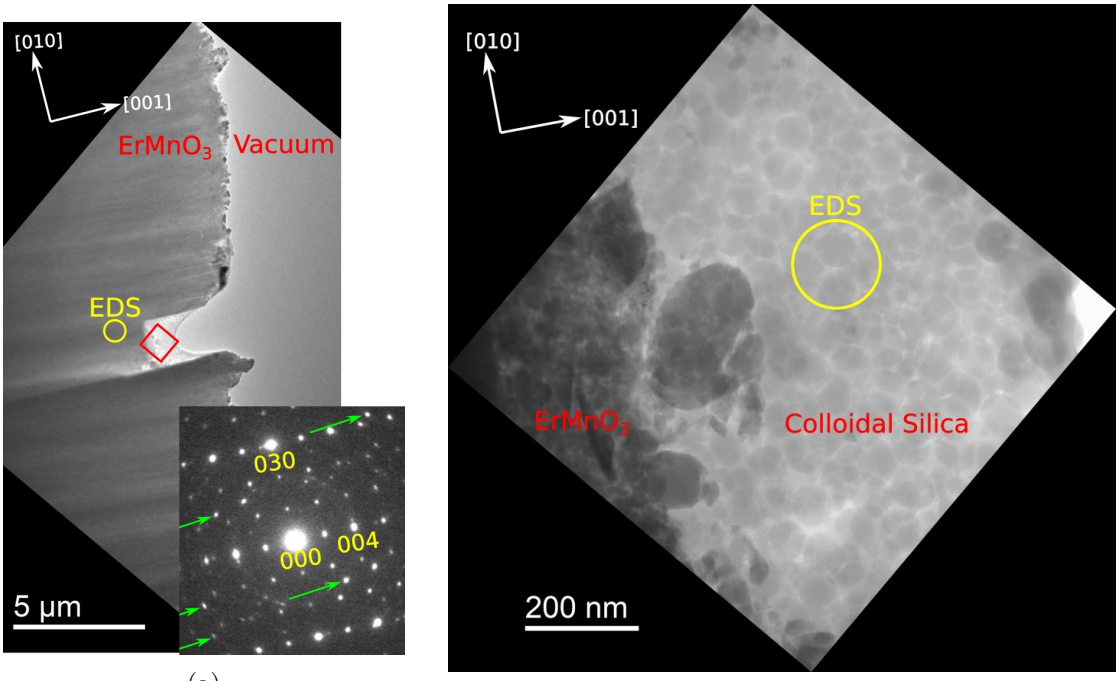

Figure 4.3: TEM images of the edge of a type B $ErMnO_3$ specimen, with EDS of contamination. (a) shows an overview of the edge, with the region used for EDS of bulk material (yellow circle) and region for (b) (red square). The SAED pattern in the bottom right corner is taken from the edge and shows additional reflections (green arrows) to the ordinary pattern in figure 2.24(a). (b) shows a close-up of the cleft containing large amounts of contamination, and the yellow circle indicate the second region used for EDS, which is shown in (c) with peaks identified by the *Aztec* software. Images are taken with the 2100 microscope.

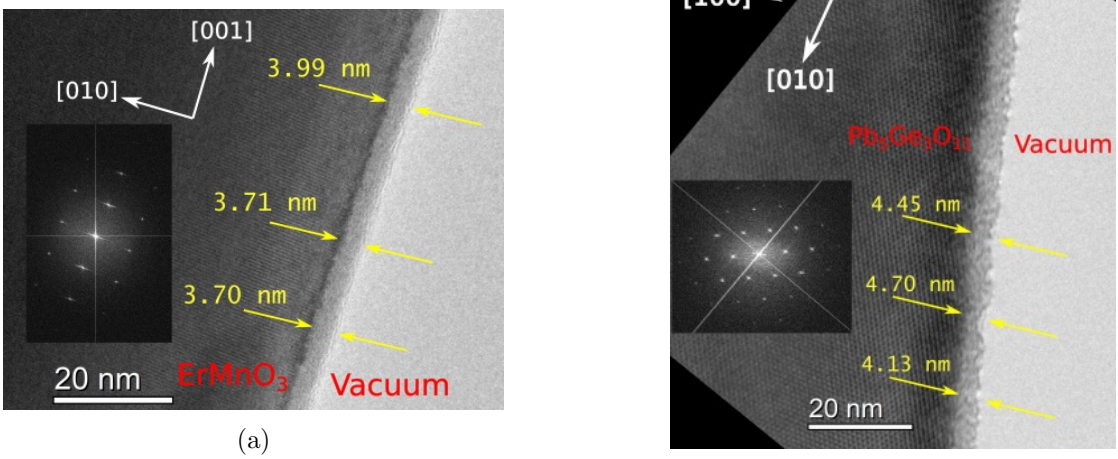

(a) (b)

Figure 4.4: HRTEM images of the edge of type A $ErMnO_3$ specimen and type C $Pb_5Ge_3O_{11}$ specimen, after ion milling. (a) shows $ErMnO_3$ after dual modulation milling for a single 7 minute round, and (b) shows $Pb_5Ge_3O_{11}$ after stationary single gun mode after two 14 minute rounds. Both images display an FFT to better show the lattice contrast. Images are taken with the 2100 microscope.

With the results presented above, the tripod technique is demonstrated to be successful for all the different specimen types for both materials, despite cleavage planes causing parts of the edge to break off. In fact, in type A specimens this cleaving leads to straight edges that are too thick for a direct TEM study, but combined with ion milling leads to high quality specimens with minimum contamination. Specimen of type B on the other hand results in a thin, but fragmented edge for about 1 µm into the material which leads to an additional 35 nm of thickness. The specimen type A is therefore recommended for further TEM experiments on these materials (or type C with cleavage plane parallel to edge), while type B is only recommended for its efficiency, as ion milling and subsequent TEM inspections is a time consuming effort.

Pestle and Mortar Specimen Preparation

TEM specimens can be prepared by crushing bulk material into a powder. Due to the existence of cleavage planes in both materials, the remaining microparticles are likely to have large flat surfaces along the (100) planes and wedges resulting in electron transparent regions. Figure 4.5 shows a SEM and TEM image of micro particles for each materials. The SEM image of the $Pb_5Ge_3O_{11}$ cluster, figure 4.5(a), shows the surface of the largest particles to be mostly flat, but some parts are fragmented. A similar particle is found in the $ErMnO_3$ specimen, where a TEM image is shown in figure 4.5(b). The DP along the [100] zone axis was obtained after small tilting ($<5°$) which means the particle is resting on the holey carbon film (barely visible) with the (100) plane. The same

result was found for the $Pb_5Ge_3O_{11}$ specimens, as they have the same cleavage planes. Furthermore, the edge can be seen to be electron transparent and of high quality due to the absence of ion milling or any contamination from the preparation process. The technique is therefore highly potent for bulk examination, although the small size of the particles and rough edge does not allows for tracking domain structures for more than a few hundred nanometers.

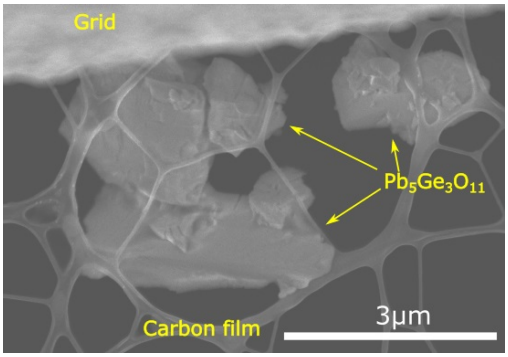

(a)

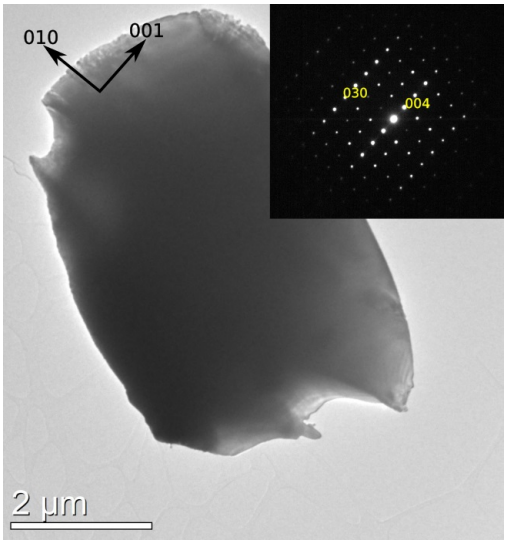

(b)

Figure 4.5: Images of TEM prepared by pulverizing bulk material. (a) shows a SEM image of a cluster of $Pb_5Ge_3O_{11}$ particles, in addition to the Cu grid and holey carbon film. (b) shows a TEM image of a $ErMnO_3$ particle, with the DP in the top right corner obtained after only small tilting ($< 5°$).

4.2 Beam Damage and Sensitivity in Lead Germanate

Beam damage is a common problems associated with electron microscopes, and in some materials form fundamental limits to the amount of data that can be extracted[53]. These effects include heating of the specimen, electrostatic charging, damage from ionization and resulting decomposition of the compounds (radiolysis), displacement of nuclei into interstitial positions and sputtering of surface atoms, all of which can be described from the scattering processes in section 2.7. Furthermore, each of the processes depend on a number of microscope parameters such as the dose rate (electrons per time), accumulated dose (charge deposited per area), beam diameter and electron energy as well as material parameters such as thickness and zone axis[54].

Problems from the electron beam are not raised for $ErMnO_3$ in scientific papers, and only charging is mentioned in $Pb_5Ge_3O_{11}$[14]. However, during the presented work

$Pb_5Ge_3O_{11}$ displayed both charging and beam damage to the extent that certain experiments could not be performed. More specifically, charging effects limited the amount of DF experiments that could be done since charging stretched out the diffraction reflections making it challenging to identify and select the correct reflections with the objective aperture. HRTEM also posed a challenge as small nanometer sized particle would frequently emerge after short exposure to the electron beam. In addition, the material quickly transformed from crystalline to amorphous under high intensity irradiation in STEM mode. Neither of this have been reported, so the nature of these effects is therefore investigated to extract critical parameters and to better discuss the importance of the defects for further work on the ferroelectric domain structures. It is however beyond the scope of this thesis to give a review of all the parameters, so only a few is tested to give a sense of the values involved for $Pb_5Ge_3O_{11}$. Most importantly will be the critical dose for the emergence of a single nanoparticle, and the rate at which the material becomes amorphous. These findings will give the maximum dose that can be applied in TEM and STEM studies for visualizing the domain structure and the atomic arrange at domain walls.

In figure 4.6, a series of images is shown of the particles evolving over time under constant irradiation in TEM mode. The initial state (4.6(a)) shows no nanoparticles, while after 3 minutes (4.6(b)) a few begin to appear indicated by green arrows. 10 minutes later (4.6(c)), more and larger particles have appeared, and after 40 (4.6(d)) minutes the bulk crystal is disappearing in favour of the nanoparticles. The green arrows are held at a fixed point assuming no drift between images, and show how the edge is creeping inwards to the bulk material. The particles can also be seen to merge as they grow larger, or in some cases lie on top of each other. This series was taken in a type D specimen, and the selected particle was not oriented beforehand to minimize prior exposure, although it was close to the [100] zone axis. In addition, an image of vacuum under the exact same microscope settings (same brightness and magnification, 200 µm condenser aperture) was taken to find the average number of electrons passing through each 0.069 nm pixel to be $1.91 * 10^3$ over an exposure time of 0.2 seconds[1].

A few key observations and calculations can be found from the figures. A few smaller particles begin emerge around the 3 minute mark, so this time period can be set as the first critical defect time (before the onset of nanoparticles), T_{d_1} for the nanoparticles under this intensity. The second critical time is the point where the amount of defect nanoparticles becomes comparable to the bulk material, T_{d_2}, in this case after 10 minutes. The quantity of interest is then the critical dose for these time periods. Dose is a measure of total charge deposited per area[2], and therefore expressed as $D = I_e T_c$, where I_e is the intensity of electrons expressed in the deposited charge per unit time and area. Using the measured values in vacuum above, the electron intensity is calculated to be $32.1 \frac{C}{s\,cm^2}$.

[1] The CCD camera count is converted into number of electrons by using a conversion factor provided by D. Lundeby and B. Soleim.

[2] Although this is a conventional definition of dose, there are different definitions using the dose rate or dose per unit mass[55].

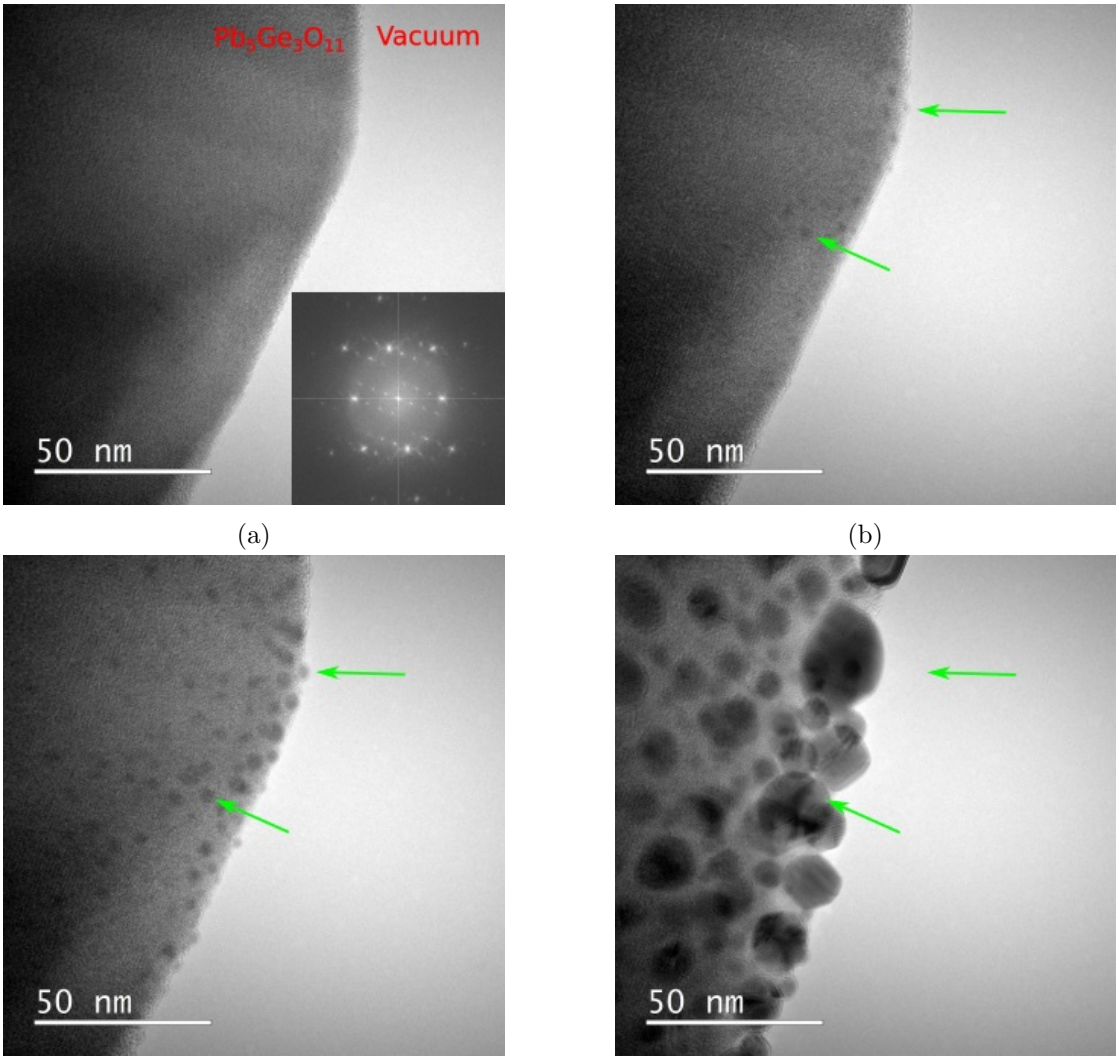

Figure 4.6: TEM images of nanoparticles emerging in a type D $Pb_5Ge_3O_{11}$ specimen. (a), (b), (c) and (d) shows the same region after 0 minutes (initial state), 3 minutes, 10 minutes and 40 minutes, respectively. The FFT in the lower right corner of (a) shows the zone axis the be slightly off, but lattice contrast is still present. Images are taken with the 2100F microscope.

The first dose, D_{d_1}, is then $5.78 * 10^3 \frac{C}{cm^2}$ (or $3.61 * 10^6 \frac{e}{\mathring{A}^2}$[3]), and the second, D_{d_2}, is $1.93 * 10^4 \frac{C}{cm^2}$ ($1.20 * 10^7 \frac{e}{\mathring{A}^2}$). A similar calculation can be done for the STEM mode to find the critical time for various magnifications since the intensity is fixed for a specific spot size. The electron intensity for a 0.2 nm spot size with a 40 µm condenser aperture

[3]Same value, but with different units, using number of electrons per angstrom squared.

is then measured to be $1.61 * 10^5 \frac{C}{s\,cm^2}$. This intensity is then distributed in the pixel size determined by the magnification over a specific dwell time. This redistribution is assumed to be unity when the pixel area is equal to the spot area, otherwise a factor equal to the relation between the spot area and the pixel area is multiplied with the intensity values above. The resulting critical durations is listed in table 4.2 by using the critical doses for the TEM mode.

Besides observing the emergence of the nanopaticles, their composition and structure is also important to investigate. To study the composition, EDX is the ideal technique, and showing the spatial distribution is advantageous in this case as it shows the signals from the bulk, nanoparticles and amorphous layer simultaneously. Therefore, EDX-STEM is used to look for systematic deviations from the bulk structure, along with an SAED image that can be used to extract the nanoparticle structure.

In figure 4.7(a) shows an overview HAADF-STEM image of a region used for EDX-STEM. The image is taken from a type D $Pb_5Ge_3O_{11}$ specimen after the edge has been deliberately deformed. The electron beam was focused in TEM mode onto the edge, with a convergence slightly larger than the main nanoparticle in the image, which eventually lead to the deformation of the material including the largest particle with a diameter of about 82 nm encircled by smaller particles. Figure 4.7(b) and 4.7(c) is the spatial distribution of the same region for Pb and Ge, respectively. The most obvious characteristic is the distribution of Ge. The element is missing in the largest nanoparticle, and it can barely be seen to be richer in the encircling region. On the other hand, Pb is as prominent in the nanoparticle as in the bulk, while slightly weaker in the encircling region.

One possible conclusion from this is that under the exposure of high intensity electron beams, the material decomposes into a pure Pb particle with the remaining Ge in the surrounding amorphous material. This is partially consistent for both EDX maps, as the the concentration of Pb in the large particle would squeeze out the Ge leaving a Ge rich ring around it. This idea does is not consistent for the smaller particles however, as they does not produce strong Pb contrast in figure 4.7(b), and is not missing in figure 4.7(c). However, these particles are much smaller than the largest and their signal may just be too small in comparison. A larger scan time may resolve this, but EDX scanning requires a large dose which in turn can create more defects or change those that are already there.

Regarding the structure of the particles, the SAED figure (figure 4.7(d)) was taken from a region where the entire bulk material had been deformed into multiple defects. The resulting rings with many sharp spots is then an indication that the defects are crystalline with a randomized orientation. By measuring the distances between the rings, the distances relative to the first ring can be used to reveal the atomic structure. If the nanoparticles are in fact pure Pb structures, then they might also belong to the FCC structure found in Pb[22]. The structure factor for this system was worked out in equation 2.15, and the result is strong reflections whenever all hkl indices are odd or even. In table 4.1, the absolute value of $\mathbf{G}$ for each strong reflection is listed, relative to the $\mathbf{c}$-vector and relative to the [111] reflection. The measured values in figure 4.7(d) is

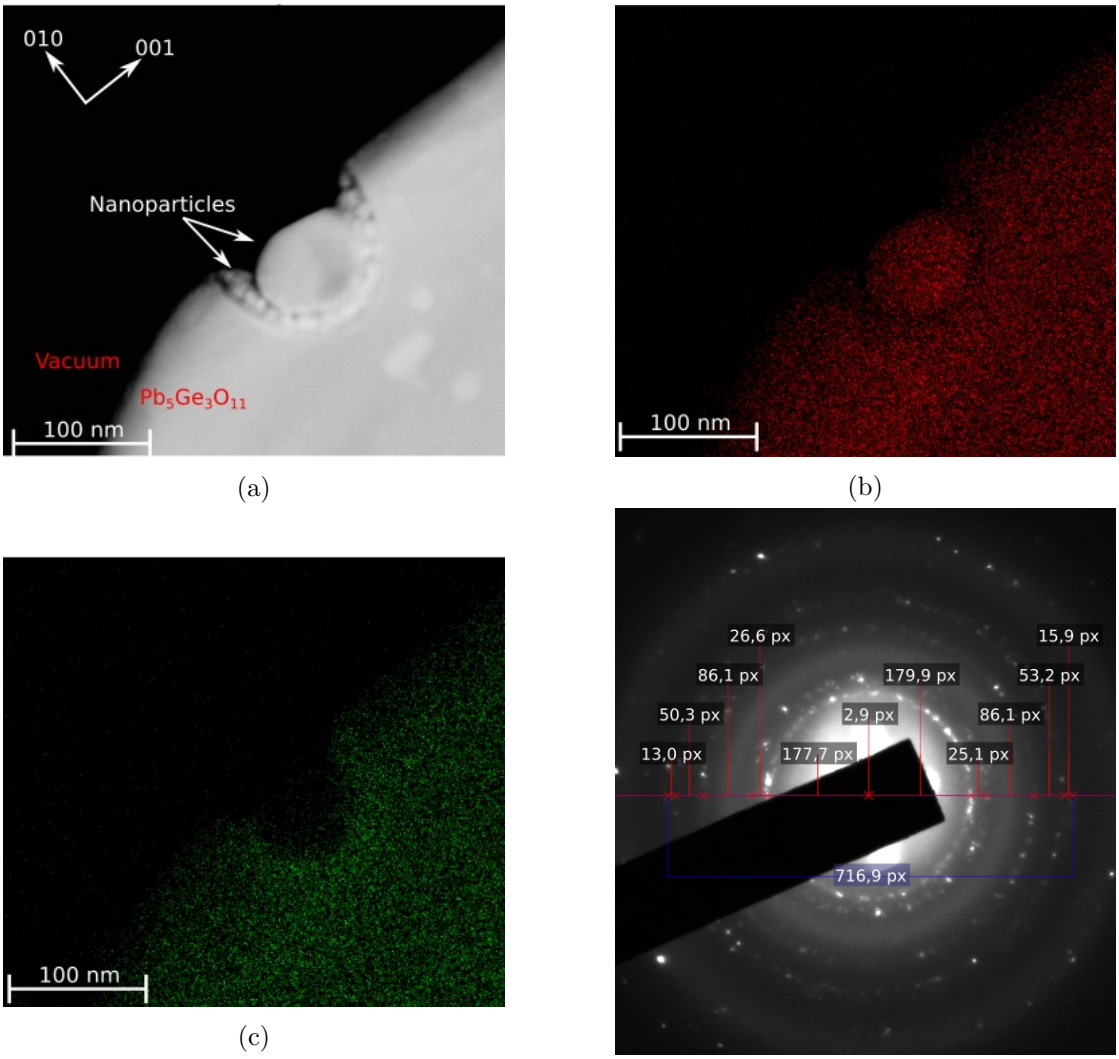

Figure 4.7: Images showing the composition and structure of the defect nanoparticles in a type D $Pb_5Ge_3O_{11}$ specimen. (a) is an HAADF-STEM image displaying a large particle defect surrounded by smaller particles. (b) and (c) shows EDX-STEM images of the same region, displaying the spatial distribution of Pb and Ge, respectively. (d) is an SAED image of a different region with more defects than bulk material. The diffraction pattern consists of rings similar to that of powder diffraction, and the distances between the rings is measured in pixels (arbitrary units). Images are taken with the 2100F microscope.

then listed below for comparison.

The first five reflections provides an accurate fit with the FCC structure, which is the common structure for pure Pb. Combined with the EDX data which also suggests a pure

Table 4.1: Table of the spacings in the FCC reciprocal lattice, measured in terms of the lattice parameter and relative to the closest [111] reflection. Measured values found in figure 4.7(d) is listed below for comparison.

Reflection	111	200	220	311	222
Length (relative to **c**)	$\sqrt{3}$	2	$\sqrt{8}$	$\sqrt{11}$	$\sqrt{12}$
Length (relative to 111)	1	1.15	1.63	1.91	2
Measured length (relative to 111)	1	1.14	1.62	1.91	1.99

Pb composition, the defects can then be safely assumed to be a pure Pb FCC structure. The Ge and O must then be expelled from the defect region, which the EDX data also supports by showing a richer Ge ring around the main defect, although contrast is weak. The exact composition, i.e. whether O is part of the compound, can not be determined by EDX as the low Z sensitivity of EDX is too poor. However, the SAED pattern does not show strong reflections besides the FCC rings so the remaining compound is most likely amorphous.

Deforming crystalline material into amorphous is a common problem for insulators in a TEM, and especially when working in STEM as all the intensity of the electron beam is converged onto a very small region[56]. For $Pb_5Ge_3O_{11}$ it became a problem as it put a heavy restriction on the amount of high-resolution imaging that could be done. To quantify the problem, two SmartAlign image stacks (figure 4.8) were taken of a type D specimen; one low magnification HAADF-STEM stack of the edge of the specimen showing growth of an amorphous layer, and one high-magnification HAADF-STEM stack displaying a fading lattice contrast. Figure 4.8(a) shows the edge of the specimen with no or little amorphous layer. After taking 20 images with 5 µs exposure each (100 µs in total) with a pixel size of 0.19 nm, the result is figure 4.8(b). The edge has gained a 25.2 nm thick layer of amorphous material, and the features in the top of the specimen shows a reduced contrast. In figures 4.8(c) and 4.8(d), the same effect is seen at a higher magnification with a total exposure time of only 20 µs. Nanoparticle defects is however seen in the initial image which means the surface was exposed to the electron beam prior to the image capture.

Using the value for the intensity in STEM mode measured above, the total exposure after 100 µs pixel dwell time in figure 4.8(b) amounts to $14.0\frac{C}{cm^2}$. This means that the amorphization dose per nanometer is $0.64\frac{C}{cm^2}$ $(3.99 * 10^2 \frac{e}{\mathring{A}^2})$. An alternative measure of amorphization is shown in figures 4.8(c) and 4.8(d), where the lattice contrast can be seen to drop sharply over a 20 µs pixel dwell time in high-magnification HAADF-STEM. The pixel size is 0.059 nm at this magnification, which implies a dose delivered between the two figures of $29.1\frac{C}{cm^2}$.

To quantify the contrast, the profiles perpendicular to the most prominent lattice planes is shown in top right of each figure, and the difference between the peaks and midpoints relative to the mean value (see equation 2.53) is used to measure the contrast. In the initial figure 4.8(c), the contrast averaged over the first five peaks is then measured to 0.892, while in figure 4.8(d) the contrast has been reduced to 0.085. In STEM imaging,

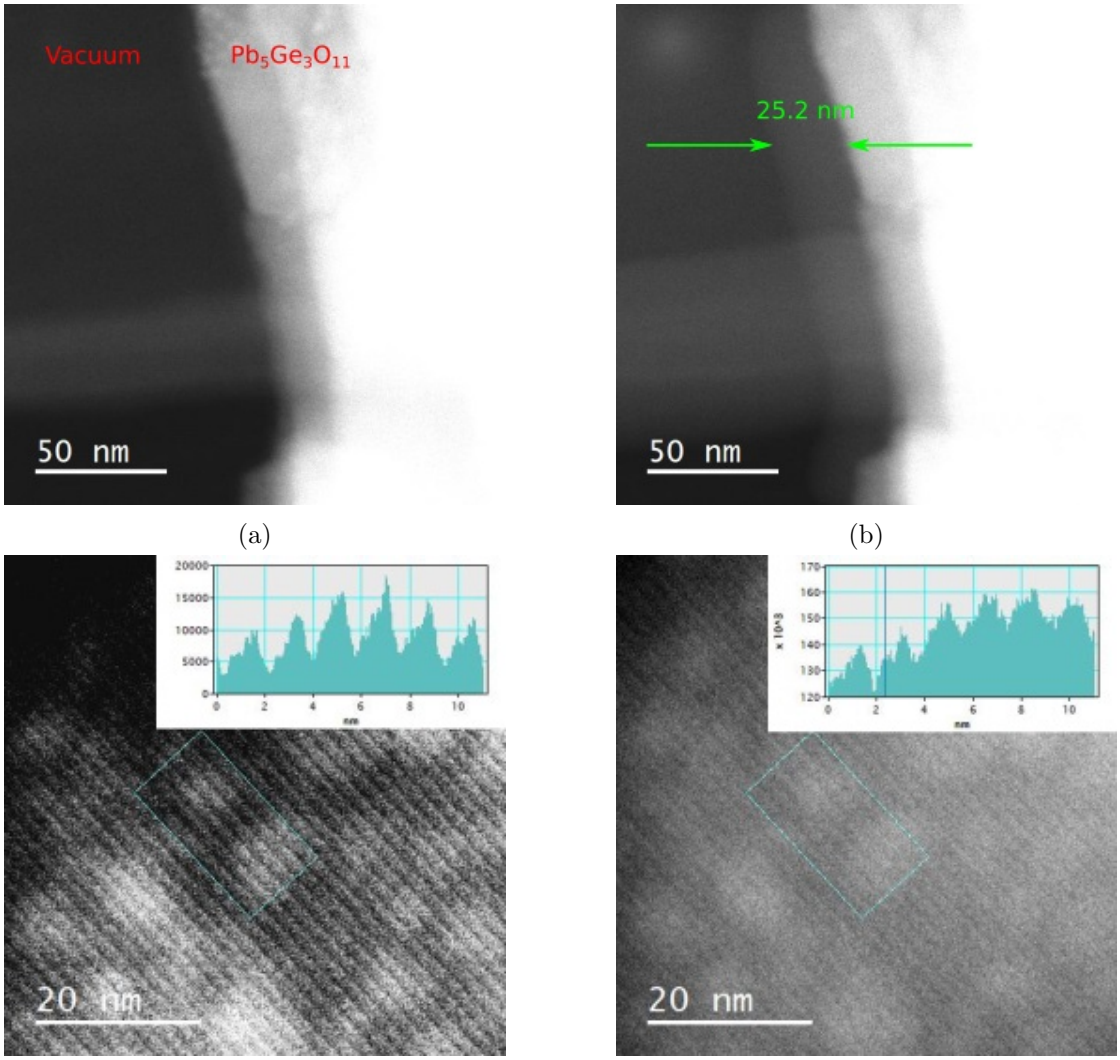

Figure 4.8: HAADF-STEM images of a type D $Pb_5Ge_3O_{11}$ specimen showing rapid growth of amorphous layers. (a) and (b) shows the edge of the specimen accumulating a 25.2 nm amorphous layer from the initial state and after 100 µs exposure per 0.19 nm square pixel, respectively. These images are taken close to the [100] zone axis. (c) and (d) shows a different region in high-resolution displaying the contrast fading at the [111] zone axis. (c) is the initial state, and (d) is the same region after 20 µs exposure per 0.059 nm pixel.

the contrast from the crystal structure has been reported to reduce the contrast almost linearly with the percentage of amorphous material present[57], $C = C_{ideal}\,R$, where R is the percentage of amorphous material and C_{ideal} is the ideal contrast from a specimen without any amorphous material. If the initial figure was taken before a significant

amount of amorphous material was formed, then the contrast can be assumed to be ideal for this thickness, and the reduction to 0.085 implies a transformation to 90.4% amorphous. With the dose given above between the images given above at $29.1\frac{C}{cm^2}$ and an amorphization dose per nanometer of $0.64\frac{C}{cm^2}$, a total of 45 nm should become amorphous, which agrees with the composition of 90.4% amorphous if the specimen was initially 50 nm thick. Although the thickness was not measured, high-resolution STEM would not be possible for much thicker specimens with less contrast from the lattice. However, using an electron energy loss spectroscopy (EELS) detector (not installed on this microscope) to measure thickness could be tried to explore the thickness dependency of the beam damage. Similar to the critical dose needed to form nanoparticles, a critical dose can be defined in this scenario as well as the dose delivered between figures 4.8(c) and 4.8(d). Table 4.2 then lists the critical pixel dwell time at different magnifications to serve as an upper limit on the exposure time when taking STEM images.

Table 4.2: Table with values for T_{d_1} and T_{d_2} for pixel dwell time calculated for the STEM mode at different magnifications, using spot size 0.2 nm. The final row also displays the pixel dwell time before losing 90.4% of the contrast due to amorphous layers for a 50 nm thick specimen.

Magnification	800K	2M	5M	8M	11M	14M
T_{d_1} (ms)	41.31	6.61	1.03	0.41	0.22	0.14
T_{d_2} (ms)	137.94	22.07	3.44	1.38	0.73	0.45
T_a (μs)	207.7	33.23	5.18	2.08	1.10	0.68

All the beam induced alteration of the material described above should be avoided and the critical dose need to be considered when designing experiments on $Pb_5Ge_3O_{11}$. The charging effects can put a limit to conventional TEM techniques such as DF and BF as the beams were deflected unevenly from the specimen, converting point reflections into disks at the BFP making it challenging to select them with the objective aperture. However, the most challenging techniques are those with a more converged beam such as CBED and HRTEM. Smaller specimens should be used, for instance the type D specimens were far easier to work with as they produced a much smaller electrostatic deflection field. This could be due to the carbon grid which allowed them to discharge, or that the material could only sustain a certain amount of charge before decomposing. A small specimen would then build up a certain deflection field and then proceed to decompose instead of building a stronger field. For the tripod specimens the charge deposited onto a local region could still diffuse into the remaining specimen which in turn contributed to a larger deflection field. If this effect was true then the tripod specimens should also be less prone to decomposing, but this has not been tested. To reduce the deflection field, silver paint can be used to connect the tripod specimen to the conductive TEM grid, but the effect is much smaller than switching to a microparticle specimen.

Emerging nanoparticles was a problem when operating in TEM mode, and also here focusing the beam amplified the problem. Two critical doses were found for the

emergence of a few small nanoparticles and the point were the nanoparticles density beam comparable to bulk material, and was measured to be $5.78 * 10^3 \frac{C}{cm^2}$ ($3.61 * 10^6 \frac{e}{\mathring{A}^2}$) and $1.93 * 10^4 \frac{C}{cm^2}$ ($1.20 * 10^7 \frac{e}{\mathring{A}^2}$). The particle were found to be pure Pb with an FCC structure based on STEM-EDX and SAED, but the effect on the ferroelectricity remains unknown. When working with $Pb_5Ge_3O_{11}$ in a TEM, rapid amorphization occurred in STEM mode. A critical dose was found of $0.64 \frac{C}{cm^2}$ ($3.99 * 10^2 \frac{e}{\mathring{A}^2}$) per nanometer (the dose needed to amorphize 1 nm of material). With few options to reduce the intensity in STEM mode (mainly spot size and pixel dwell time), this forms a significant challenge for high-resolution STEM imaging. This type of amorphization was however not observed in TEM mode, while the nanoparticles did not emerge as often in STEM mode as in TEM mode, implying that the dose rate (not just total dose) and beam diameter are important parameters for these types of beam damage that could be explored further.

4.3 Correlated SEM/TEM Routine with Tripod Polishing

4.3.1 Overview Domain Structure Imaging by SEM

To gain overview information on the domain structure, the SEM is an efficient and verstatile tool. In standard viewing mode, the domain are visible in $ErMnO_3$ as demonstrated with a type A specimen in figure 4.9 and type C spceimen in figure 4.10. In the case of the type A specimen, the polarization direciton is lying in the plane of the specimen and the domain walls are clearly visible at acquisition times below one minute. In the close-up figure the domain wall will however appear to be several hundred nanometers wide, although they are in fact between 1-2 nm wide, indicating the resolution or the generated contrast in the SEM is not sufficient to study the actual profile of the domain wall. Surface contrast can also be seen in the form of small circular particles and stripes most likely colloidal silica and scratches from the tripod polishing, but the strong domain wall contrast is unaffected by this. It is also worth noting that the domain wall contrast is not consistent, with some domain walls dissapearing before entering a vortex. In addition, a few of the domain walls are less sharply defined with weaker contrast than the others, as the center domain wall in figure 4.9(b). Since the SE yield is inversely proportional to conductivity, these domain walls are likely to be the positively charged tail-to-tail walls[33] while the brightest walls the negatively charged tail-to-tail walls, although this requires additional confirmation.

To study the domain structure, the ideal acceleration voltage was found to be 1.5 keV, but the APREO microscope had no user-accessible option between 1 and 2 keV, so the latter was chosen with this microscope. At this voltage the type C specimen was studied after polishing the first side, where the polarization is pointing out of the plane of the specimen. In this case the domains and not domain walls showed a contrast difference owing to the pyreoelectric effect[17]. It is worth noting that the contrast is far weaker than in the case of type A and B specimens, so having a finely polished surface is more important to reduce unwanted contrast, and acquisition times above 3 minutes was necessary. It should also be noted that a few type A and B specimens did not show

either domain or domain wall contrast under any circumstances, and after ion milling the domain and domain wall contrast was in general reduced.

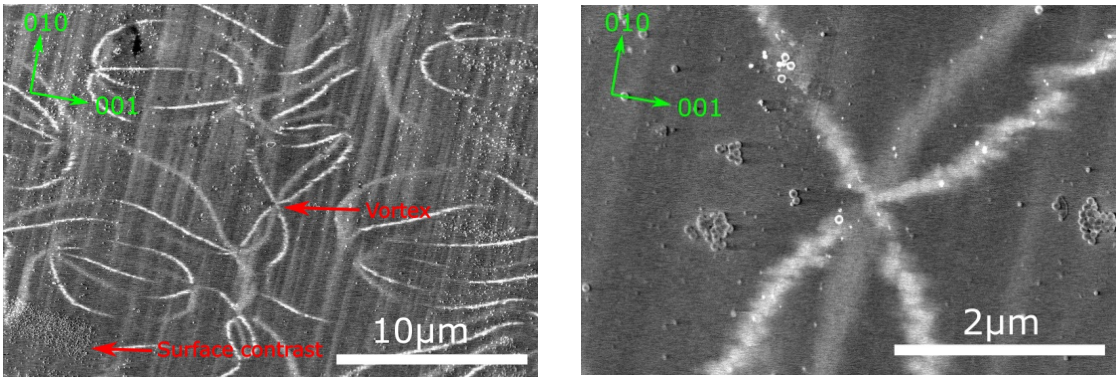

(a) (b)

Figure 4.9: SEM images of the domain structures in a type A $ErMnO_3$ with the polarization in the plane of the specimen. Figure (a) shows an overview of multiple vortices and some surface contrast while figure (b) shows a close-up of one vortex. Images are taken with the S-5500 microscope at 15 µA emission current and 1.5 keV acceleration voltage.

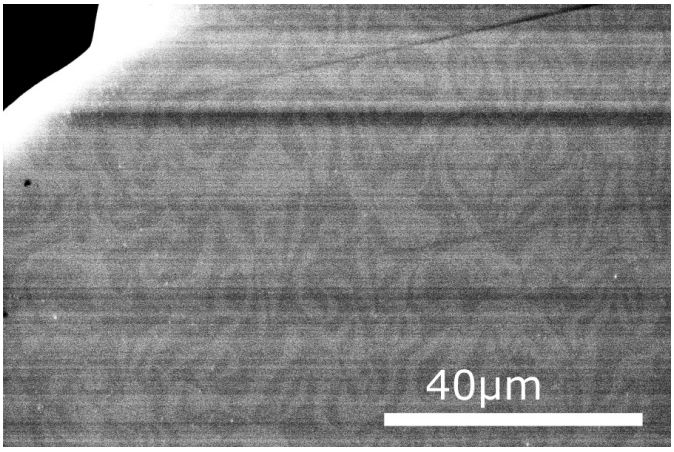

Figure 4.10: SEM image of the domain structures of $ErMnO_3$ with the polarization pointing out of the plane of the specimen (along the **c**-axis. Image is taken at 50 pA emission current and 2 keV acceleration voltage with the APREO microscope using the ETD.

The figures shown above (figures 4.9 and 4.10) illustrate how the SEM can be used to gain overview information on the domain structure regarding shape and size of the domains, and even show signs of being able to distinguish positively and negatively charged domain walls. The SEM is however unable to properly probe the profile of the

wall with nanometer resolution and obtain confirmation on the polarization direction so the results must be connected to experiments performed by the TEM. Since the TEM requires thin specimens, only the edge of the tripod specimen can be used, and figures 4.11(a) and 4.11(b) shows two SEM images of an electron transparent edge in a type A specimen. In the top of the figures where the specimen is thicker weak contrast from the domain walls are present, but the contrast fades away as they get closer to the edge. At the very tip of the specimen there is also a line present where the contrast disappears completely, which is called the transparency line in figure 4.11(a). In figure 4.11(b), this line is measured to be around 6.51 µm from the edge where the TEM can be used. Furthermore, the surface contrast at both sides of the image show that the loss in domain wall contrast is not associated with a general resolution or contrast loss (for instance from charging effects). Assuming the edge is 200 nm thick (most likely smaller), the critical thickness for observing domain contrast in $ErMnO_3$ is then found to be 427 nm. This is far above what the TEM can work with, and as a result the SEM and TEM can not probe the same locations in the specimen without taking a more systematic approach.

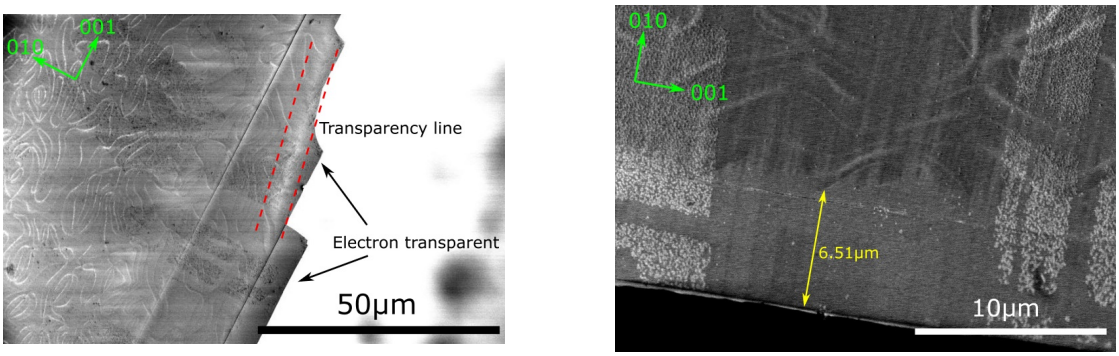

(a) (b)

Figure 4.11: (a) SEM overview image of the edge of a type A $ErMnO_3$ specimen. As the specimen becomes thinner the contrast from the domain walls fades away, and at the electron transparent region the contrast it is completely gone. Between the two stripled red lines there is a line indicating where the contrast disappears. (b) close-up of the edge showing the line where the domain walls dissapear, but also finely resolved surface constrast on both sides of the image. (a) is taken with the APREO microscope using T2 detector in immersion mode at 1 keV and 0.4 nA, and (b) is taken with the S-5500 microscope at 1.5 keV and 15 µA.

In order to make use of easily obtained domain structure images from the SEM, the specimen preparation routine was slightly altered to allow domain walls to be found at the edge. The routine in appendix A is still used, but when polishing the second side the specimen was not mounted near the edge of the pyrex, but instead in the middle so there is at least 500 µm between the edge of the specimen and the edge of the pyrex. When polishing with an angle of 2°, the height of the specimen could then be determined

by measuring the distance L between the specimen edge and the polished pyrex (see figure 4.12). To achieve a thickness larger than the critical thickness of 427 nm, the length L must be at least 12.23 µm, but larger value between 50 and 100 µm was more convenient to use as the specimen edge was not perfectly straight and some regions might become thinner than others. After polishing the second side the TEM grid was then glued onto the specimen, and SEM could be used to gain information at the edge of the specimen on the side that was polished last. The other side would then be ion milled to electron transparency, so the same regions could be viewed in the TEM. Note that the ion milling must be done on the side opposite to the one which was imaged, otherwise due the curvature of the domain wall their position in the final specimen would be different then in the pre-milling image.

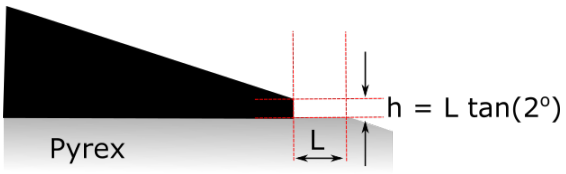

Figure 4.12: Schematic of a modified tripod polishing routine for correlated SEM and TEM studies. The specimen is glued at the center and not the edge of the pyrex, and polished only to the point where the height is at or above the critical thickness for observing domain walls in the SEM.

Figure 4.13 shows a region where both SEM and TEM has been carried out, by using Ar ion milling (described in section 3.2) between the two images. In figure 4.13(a) the region is shown directly after the modified tripod polishing routine where it is still thick enough to be imaged by the SEM, although the contrast is weaker than in the bulk. The domain walls are indicated by red arrows, and can be found closer than 2 µm away from the edge (2 µm into the specimen equals 70 nm thickness increase). A vortex is also seen directly behind the sharp tip, about 4.5 µm into the specimen. The same region is shown after ion milling in an overview image from the TEM in figure 4.13(b), where the sharp tip in the SEM image has been slightly etched off. In addition, there are no signs of the domain structure anywhere in the region which means specific TEM techniques for visualizing ferroelectric domains are needed for overview information on domain structures in the TEM.

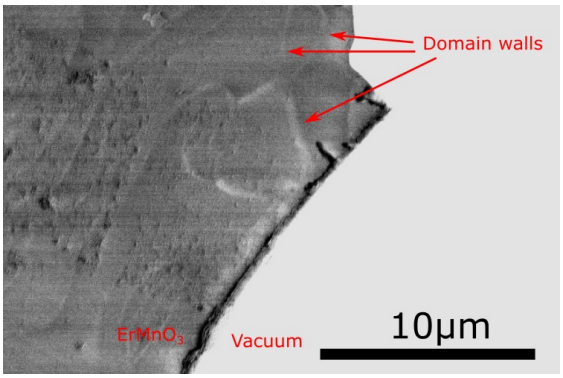

(a)

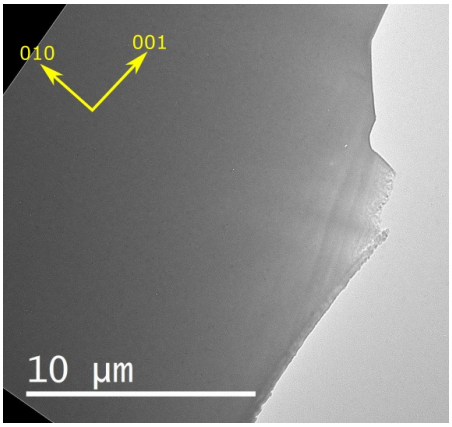

(b)

Figure 4.13: A selected region imaged by both TEM and SEM, with ion milling between the two sessions. (a) shows a SEM image of the region while it still thick and domain walls are visible and indicated near the edge. (b) shows a TEM overview image after ion milling, where the sharp tip in the SEM image has been slightly etched off. SEM image is taken with the APREO microscope at 1 keV and 0.4 nA in immersion mode using the T2 detector, and the TEM image is taken with the 2100F microscope and filtered in DM with a sharpening filter.

4.3.2 Overview Domain Structure Imaging by TEM

In figure 4.13, a specific region was shown in the SEM (figure 4.13(a)) to contain domain walls which were completely missing the corresponding TEM image (figure 4.13(b)). As the resolution of the TEM is needed, a technique to gain overview information on the domain structure may be needed and so a common solution is DF imaging[19][58][59][27]. As explained in section 2.2.5, two domain separated by a 180° rotation does not produce the same diffraction pattern due to the violation of Friedel's law as a result of dynamic (multiple) scattering. Not all reflection will give a strong contrast difference though, and selecting reflections far away from the center will contain less intensity to form images. The closest and strongest reflections that are opposite for two domains is therefore the best choice to begin with, and in $ErMnO_3$ along the [100] direction, this is the 002, 004 and 006 reflections. Due to the repeating pattern of two weak and one strong reflection (section 2.5), the other strong reflections are found at the 03X and $0\bar{3}X$ (X = ± 1, 2, 3 ...) reflections.

Simulations for the 002, 004 and 006 reflections, including their opposite, is plotted in figure 4.14. The 002 reflection is the strongest, as expected, but the difference between opposite domains is also continuous up until 150 nm. The largest peak at 20 nm should display 19% contrast, while the second peak at 40 nm should display a 7% contrast.

The 004 reflection on the other hand switches[4] with the opposite $00\bar{4}$ between being strongest four times before 0 and 100 nm thickness, although it can be used at 50 ± 10 nm thickness where the 002 and $00\bar{2}$ reflection switch. For very thin materials (< 50 nm), the 006 reflection is best suited, as it clearly shows the strongest contrast (28% at first peak and 20% at second peak) and also contains enough intensity. After 50 nm the contrast will however flip sign frequently and is not usable.

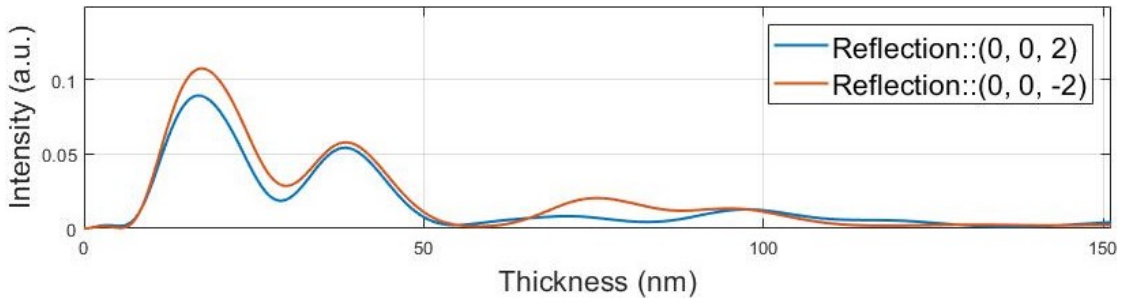

(a)

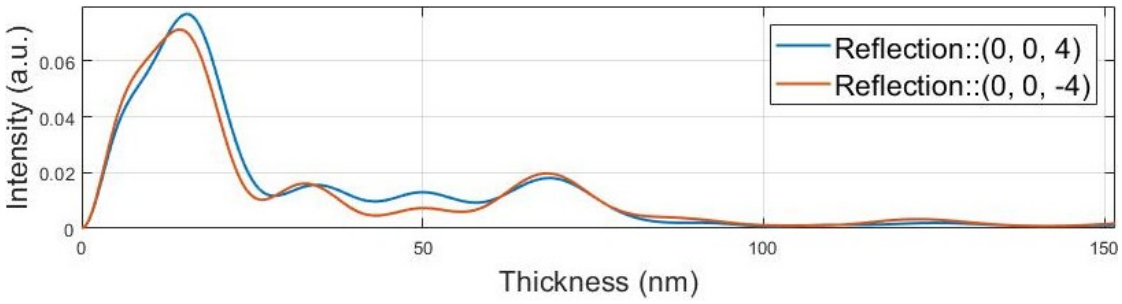

(b)

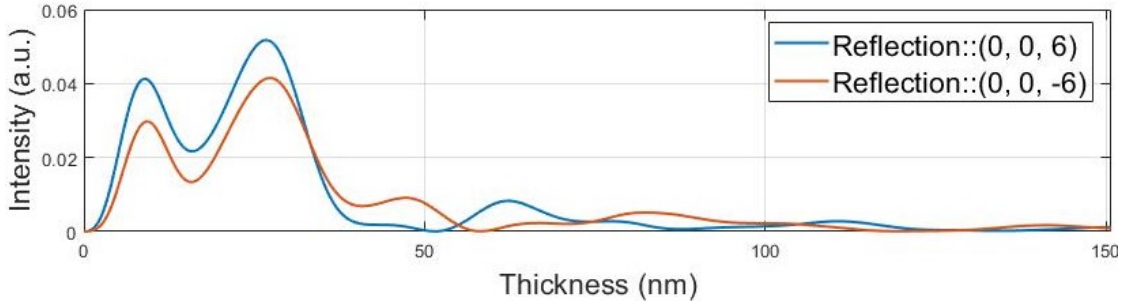

(c)

Figure 4.14: Simulation of the diffracted intensity of the (a) 002, (b) 004 and (c) 006 reflections plotted together with the opposite reflections $00\bar{2}$, $00\bar{4}$ and $00\bar{6}$ obtained at the same location in reciprocal space for opposite domains. Simulation is based on two-beam

The 002 and 004 reflections is therefore selected to investigate the region in figure

[4]Switching implies that the two reflection switches between being stronger and weaker, resulting in a contrast switch in the DF image.

4.13, along with their opposite reflection to make sure the contrast is inverted. The result is shown in figure 4.15, where the region where a domain wall was found with the SEM is encircled by the red square. However, neither of the four reflections in DF yielded any contrast of the domain wall. A few regions can be seen invert contrast, but a domain wall should be sharp and straight inside the red square. It can also be noted that the edge of the tip is far brighter than the domain wall region for all the reflections, meaning it is a far thinner region. One possibility is therefore that the domain wall region is still to thick (larger than 150 nm), but further ion milling will remove the recognizable tip and the mapping from the SEM is no longer usable.

By looking at the DF series in figure 4.15, one clear problem is the amount of noise and unwanted contrast not related to domain structure. The two main contrast mechanisms in DF are mass-thickness contrast and most importantly diffraction contrast. In a wedge shape specimen, the mass-thickness contrast should be fairly easy to interpret as the thickness increases linearly from the edge into the bulk. Scratches could also produce contrast, but they will always be perpendicular to the edge and parallel to each other. The remaining noise then originates in diffraction contrast from defects, which are especially pronounced in DF imaging as the other contrast mechanisms are removed or reduced.

In figure 4.16 two DF images using the 002 reflection is shown of two different specimen types in regions representative for te whole specimen. Figure 4.16(a) shows a type A tripod specimen with a drawn in domain wall found with the SEM, and figure 4.16(b) shows a type D powder specimen. In the powder specimen, the DF image is perfectly clean with the only contrast stemming from thickness fringes and the carbon film. On the other hand, the tripod specimen resembles that of the region 4.15, with slightly less thickness contrast, but still with no signs of the domain wall. Since these two specimens were made from the same starting sample, the tripod and ion milling preparation technique is therefore the cause of the defects. Although the tripod preparation may introduce a minimum of amorphous layering and a more uniform crystal structure[43], it is also reported to introduce surface roughness, dislocations and strain[60][61]. Ideally, the the powder specimens should therefore be used, but the small size with less than 1 µm electronic transparent material makes it challenging to gain overview information on domain structures, which in turn makes it challenging to separate domain walls from other interfaces.

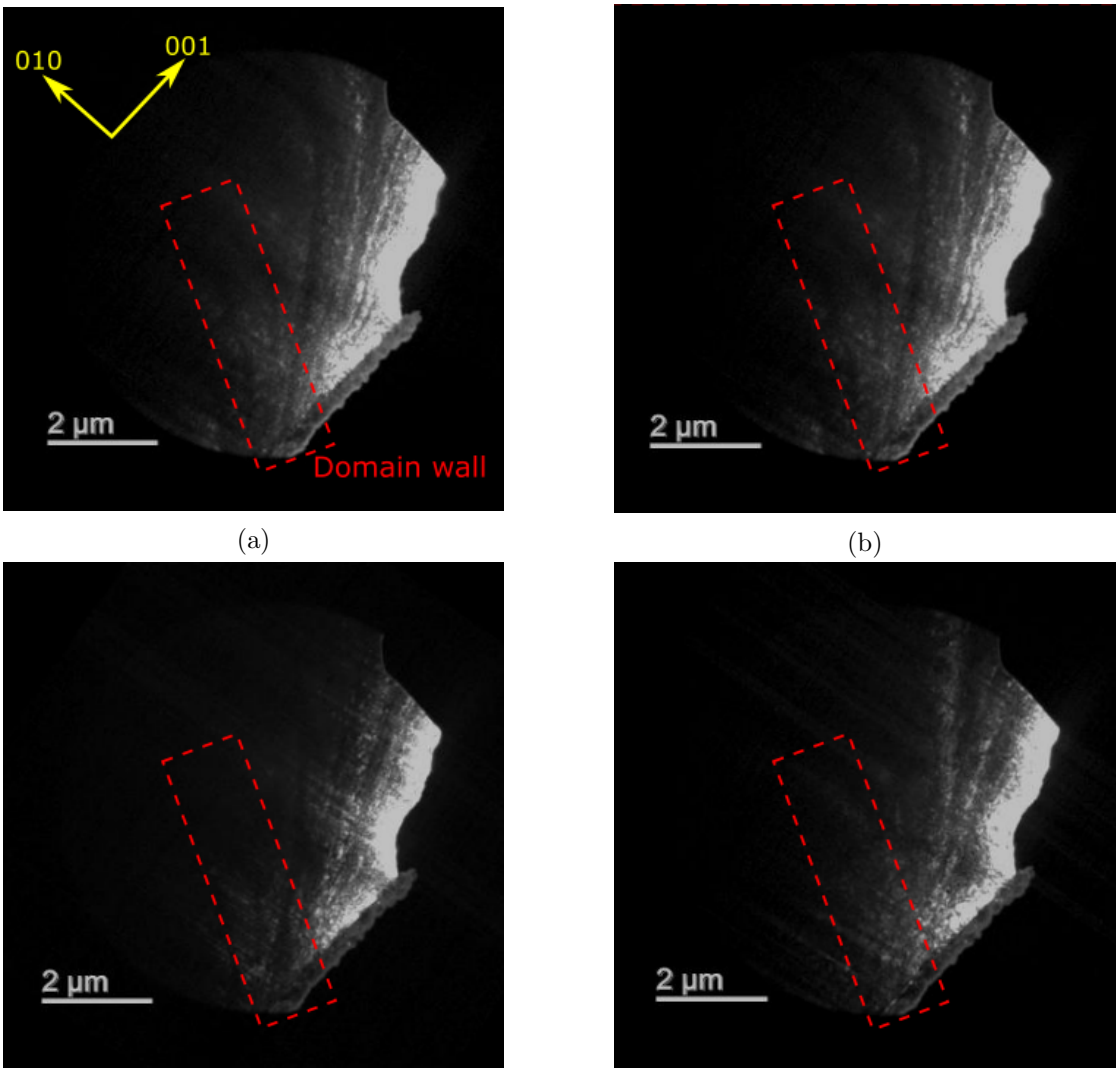

Figure 4.15: DF images of the region in figure 4.13 using the (a) 002, (b) 00-2, (c) 004 and (d) 00-4 reflections. The region where the domain wall should be located is encircled by the red square. Images are taken with the 2100F microscope.

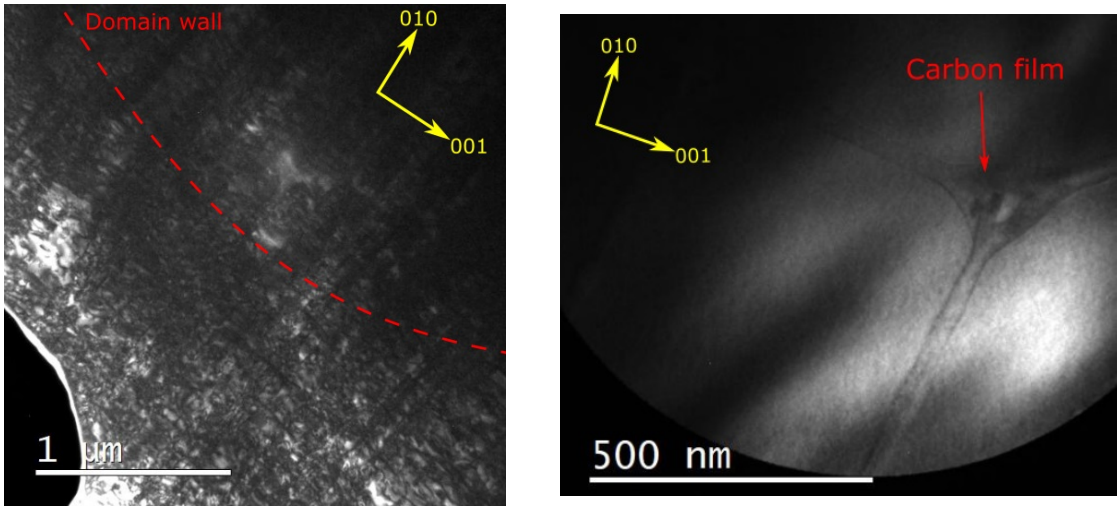

(a) (b)

Figure 4.16: Two representative DF images using the 002 reflection from two different specimen types. (a) a type A tripod specimen in DF with a lot of defects creating noise in the DF image, while (b) a DF image of a type D powder specimen with little to no defects and noise, but the underlying support. (a) also has a domain wall drawn in where it is found from the SEM mapping. Both images are taken with the 2100F microscope.

4.3.3 High Resolution Imaging of Domain Structures

The key advantage of the TEM compared to other techniques is the superior resolution. Since the polarization in $ErMnO_3$ is found from the crystal structure by its easily recognizable pattern of Er atoms (↑↑↓, ↓↓↑), HAADF-STEM was performed on a tripod and powder specimen in an attempt to view the atomic structure. The Z-contrast from this technique is especially well suited for this purpose since it is only the heavy Er atoms that needs to be imaged, although they are tightly bound with an interatomic distance of 2.04 Å along the pattern.

Figure 4.17 shows two HAADF-STEM images of two different specimens, a type A tripod specimen (figure 4.17(a)) and a type D powder specimen (figure 4.17(b)). The ↑↑↓ pattern of the Er atoms is barely visible in the powder specimen, where it is drawn in as an overlay in the top of the figure. The interatomic distances are also measured to be 5.80 Å along the **c**-axis, and 6.24 Å along the **b**-axis, compared to the expected values of 5.71 Å and 6.12 Å. Possible causes for the 0.1 Å underestimation are inaccuracy in the microscope alignment, or deviation in the STEM calibration. Since the actual **c**-axis direction is found, the polarization can also be determined and it is set to always be opposite to the **c**-axis in this work. The high resolution image is however only obtained in the thinnest region of a small powder specimen with no domain walls present.

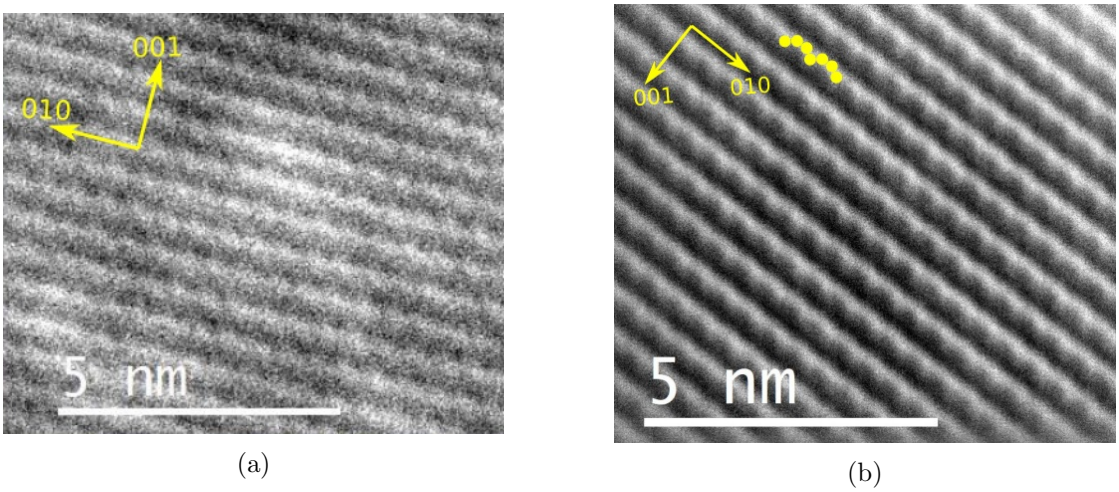

(a) (b)

Figure 4.17: Two high resolution HAADF-STEM images of $ErMnO_3$ imaged with almost the same dose, (a) in a type A tripod specimen and (b) in a type D powder specimen. In the latter, an ↑↑↓ pattern of the Er atoms is barely visible and an overlay in top of the figure is drawn in such that the actual **c**-axis direction was determined along with the polarization (with is pointing the opposite direction). In the tripod specimen the ↑↑↓ pattern is not found so the **c**-axis direction can also be the other way. Both images are taken with the 2100F microscope.

The tripod specimen on the contrary are larger containing several hundred domain walls, but also thicker with lower crystal quality and as a result the ↑↑↓ pattern can not

be determined in figure 4.17(a). The **c**-axis is still drawn in as with previous images, but as usual it may be flipped 180° depending on the polarization direction. Overall, both the DF and high resolution STEM images point to the conclusion that the specimen quality of the tripod specimens is the limiting factor in studying the ferroelectric domain structures, while in the higher quality powder specimens the size is the only problem (too small to recognize and track domain walls).

4.4 The Domain Structures of Lead Germanate

4.4.1 Overview Imaging by SEM

To begin the investigations into $Pb_5Ge_3O_{11}$, the SEM is employed to obtain overview information on the domain structure as shown in figure 4.18. A good contrast is achieved close to 5 kV acceleration voltage, although previous articles reports that 5 kV is the equilibrium value where the material remains uncharged and a value larger than 7 kV is needed[9]. Figures 4.18(a) and 4.18(b) shows an overview and close-up of the domains in a type A specimen. The domains can be found to be needles elongated along the **c**-axis with an in-plane polarization (figure 4.18(b)), and with an out-of-plane polarization the domain structure is instead irregular and shaped as a maze (figure 4.18(d)). This is consistent with the previously documented starting domain structure (SDS)[11], unlike the data from the S-5500 in figure 4.18(c) taken at a larger beam current (5 µA against 0.1 nA). This figure shows a maze pattern in a type A specimen with an in-plane polarization, which resembles more the free domain structure (FDS) than the SDS. There are however several features of the domain imaging that should be addressed.

Firstly, the imaging can be seen to be heavily affected by charging effects. Beginning with figure 4.18(a), the visible domains are located around the center of the image and appears as needles coming out of a dark region. However, the dark region does not have sharp edges on the opposite side and is therefore not a domain, and must instead be dark simply by emitting fewer electrons than the brighter regions surrounding it, as a consequence of charging effects. Besides the dark region in the center, the remaining parts of the image undergoes large contrast variation and no other domains are seen. As the crystal should be uniform, one possibility is that the contrast from the domains disappear behind the large charging effects. In addition, by comparing figures 4.18(a) and 4.9(b), the domain structure can be seen to change between the images. A square window is also visible in figure 4.18(b) where a previous image has been taken at higher magnification, and the border appears to block the needle domains in the bottom of the window. It is therefore important to be aware that the domain structure is easily rewritten during imaging.

This rewriting effect is most prominent when larger currents are used. Figure 4.18(c) is taken with the S-5500 microscope which uses a current several orders of magnitude larger than the APREO microscope (5 µA against 0.1 nA here). Since the domain structure is identical to the FDS, the domains are therefore reversed before the first image can be formed. A similar effect has also occured in the APREO images, as the

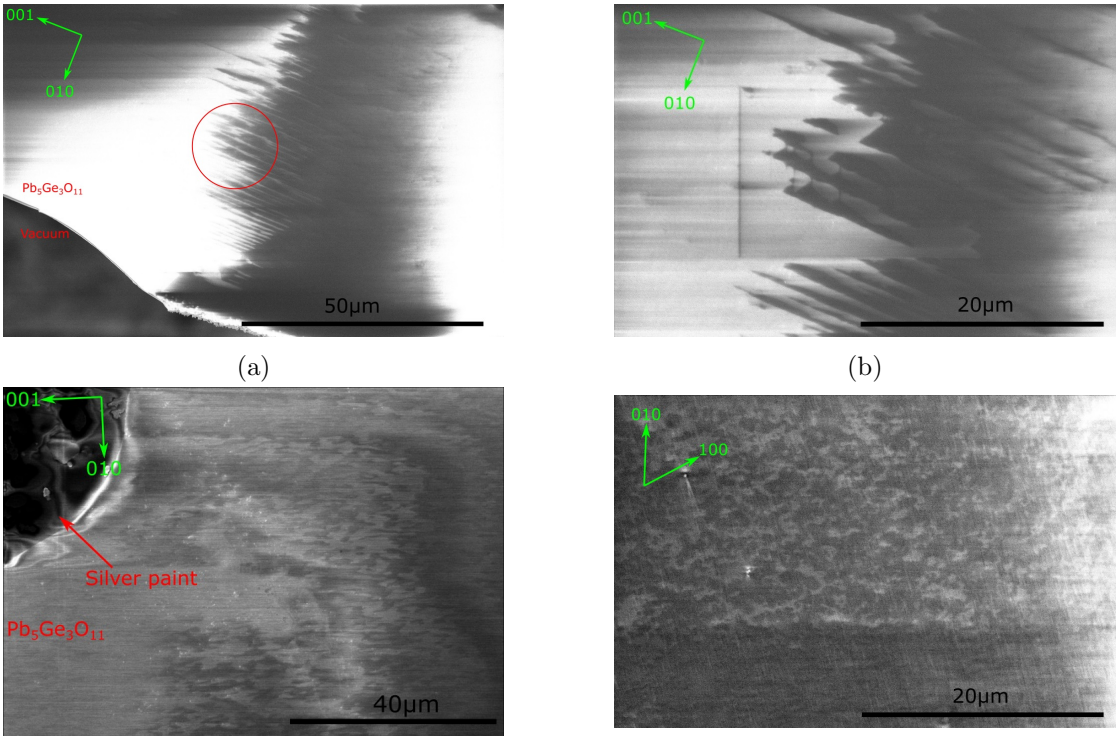

Figure 4.18: Four SEM images of the bulk of PGO specimen. (a) shows an overview of the domain structure in a type A specimen and (b) shows a close-up of the region in the red circle. (c) shows a different region in the same specimen as in figure (a), but taken with the S-5500 microscope. (d) shows a type C specimen. Images are taken at 5 keV and 0.1 nA with the APREO microscope in immersion mode using the T2 detector, and at 5 keV and 5 µA with the S-5500 microscope.

domains appear to have a thickness variation. In figure 4.18(a), it can be seen that the needles are smaller close to the edge compared to bulk. Since the thickness variation was introduced after the tripod polishing and consequently after the crystal growth, the effect must have happened as a result of the exposure to the SEM current. The image is however taken using a small current of 0.1 nA so the main shape of the domains remain the same (long needles). Regardless of the microscope settings used, rewriting the domains or creating artificial equilibrium states should be considered for all results on $Pb_5Ge_3O_{11}$ when the material is exposed to an electron beam.

To correlate the SEM results to the TEM as was done for $ErMnO_3$, an attempt at imaging the edge of the tripod specimen in figure 4.18(a) was done and the result is shown in figure 4.19. This is a finished TEM specimen with an electron transparent edge which is entirely prepared by tripod polishing. In contrast to $ErMnO_3$ where the edge appeared finely polished without surface artefacts (figure 4.11), $Pb_5Ge_3O_{11}$ displays a

rougher edge and surface. Parts of the surface is covered in debris, and most of the edge is damaged and are especially rough and thin compared to the undamaged surface. Domains are also present, but their contrast flip from bright to dark (top to middle) and disappear in the middle of the image. Although domains are not present in electron transparent regions in $ErMnO_3$ either, this comes in form of a gradual contrast fade. In $Pb_5Ge_3O_{11}$ on the other hand, the domains are not visible due to charging effects causing the edge to appear either overly bright or dark. This is a problem seen across all the thin edge, and the thicker edge on the right side of the specimen in the overview image in figure 4.19(a). Slightly before the thicker edge, there is also a FDS present despite the bulk showing the SDS. This is an indication that the charging effects at the edge is much larger than in the bulk, and can lead to domain reversal faster than in the bulk. Considering that the bulk domains are affected so easily by the electron beam, finding domains at the edge is unlikely and combined with the large charging effects degrading image quality, a similar correlated SEM/TEM experiment as was done for $ErMnO_3$ (figure 4.13) using the PIPS was not successfully obtained with this material.

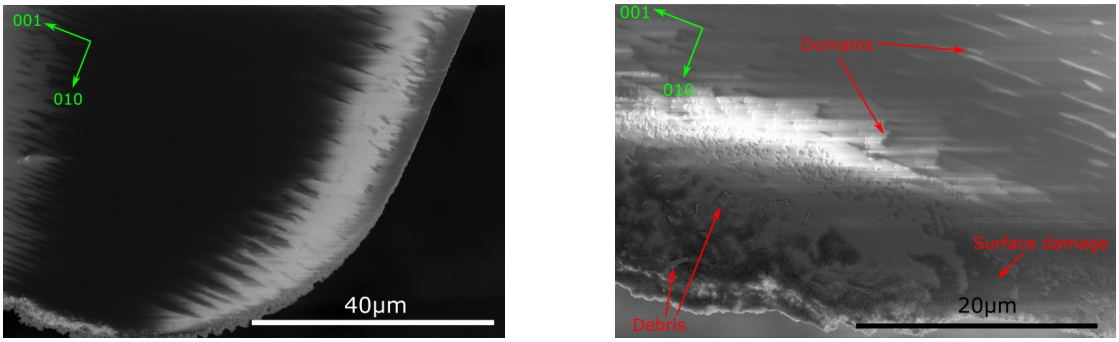

(a) (b)

Figure 4.19: Two SEM images of the edge of a type A PGO specimen. (a) shows an overview image of both both the thin edge (bottom) and the thick edge (right), both of which display different domain structures than the bulk. (b) shows a close-up of the thin edge where small domains are visible in the top and large amounts of surface contrast is seen in the bottom. Both images are taken with the APREO microscope in immersion mode using the T2 detector at 5 keV and 0.1 nA.

Despite charging effects and the damage surface, figure 4.19(b) can however show the general size and feature of the domain structure close to the edge. First of all, most the edge is mostly a mono-domain with the sharp needles which occupies only a small portion of the edge of about 200 nm width and up to 6-7 µm length. Secondly, the domain structure is not limited to needles, but a few domains with arbitrary shape similar to the FDS is also present which makes it a type of hybrid domain structure between the SDS and FDS. Correlating this with the TEM data will however be challenging as the domain structure studied here might be specific for the SEM and appear differently for the TEM due to different imaging conditions.

4.4.2 Overview Imaging by TEM

As for $ErMnO_3$, to gain overview information on the domain structures, DF imaging was used for $Pb_5Ge_3O_{11}$. The closest reflections to the center that are inverted when changing the polarization are the 001, 002 and 003 reflections. However, the structure factor resulting in the kinematic SAED in figure 2.27(a) will weaken the 001 and 002 reflections, so the most promising choice is the 003 reflection. Simulations for each of these are found in figure 4.20, and although the 002 reflection is strongest despite being unfavoured kinematically, the 003 reflections results in the largest contrast between opposite domains (55% at best). It is also consistent up to 120 nm thickness and is therefore chosen for the DF imaging.

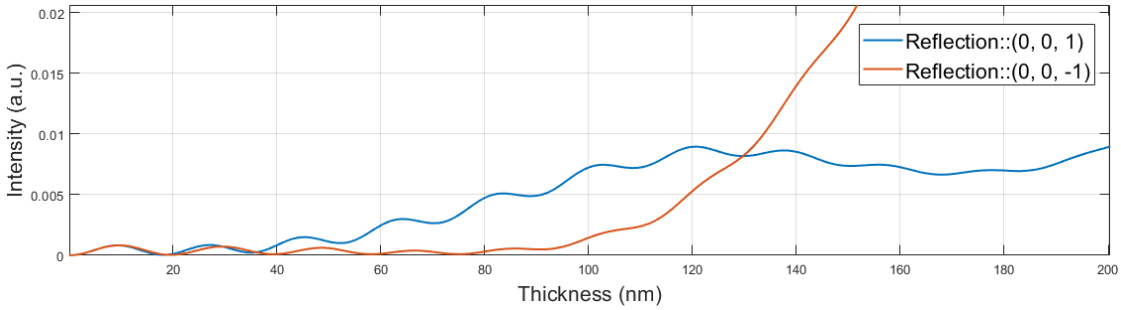

(a)

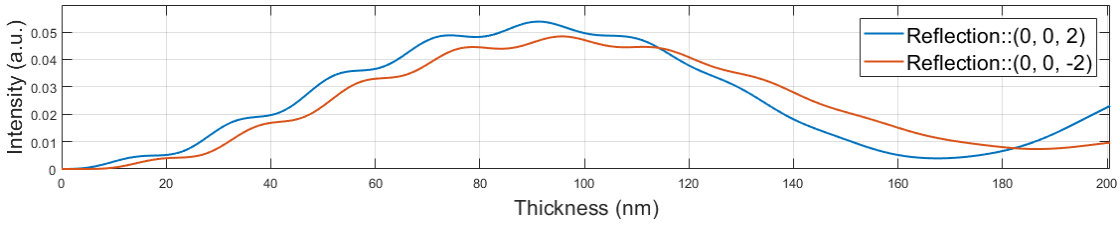

(b)

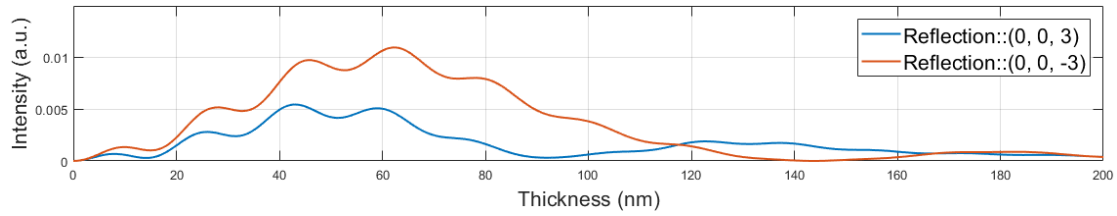

(c)

Figure 4.20: Simulations from the *JEMS* software of SAED along the [100] direction in $Pb_5Ge_3O_{11}$. (a), (b) and (c) is the intensity for the 001, 002 and 003 reflection plotted against their opposite reflection under a 180° rotation, similar to that of a domain wall.

In figure 4.21, two regions are shown in a type A $Pb_5Ge_3O_{11}$ specimen with TEM overview images as well as DF images with opposing reflections. First of, the TEM overview images display a range of contrast variation across the specimen. This is most

likely thickness and surface variations since the edge of the specimen could be seen to be heavily damaged from the tripod polisher in the SEM (figure 4.19). Although the damage is contained to the surface, the damage can come in the same form as the irregular ferroelectric domains making it challenging to identify domains in DF. Two regions where the surface contrast is sharply defined is therefore use for further investigations with DF. Keeping such an interface in the DF image allows for comparison between an actual domain interface (domain wall) and a surface interface (damage and undamaged), and make it possible to distinguish the two types.

In figures 4.21(a), 4.21(c) and 4.21(e) the same region is studied with an overview TEM image, a DF image using the 003 reflection and a DF image using the $00\bar{3}$ reflection, respectively. Several interfaces were found in figure 4.21(c) and indicated by arrows at the same location in both images, but only the arrow to the left was present in figure 4.21(e) which was the surface contrast. The middle arrow is the most probable to represent a domain, since the interface is sharply defined and in figure 4.21(e) it only seems to be a thickness fringe that is blocking the contrast. In the second region, figure 4.21(d) also point to several interfaces that could be domain walls, but also here the contrast on each side i not reversed when switching reflection in figure 4.21(f). Two regions labelled "I" and "II" is however reversed, although their interface is not sharp.

Due to the challenges in identifying the domains, additional techniques must be used to confirm that interfaces represent a domain wall. One way is the CBED technique, which can reveal the actual crystallographic direction and therefore also the polarization direction. At both sides of the interface a CBED pattern could therefore be taken to identify the polarization direction, and compared to see if it has been reversed. However, due to charging effects the beam can not be focused in conventional TEM mode without causing large beam deflection. Since CBED in conventional mode does not allow for simultaneous imaging the excact position of the CBED probe with beam deflection makes it too challenging to accurately probe the correct side of the interface without going far into the domain on each side. Since the technique is also very sensitive to small tilting (see C), the two probing positions can not be far away and as a result this procedure could not be performed here. STEM-CBED could resolve this issue by allowing simultaneous imaging and probing, but the apertures on the 2100F microscope was too large (even the 10 µm aperture) to form a CBED pattern without using the condensor mini lens (ALPHA knob) which normally is unavaible in STEM mode. Scanning CBED [30] where there is more control on the illumination to obtain optimal CBED patterns is a technique that should be considered in future work.

To overcome the charging effects and test the CBED routine, a type D powder specimen was tested in figure 4.22 combined with a DF image. Figure 4.22(b) shows the CBED pattern after indexing (compare to figure 2.27(b)), where the 003 and $00\bar{3}$ disks are used as they should be mirrored when the polarization is reversed. In the simulation with polarization along the **c**-axis the 003 is slightly weaker than the $00\bar{3}$ disk, and the same goes for the acquired CBED pattern. The actual crystallographic direction of the unit cell is thus revealed along the polarization (which is along the **c**-axis).

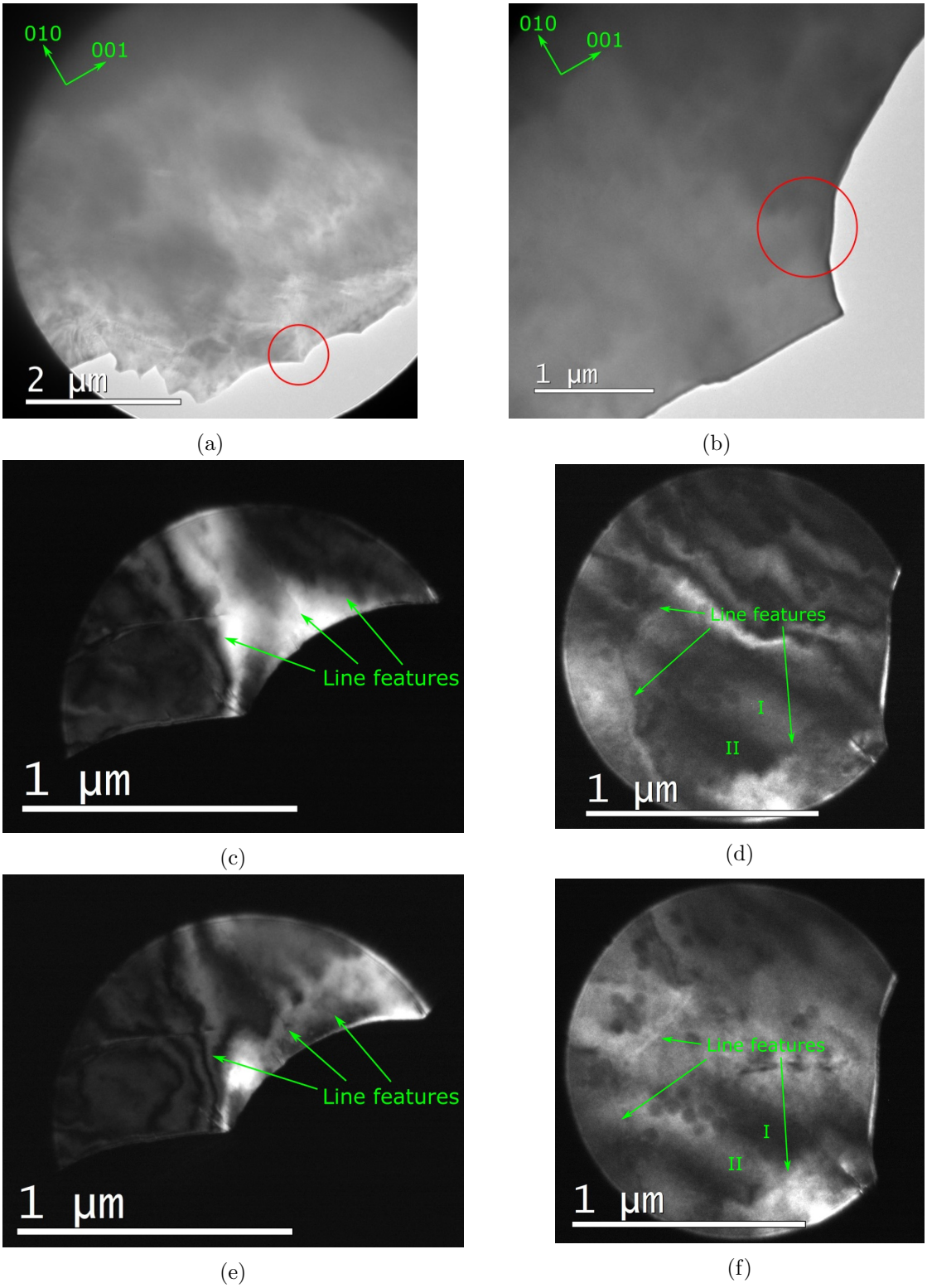

Figure 4.21: Dark field images from two different locations in the same type A tripod specimen of $Pb_5Ge_3O_{11}$. Figures (a) and (b) shows a TEM overview image of the two locations (red circle). (c) and (e) shows two DF images using the 003 and $00\bar{3}$ reflections, respectively, in the region in figure (a). (d) and (f) is also DF images using the 003 and $00\bar{3}$ reflections, but shows the region in figure (b). All images are taken with the 2100F microscope.

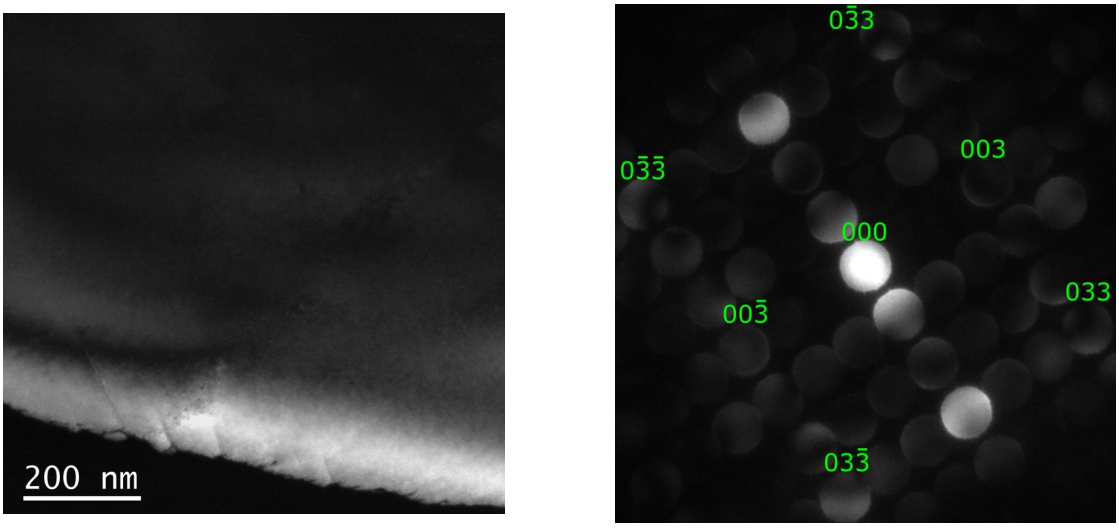

(a) (b)

Figure 4.22: (a) a DF image using the 003 reflection and (b) a CBED pattern taking in the same region. The DF image shows no features that could be a domain wall, but the CBED pattern reveals the polarization direction locally (along the **c**-axis).

The same region where the CBED pattern is found is imaged in figure 4.22(a), but there are no visible interfaces due to a combination of small particle size and surface roughness. The same surface roughness and small size also means that they can not easily be imaged by the SEM to get correlation with the TEM. Small size is however far easier to work with and does not display any noticeable beam deflection which is the main limitation with the tripod specimens.

The charged domain walls are the main feature of interest in the specimen, but other zone axis could be studied as well. Simulations on the 001 directions (appendix D) are very promising and can be used to investigate the interaction of the domains with the electron beam of a TEM. More specifically, the 001 zone axis has a "handedness" visible in the $\bar{1}30$ and $\bar{2}30$ reflections that results in a large kinematic intensity difference (figure D.1), in addition to the regular dynamical difference. These two reflections also switch place when the **c**-axis is rotated, allowing for DF imaging. The net result is a consistent contrast difference between domains up to 150 nm thickness, with a maximum of 100% contrast at 110 nm thickness which are ideal working conditions for typical tripod specimens. However, the challenges from charging in accurately identifying domains as with the 100 zone axis will also be a challenge here.

High resolution information on the domain structure is not yet obtained and can not be achieved in an efficient approach before finding a routine to identify domains. After they are identified, it must also be considered if the lattice image can be taken below the critical dose for damage (see section 4.2). Unlike $ErMnO_3$ where the easily recognizeable $\uparrow\downarrow\downarrow$ and $\uparrow\uparrow\downarrow$ of the Er atoms and the six-fold vortex immediately reveals the true nature of an interface in high-resolution or overview, $Pb_5Ge_3O_{11}$ does not have

such properties. Close examination of the unit cell can reveal that a row of Pb atoms are shifted 0.3 Å during polarization reversal. This is challenging to measure even for an abberation corrected TEM, although there are indirect ways of observing domain walls through strain[62].

As mentioned before, neither an overview of domains after deformation into the FDS, or directly looking at the unit cell display any noticeable pattern that could be used to distinguish domain walls from other interfaces. Finding a way to correlate the TEM results to another instrument is therefore highly important. Throughout this thesis, the SEM has been tried for this purpose, but the edge of tripod specimens could not be mapped in $Pb_5Ge_3O_{11}$ and the large specimen size caused too much charging for CBED to confirm the polarization. An alternative is then to image the bulk, and use the FIB to prepare small lamellas grounded to the grid with reduced charging effects for further TEM study. Although the SEM has been demonstrated to rewrite domains easily, the FDS also contains charged domain walls and high resolution information on any type of domain structure is a goal for this material. To obtain this final goal however, precise STEM must then be used with an abberation corrected microscope and with careful dose managment if at all possible[63].

In conclusion, no single specimen type was found to be able to correlate to SEM or gain overview information on domain structure and also be able to determine polarization locally. The CBED technique and DF using the 003 reflection is still recommended for further investigations on different specimen types, but ways to correlate TEM to another technique should be first priority.

Chapter 5

Conclusion

As stated in the introduction, the two main goals of this thesis were to i) test and document a combined, if possible correlated, SEM/TEM routine making use of the tripod polisher, which is not reported on these materials, to obtain large high quality TEM specimens for studying ferroelectric domains, and ii) find specific techniques and parameters that can be used to study the domains of $Pb_5Ge_3O_{11}$ along with gathering new information on the domain structure and the materials behaviour in electron microscopes. The main conclusions from the first main goal:

- For both specimens the tripod polishing routine worked for creating large (> 1 mm long) high quality electron transparent edges for the TEM. Ar ion milling at 3 keV and down to 0.1 keV was used for final thinning, and resulted in a thin ($<$ 5 nm wide) amorphous layer.

- A cleavage plane along (100) is identified in $ErMnO_3$ from the TEM specimen preparation and by diffraction, same as in $Pb_5Ge_3O_{11}$ and was used to make powder (microparticle) specimens for the TEM.

- Polishing with the cleavage plane parallel to the edge of the specimen would yield an edge with a staircase edge morphology resulting from cleaving, which was too thick for the TEM, but combined with Ar ion milling reduced the contamination and yielded a straight edge.

- Crushing the crystals into a powder dissolved in isopropanol, drop-casted onto a holey carbon copper mesh grid, produced in a fast and easy way, small particles of even higher quality. The usable particles were mostly wedge shaped facing down on the carbon grid with the cleavage planes. The higher quality allowed for the atomic structure of $ErMnO_3$ to be imaged with high-resolution STEM using SmartAlign acquisition and reconstruction which revealed the polarization direction.

- The domain structure contrast in SEM was lost below 427 nm thickness in $ErMnO_3$, which means no correlated SEM-TEM specimens could be made in one step. Instead, they were polished down to about 3 µm thickness by measuring the distance

from the specimen to the polishing line, and then mapped in the SEM before Ar ion milling down to electron transparency for TEM analysis.

- For $ErMnO_3$, the tripod polisher was found to introduce defects in the specimen which obstructed the DF TEM contrast of the domains.

The main conclusions for the second main goal:

- From the SEM it was found that the domains in $Pb_5Ge_3O_{11}$ are best imaged at 5 keV, unlike the 7 keV previously reported, and that domains are easily rewritten even with low currents (< 0.1 nA). Complete deformation into the free domain structure however requires a larger dose, but occurs immediately at a beam current 5 µA.

- Rewriting domains is dependent on thickness and geometry of the specimen. The thinner regions are rewritten far easier than the thicker, and the edges (both thin and thick) are often completely deformed in the first image.

- Due to severe charging effects being most dominantly present at the edge of the specimen, the SEM could not be used for mapping domains before TEM as in $ErMnO_3$, but it could still reveal that the typical needle or cigar shape of the domain up to 20 µm long in the bulk is no longer necessary at the edge. Instead they are much smaller, down to 1-2 µm, and some are deformed into the free domain structure structure. The SEM also revealed that the surface near the edge to be damaged and unevenly thick.

- Using dynamic electron diffraction simulations it was found that the 003 reflections are the best option along the [100] zone axis for visualizing ferroelectric domains. The contrast between opposing domains in DF imaging is consistent up to 120 nm thickness with the maximum contrast at 90 nm thickness favouring the $00\bar{3}$ reflection.

- DF TEM imaging using the 003 reflection showed that the tripod polishing did not induce defects in the $Pb_5Ge_3O_{11}$ specimens, and that DF imaging was possible. However, surface damage made it challenging to confirm line shaped features to be domain walls.

- CBED was attempted to confirm the change of polarization across the feature, but charging resulted in the beam being deflected in conventional TEM mode when converged, and CBED in STEM mode was suboptimal due to too large apertures resulting in disk overlap.

- Crushed specimen on C-foil displayed significantly reduced charging due to the small size and nearby carbon film, and CBED was demonstrated to find the polarization at a local point. DF in the same particle showed that the edge was a single domain.

- Charging and beam induced damage effects were found to be different depending on whether the microscope was working in TEM or STEM mode. In TEM mode, Pb nanoparticles with an FCC crystal structure appeared after a critical dose of $5.78\times10^{3}\frac{C}{cm^2}$ $(3.61*10^{6}\frac{e}{\mathring{A}^2})$, and in STEM mode the material was amorphized with a dose of $0.64\frac{C}{cm^2}$ $(3.99*10^{2}\frac{e}{\mathring{A}^2})$ per nanometer.

Chapter 6

Further Work

Preparing specimens with the tripod polisher was a main part of the study, and specimens were successfully made for the first time. However, the triopd specimens had a few drawbacks. The $ErMnO_3$ specimens suffered from too many defects that made DF overview imaging challenging, and the $Pb_5Ge_3O_{11}$ specimens were large creating too much charging for most electron microscopy techniques, especially conventional TEM technqiues that require a condensed beam such as CBED and HRTEM. Both the defects in $ErMnO_3$ and charging effects in $Pb_5Ge_3O_{11}$ can be overcome by using STEM techniques instead. STEM is less sensitive to defects due to the annular detectors, and scanning the probe does not cause beam deflection to the same degree. Common HAADF and BF STEM techniques will however not produce any contrast from domains so specific technqiues for STEM must be used. As briefly mentioned in section 2.2.6, one option is to displace the center beam to weaken and amplify to of the CBED disks in STEM mode. By studying CBED simulation one can look for disks or planes that are not mirrored over a domain wall, and in that case a displacing the central beam leads to a contrast from domains[62]. However, due to the large unit cell and consequently small Bragg angles, even the smallest condenser aperture are not able to prevent disk overlap in STEM mode so the lenses must be controlled manually[1].

Having polarization in the material can also lead to a shift of the CBED pattern due to coulomb deflection, which a segmented STEM detector can detect[64]. This technique is called differential phase contrast (DPC)-STEM, and can also be used to gain overview information on domain structures in STEM mode. An additional technique that is becoming more and more common is scanning precession electron diffraction (SPED) where the probe is precessed over a spot while the diffraction pattern is recorded and eventually averaged over[65]. This is equivalent to averaging each disks in the CBED pattern over a range of deviation parameters. While untested for the purpose of studying ferroelectric domains, but selectively adding certain parts of the PED patterns or using information in the FOLZ could be tried[66]. A final option to get confirmation of the polarization is scanning CBED (SCBED) as mentioned in section 2.2.6[30]. Although the lenses must be controlled manually to allow control of the convergence angle, the

[1]The ALPHA knob for adjusting convergence angle is not available in STEM mode.

scanning would reduce the dose in each region and also give the option of obtaining patterns from both sides of a domain wall quickly before beam deflection can move the probe. Implementing energy filtering could also enhance the difference in the CBED pattern of opposing domains[16]. These techniques along with other scanning techniques is called 4D STEM, and could be promising candiates for studying ferroelectric domain structures in specimens not accessible by conventional techniques[67]. These have not be applied to either materials so far.

Besides turning to additional TEM techniques, the specimens can be improved instead. Sputter coating to create a conductive surface layer can reduce the charging of the tripod specimens enough so they can be used in the TEM. If this does not work, new and specimens could be made. As suggested in chapter 4, preparing FIB lamellas of the bulk where the SEM can be used would allow for preparing small specimens with domains at known locations. The FIB also has the possibility to pick a certain orientation and optimal thickness (see figure 4.20). However, charging under the ion beam used for milling, might be a challenging, requiring an extra thick conducting protective layer. The results found in the present study without any ion milling, are good references to verify that the Ga ion milling has not altered/degraded the crystalline structure. This would allow for an easy way of testing the overview techniques since both domain locations and thickness are known, and even if they prove not be useful it would still be possible to continue to high resolution imaging. Since the polarization could only be determined in $ErMnO_3$ using close to perfect specimens and with an easily recognizable pattern of the Er atoms, an aberration corrected TEM must be used to obtain lattice images of the domain wall in $Pb_5Ge_3O_{11}$. After TEM characterization, the lamellas can also be scanned with SPM techniques for a final correlation with the functional properties of the material.

References

[1] "60 years of integrated circuits". In: *Nature Electronics* 1.9 (2018), pp. 483–483. DOI: 10.1038/s41928-018-0145-6.

[2] "Multiferroics march on". In: *Nature Materials* 18.3 (2019), pp. 187–187. DOI: 10.1038/s41563-019-0310-y.

[3] P. S. Bednyakov et al. "Physics and Applications of Charged Domain Walls". In: *npj Computational Materials* 4.1 (2018), p. 65. DOI: 10.1038/s41524-018-0121-8.

[4] J. A. Mundy et al. "Functional Electronic Inversion Layers at Ferroelectric Domain Walls". In: *Nature Materials* 16.6 (2017), pp. 622–627. DOI: 10.1038/nmat4878.

[5] M. E. Holtz et al. "Topological Defects in Hexagonal Manganites: Inner Structure and Emergent Electrostatics". In: *Nano Letters* 17.10 (2017), pp. 5883–5890. DOI: 10.1021/acs.nanolett.7b01288.

[6] G. Catalan et al. "Domain Wall Nanoelectronics". In: *Reviews of Modern Physics* 84.1 (2012), pp. 119–156. DOI: 10.1103/RevModPhys.84.119.

[7] D. Meier et al. "Anisotropic Conductance at Improper Ferroelectric Domain Walls". In: *Nature Materials* 11.4 (2012), pp. 284–288. DOI: 10.1038/nmat3249.

[8] M. Han et al. "Ferroelectric Switching Dynamics of Topological Vortex Domains in a Hexagonal Manganite". In: *Advanced Materials* 25.17 (2013), pp. 2415–2421. DOI: 10.1002/adma.201204766.

[9] V. V. Aristov, L. S. Kokhanchik, and V. G. Monya. "Investigations of Domain Contrast in $Pb_5Ge_3O_{11}$ with a Scanning Electron Microscope". In: *Ferroelectrics* 70.1-2 (1986), pp. 15–26. DOI: 10.1080/00150198608221417.

[10] E. I. Shishkin et al. "Local Study of Polarization Reversal Kinetics in Ferroelectric Crystals Using Scanning Probe Microscopy". In: *Ferroelectrics* 374 (2008), pp. 26–32. DOI: 10.1080/00150190802424769.

[11] V. Y. Shur et al. "Domain Structure of Lead Germanate". In: *Ferroelectrics* 98.1 (1989), pp. 29–49. DOI: 10.1080/00150198908217568.

[12] K. Sugii et al. "X-Ray Topographic Observation of 180 Degrees Domains in Ferroelectric $Pb_5Ge_3O_{11}$ Single-Crystals". In: *Journal of Crystal Growth* 16.3 (1972), pp. 291–293. DOI: 10.1016/0022-0248(72)90220-5.

[13] H. Iwasaki et al. "Ferroelectric and Optical Properties of $Pb_5Ge_3O_{11}$ and Its Isomorphous Compound $Pb_5Ge_2SiO_{11}$". In: *Journal of Applied Physics* 43.12 (1972), pp. 4907–4915. DOI: 10.1063/1.1661044.

[14] Jun Hatano et al. "Crystal Structure of the Metastable State of Ferroelectric Lead Germanate". In: *Japanese Journal of Applied Physics* 36.9S (1997), p. 6155.

[15] Private communication, Theodor S. Holstad (Institute of Materials Science, NTNU). 2019.

[16] D. B. Williams and C. B. Carter. *Transmission Electron Microscopy*. 2nd Edition. Springer US, 2009.

[17] J. Li et al. "Scanning Secondary-electron Microscopy on Ferroelectric Domains and Domain Walls in $YMnO_3$". In: *Applied Physics Letters* 100.15 (2012). DOI: 10.1063/1.4704165.

[18] Y. Yu et al. "Atomic-Scale Study of Topological Vortex-Like Domain Pattern in Multiferroic Hexagonal Manganites". In: *Applied Physics Letters* 103.3 (2013). DOI: 10.1063/1.4813755.

[19] T. Choi et al. "Insulating Interlocked Ferroelectric and Structural Antiphase Domain Walls in Multiferroic $YMnO_3$". In: *Nature Materials* 9 (2010), p. 253. DOI: 10.1038/nmat2632https://www.nature.com/articles/nmat2632#supplementary-information.

[20] J. Schaab et al. "Electrical Half-wave Rectification at Ferroelectric Domain Walls". In: *Nature Nanotechnology* 13 (2018), 1028–1034. DOI: 10.1038/s41565-018-0253-5.

[21] *MULTIPREP POLISHING SYSTEM - Product Information"*. Visited on 15/11/18. URL: http://www.alliedhightech.com/Equipment/multiprep-polishing-system-12.

[22] C. Kittel. *Introduction to Solid State Physics*. 8th Edition. John Wiley and Sons, Inc., 2005.

[23] E. J. Samuelsen. *Material physics; Structure, diffraction, imaging and spectroscopy; Lecture notes*. NTNU, Department of Physics, 2006.

[24] B. Fultz and J. Howe. *Transmission Electron Microscopy and Diffractometry of Materials*. 4th Edition. Springer, Berlin, Heidelberg, 2013. DOI: https://doi.org/10.1007/978-3-642-29761-8.

[25] J. M. Zuo and J. C. H. Spence. *Advanced Transmission Electron Microscopy: Imaging and Diffraction in Nanoscience*. Springer, New York, NY, 2017.

[26] D. Talantikite and L. Taïbi-Benziada. "Phase transitions of $CaTiO_3$ ceramics sintered with the aid of NaF and MgF_2". In: *Solid State Sciences* 11.1 (2009), pp. 151–155. DOI: https://doi.org/10.1016/j.solidstatesciences.2008.05.002.

[27] R. Gevers, H. Blank, and S. Amelinckx. "Extension of the Howie-Whelan Equations for Electron Diffraction to Non-Centro Symmetrical Crystals". In: *physica status solidi (b)* 13.2 (1966), pp. 449–465. DOI: 10.1002/pssb.19660130217.

[28] L. Jones. *SmartAlign Software Package*. http://lewysjones.com/software/smart-align/. Accessed on 25-02-2019.

[29] L. Jones et al. "Smart Align—a New Tool for Robust Non-Rigid Registration of Scanning Microscope Data". In: *Advanced Structural and Chemical Imaging* 1.1 (2015), p. 8. DOI: 10.1186/s40679-015-0008-4.

[30] K. Tsuda, A. Yasuhara, and M. Tanaka. "Two-dimensional Mapping of Polarizations of Rhombohedral Nanostructures in the Tetragonal Phase of $BaTiO_3$ by the Combined Use of the Scanning Transmission Electron Microscopy and Convergent-beam Electron Diffraction Methods". In: *Applied Physics Letters* 103.8 (2013), p. 082908. DOI: 10.1063/1.4819221.

[31] Y.-T. Shao and J.-M. Zuo. "Nanoscale Symmetry Fluctuations in Ferroelectric Barium Titanate, $BaTiO_3$". In: *Acta Crystallographica Section B* 73.4 (2017), pp. 708–714. DOI: doi:10.1107/S2052520617008496.

[32] Goerg H. Michler. "Electron Microscopy of Polymers". In: Berlin, Heidelberg: Springer Berlin Heidelberg, 2008. DOI: 10.1007/978-3-540-36352-1_5.

[33] G. F. Dionne. "Origin of Secondary-electron-emission Yield-curve Parameters". In: *Journal of Applied Physics* 46.8 (1975), pp. 3347–3351. DOI: 10.1063/1.322061.

[34] R. F. Egerton. *Physical Principles of Electron Microscopy*. Springer US, 2005. DOI: 10.1007/b136495.

[35] G. Rosenman et al. "Observation of Ferroelectric Domain Structures by Secondary-electron Microscopy in As-grown $KTiOPO_4$ crystals". In: *Physical Review B* 54.9 (1996), pp. 6222–6226. DOI: 10.1103/PhysRevB.54.6222.

[36] P. Barone and S. Picozzi. "Mechanisms and Origin of Multiferroicity". In: *Comptes Rendus Physique* 16.2 (2015), pp. 143–152. DOI: https://doi.org/10.1016/j.crhy.2015.01.009.

[37] M. Fiebig et al. "The Evolution of Multiferroics". In: *Nature Reviews Materials* 1 (2016), p. 16046. DOI: 10.1038/natrevmats.2016.46.

[38] Y. Iwata. "Neutron-Diffraction Study of Structure of Paraelectric Phase of $Pb_5Ge_3O_{11}$". In: *Journal of the Physical Society of Japan* 43.3 (1977), pp. 961–967. DOI: 10.1143/jpsj.43.961.

[39] T. Baikie et al. "Polysomatic Apatites". In: *Acta Crystallographica Section B-Structural Science* 66 (2010), pp. 1–16. DOI: 10.1107/s0108768109053981.

[40] S. M. Griffin et al. "Scaling Behavior and Beyond Equilibrium in the Hexagonal Manganites". In: *Physical Review X* 2.4 (2012), p. 041022. DOI: 10.1103/PhysRevX.2.041022.

[41] B. B. Van Aken et al. "The origin of ferroelectricity in magnetoelectric $YMnO_3$". In: *Nature Materials* 3 (2004), 164–170. DOI: 10.1038/nmat1080.

[42] Doughert. J, Sawaguch. E, and L. E. Cross. "Ferroelectric Optical-Rotation Domains in Single-Crystal $Pb_5Ge_3O_{11}$". In: *Applied Physics Letters* 20.9 (1972), p. 364. DOI: 10.1063/1.1654188.

[43] E. Eberg et al. "Comparison of TEM Specimen Preparation of Perovskite Thin Films by Tripod Polishing and Conventional Ion Milling". In: *Journal of Electron Microscopy (Tokyo)* 57.6 (2008), pp. 175–179. DOI: 10.1093/jmicro/dfn018.

[44] M. Fiebig et al. "Determination of the Magnetic Symmetry of Hexagonal Manganites by Second Harmonic Generation". In: *Physical Review Letters* 84.24 (2000), pp. 5620–5623. DOI: 10.1103/PhysRevLett.84.5620.

[45] H. L. Yakel et al. "On the Crystal Structure of the Manganese(III) Trioxides of the Heavy Lanthanides and Yttrium". In: *Acta Crystallographica* 16.10 (1963), pp. 957–962. DOI: doi:10.1107/S0365110X63002589.

[46] *ErMnO3 Crystal Structure: Datasheet from "PAULING FILE Multinaries Edition – 2012" in SpringerMaterials*. https://materials.springer.com/isp/crystallographic/docs/sd_1502735. Accessed on 25-02-2019.

[47] H. Iwasaki et al. "5PbO·3GeO_2 Crystal; a New Ferroelectric". In: *Applied Physics Letters* 18.10 (1971), pp. 444–445. DOI: 10.1063/1.1653487.

[48] R. Viennois et al. "Influence of Cr^{3+} Doping on the Enhanced Dielectric and Nonlinear Optical Features of Pyroelectric $Pb_5Ge_3O_{11}$ Single Crystals". In: *Materials Chemistry and Physics* 213 (2018), pp. 461–471. DOI: 10.1016/j.matchemphys.2018.04.025.

[49] X. Wu, J. Xu, and W. Jin. "Growth Defects of Lead Germanate Single Crystals Grown by the Vertical Bridgman Method". In: *Materials Characterization* 55.2 (2005), pp. 143–147. DOI: https://doi.org/10.1016/j.matchar.2005.04.003.

[50] M. I. Kay, R. E. Newnham, and R. W. Wolfe. "Crystal Structure of Ferroelectric Phase of $Pb_5Ge_3O_{11}$". In: *Ferroelectrics* 9.1-2 (1975), pp. 1–6. DOI: 10.1080/00150197508240073.

[51] J. R. Whyte et al. "Ferroelectric Domain Wall Injection". In: *Advanced Materials* 26.2 (2014), pp. 293–298. DOI: doi:10.1002/adma.201303567.

[52] P. Gao et al. "Revealing the Role of Defects in Ferroelectric Switching With Atomic Resolution". In: *Nature Communications* 2 (2011), p. 591. DOI: https://doi.org/10.1038/ncomms1600.

[53] R. F. Egerton, P. Li, and M. Malac. "Radiation Damage in the TEM and SEM". In: *Micron* 35.6 (2004), pp. 399–409. DOI: https://doi.org/10.1016/j.micron.2004.02.003.

[54] J.L. Hollenbeck and R.C. Buchanan. "Oxide thin films for nanometer scale electron beam lithography". In: *Journal of Materials Research* 5.5 (1990), 1058–1072. DOI: 10.1557/JMR.1990.1058.

[55] R. F. Egerton. "Radiation Damage to Organic and Inorganic Specimens in the TEM". In: *Micron* 119 (2019), pp. 72–87. DOI: https://doi.org/10.1016/j.micron.2019.01.005.

[56] L. W. Hobbs. "Topology and Geometry in the Irradiation-Induced Amorphization of Insulators". In: *Nuclear Instruments and Methods in Physics Research Section B: Beam Interactions with Materials and Atoms* 91.1 (1994), pp. 30–42. DOI: https://doi.org/10.1016/0168-583X(94)96187-5.

[57] K. A. Mkhoyan et al. "Effects of Amorphous Layers on ADF-STEM Imaging". In: *Ultramicroscopy* 108.8 (2008), pp. 791–803. DOI: https://doi.org/10.1016/j.ultramic.2008.01.007.

[58] Y. Ding, J. S. Liu, and Y. N. Wang. "Transmission Electron Microscopy Study on Ferroelectric Domain Structure in $SrBi_2Ta_2O_9$ Ceramics". In: *Applied Physics Letters* 76.1 (1999), pp. 103–105. DOI: 10.1063/1.125670.

[59] H. Tsukasaki, S. Mori, and Y. Koyama. "Features of the Ferroelectric Rhombohedral State in $Ba(Ti_{1-x}Zr_x)O_3$ Having the Simple Perovskite Structure". In: *Journal of the Ceramic Society of Japan* 123.1441 (2015), pp. 913–919. DOI: 10.2109/jcersj2.123.913.

[60] B. Yao et al. "High Contrast Hollow-Cone Dark Field Transmission Electron Microscopy for Nanocrystalline Grain Size Quantification". In: *Micron* 41.3 (2010), pp. 177–182. DOI: https://doi.org/10.1016/j.micron.2009.11.008.

[61] J. S. Barnard et al. "The Role of Rough Surfaces in Quantitative ADF Imaging of Gallium Nitride-Based Materials". In: *Journal of Physics: Conference Series* 209 (2010), p. 012019. DOI: 10.1088/1742-6596/209/1/012019.

[62] X. He, L. Gu, and A. Rockett. "Scanning Transmission Electron Microscopy Imaging of 180 Degrees Ferroelectric Domains and Application to $Ca_{0.28}Ba_{0.72}Nb_2O_6$ Single Crystals". In: *Applied Physics Letters* 109.26 (2016). DOI: 10.1063/1.4973453.

[63] L. Jones et al. "Managing Dose-, Damage- and Data-Rates in Multi-Frame Spectrum-Imaging". In: *Microscopy* 67 (2018), pp. i98–i113. DOI: 10.1093/jmicro/dfx125.

[64] T. Matsumoto. "Nanoscale Ferroelectric-Multiferroic Materials for Energy Harvesting Applications". In: Elsevier, 2019. DOI: https://doi.org/10.1016/B978-0-12-814499-2.00007-4.

[65] E. F. Rauch and M. Véron. "Automated Crystal Orientation and Phase Mapping in TEM". In: *Materials Characterization* 98 (2014), pp. 1–9. DOI: https://doi.org/10.1016/j.matchar.2014.08.010.

[66] Y. Ma, P. Oleynikov, and O. Terasaki. "Electron Crystallography for Determining the Handedness of a Chiral Zeolite Nanocrystal". In: *Nature Materials* 16 (2017), p. 755. DOI: 10.1038/nmat4890https://www.nature.com/articles/nmat4890#supplementary-information.

[67] C. Ophus. "Four-Dimensional Scanning Transmission Electron Microscopy (4D-STEM): From Scanning Nanodiffraction to Ptychography and Beyond". In: *Microscopy and Microanalysis* 25.3 (2019), pp. 563–582. DOI: 10.1017/S1431927619000497.

Appendix A

Mechanical Polishing Routine

The routine here is used on all samples as described from section 3.2, and are taken from [43]. The original paper discussed thin films on a substrate, but the work is adapted for bulk material in this case.

1. **Cutting and gluing the sample to the pyrex**
    - Mount the sample on a glass slide with wax. Heat the wax to 100°C to melt it.
    - Cut into slabs of 1 ×1-2 mm^2 using *Testbourne Model 650 Low Speed Diamond Wheel Saw* with a 60 µm thin diamond blade. Use load > 100 g and speed 10 rpm.
    - Remove the sample from the glass slider first, then clean the slabs in acetone for 1 min and rinse in ethanol to remove the wax.
2. **Polishing of reference plane (first polishing)**
    - Polish a pyrex flat using 6 µm diamond lapping film (DLF) at 50 rpm and 500 g load. Oscillate the pyrex on one of the plate sides, with oscillation radius about two-thirds of the plate radius while washing the DLF continuously with water. Inspect in VLM to make sure it is flat.
    - Apply a small amount of *Loctite Precision* acetone soluble glue with a toothpick to the pyrex, and attach the sample. The sample should be oriented in such a way edge chipping is most unlikely. Let it cure for a day, and then rinse shortly in acetone to remove any glue outside the sample.
    - Polish with 15 µm DLF until the top of the sample is flat. Use load of 200 g, rotation speed of 30 rpm, sample oscillation speed of 1 and zero angle from the plate plane. continuously wash the plate with water, and rinse afterwards in de-ionised water before next step.
    - Polish off 50 µm using 6 µm DLF with the same conditions as above.
    - Polish off 20 µm using 3 µm DLF with the same conditions as above.

- Polish off 10 µm using 1 µm DLF and same conditions as above, but using a load of 50 g instead and *Allied GreenLube* lubricant instead of water. Inspect in a VLM and repeat this step if deep scratches are observed, as they can cause the sample to break when polishing the other side.
- Polish for 20 s with 0.5 µm DLF as in the previous step.
- Polish for 20 s with 0.1 µm DLF as in the previous step.
- Polish for 1 min s with a cloth stained with *Allied* 0.02 µm *Colloidal Silica* without any load applied, and clean using *Allied Micro Organic* soap applied with a cotton swab before rinsing in water.
- Put the pyrex and sample in an acetone beaker for 1 hour or until the sample falls off, and rinse both in an ethanol beaker. Re-attach the sample to the pyrex using *Loctite Precision* glue with the polished side facing into the pyrex. Let it cure for a day.

3. **Polishing into wedge (second polishing)**

- Polish the sample down to 500 µm with a 15 µm DLF, then introduce a 2° angle and keep polishing until the edge reaches 250 µm. Use a load of 200 g, rotation speed of 30 rpm, oscillation speed of 1 and an oscillation radius of two-thirds of the plate radius. Wash the DLF continuously with water, and ensure that the edge of the sample is perpendicular to the polishing direction. Adjust the sample holder if there is an angle as it can cause edge chipping.
- Polish with 6 µm DLF until the edge is 150 µm thick using the same conditions as above.
- Polish with 3 µm DLF until the edge is 60 µm thick using the same conditions as above.
- Polish in steps of 30 s with 1 µm DLF until the edge begins to move and the pyrex becomes visible. Use *Allied GreenLube* lubricant instead of water, and set load to 0 g. Inspect in VLM at every step to make sure cracks have not formed and large pieces of the edge is not falling off, if so proceed to next step.
- Polish for 15 s with 0.5 µm DLF using the same conditions as above. Inspect in VLM and see if more cracks are forming or edge is beginning to loose large bits, if so proceed to the next step.
- Polish for 1 min with *Allied* 0.02 µm *Colloidal Silica* stained cloth and clean using *Allied Micro Organic* soap applied with a cotton swab before rinsing in water.

4. **Mounting sample to a TEM grid**

- Using *Biltema Quick-Epoxy* two-part, acetone-resistant glue, apply a very small amount to the sample while attached to the pyrex using a sharpened

toothpick. Make sure no glue hits the pyrex, and place the TEM grid of Mo or Cu on top of the sample without covering the electron transparent edge. Let it cure for a day.

- Put the pyrex and sample on top of a paper filter in an acetone beaker for 1 hour or until the sample falls off, and rinse both in an ethanol beaker.

Appendix B

CBED Calibration

Figure B.1 shows the calibration curve for the 2100 microscope, where the apertures 1-4 (10, 50, 70 and 150 µm) and ALPHA knob (setting 1-9) determines the resulting convergence angle α.

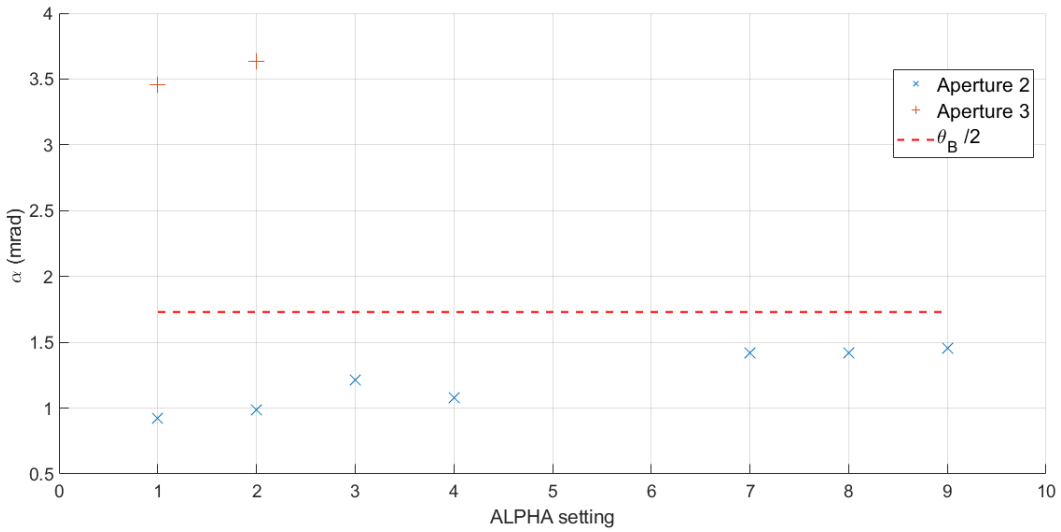

Figure B.1: Calibration curve for the CBD mode in the 2100 microscope with the convergence angle α plotted against the ALPHA knob setting and the condenser aperture. The apertures 2 (50 µm) and 3 (70 µm) were tried. The ALPHA knob had 9 possible settings (1-9), but setting 5 and 6 on aperture 2 was not tried, and only 1 and 2 was tried for aperture 3. The stripled line is half the Bragg angle, 1.73 mrad.

The ideal convergence angle is when the disks barely touch, which is half the Bragg angle (to the 002 disk), θ_B, indicated in the figure by a stripled line as 1.73 mrad for $ErMnO_3$. This angle was not found, as the figure shows the gap between aperture 2, ALPHA 9 and aperture 3, ALPHA 1 to contain the ideal angle. The result was that aperture 3 always lead to overlap of the disks, while aperture 2 was slightly too small to

reach the ideal angle, but still usable. The ALPHA settings did not have a large effect on the convergence angle when using aperture 2, as can be seen from the figure. For the 2100F microscope, the apertures 1-4 are slightly different (10, 40, 100 and 250 µm). For $ErMnO_3$, this means the gap between aperture 2 and 3 is even larger and more impractical. $Pb_5Ge_3O_{11}$ on the other hand had a half Bragg angle of only 1.17 mrad, which means aperture 2 (40 µm) was placed almost ideally for any ALPHA setting. Normal TEM mode was therefore used with ALPHA 3 (ALPHA 5 or 6 in CBED mode) with aperture 2.

Appendix C

CBED Simulations (off-zone)

Figures C.1 and C.2 shows CBED simulations of $ErMnO_3$ from the *JEMS* software for imperfect placement of the zone-axis. Ideally, the [100] direction is to be used (section 2.1.1 and figure 2.24(b)), but if the tilting is off by 0.1°, the result is a significant change in contrast within the disks. It is worth noting that tilting 0.1° does not return the same result as tilting −0.1° while rotating the pattern 180°, even if the tilt is the cause for most of the contrast (due to the polarization). In figure C.2, the 004 disk in (a) is not exactly equal to the $00\bar{4}$ disk in (b).

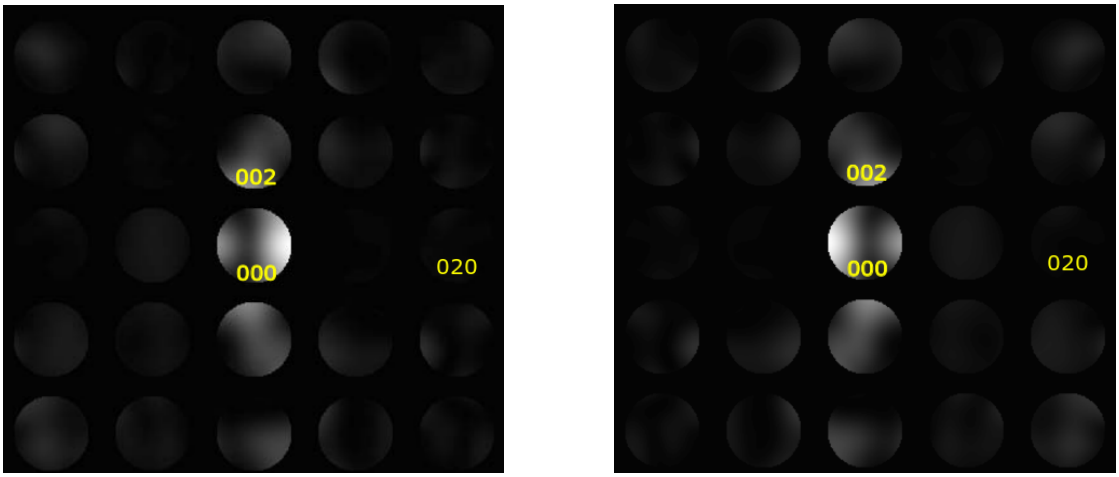

(a) (b)

Figure C.1: (a) CBED simulation for $ErMnO_3$ from *JEMS* with a 0.1° tilting towards the $0\bar{1}0$ disk. (b) CBED simulation with a 0.1° tilting towards the 010 disk.

Figure C.3 shows how the CBED simulations change as the tilting changes from 0.01° to 0.05° towards the $00\bar{2}$ disk. The tilting at low angles is almost a simple shift of the pattern in the direction of the tilt.

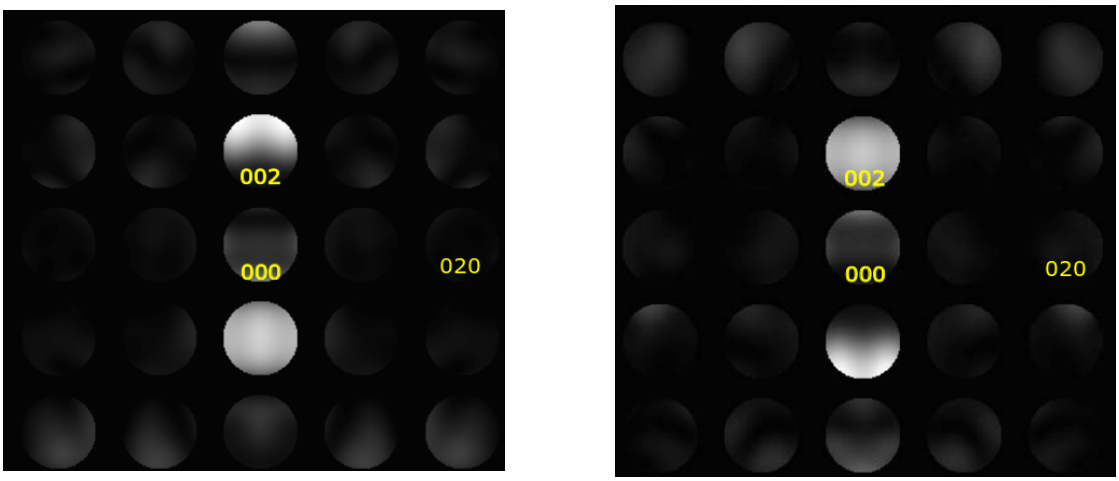

(a) (b)

Figure C.2: (a) CBED simulation for $ErMnO_3$ from *JEMS* with a 0.1° tilting towards the $00\bar{2}$ disk. (b) CBED simulation with a 0.1° tilting towards the 002 disk.

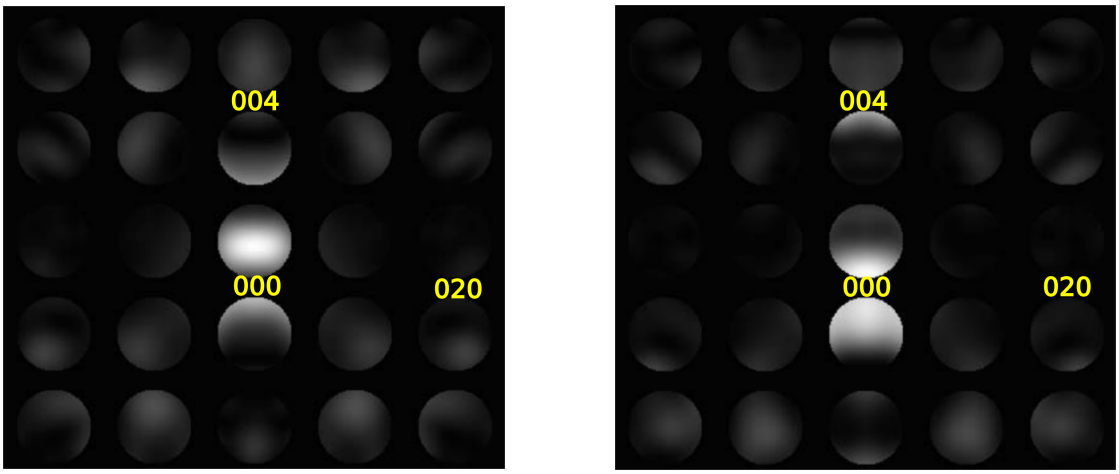

(a) (b)

Figure C.3: CBED simulations for $ErMnO_3$ from the *JEMS* software with (a) 0.01° and (b) 0.05° tilt towards the $00\bar{2}$ disk.

Appendix D

SAED Simulations

Figure D.1 shows a *JEMS* simulation of SAED along the [001] zone axis of PGO at 100 nm thickness. The simulation has taken dynamic effects into account by treating all reflections through the two-beam case. Note that a "handedness" is present with the 120 and 210 reflections and their counterparts by a 60° rotation. The 120 is significantly weaker than 210, just as $\bar{2}30$ is much weaker than $\bar{1}30$ and the same goes for the other four pairs.

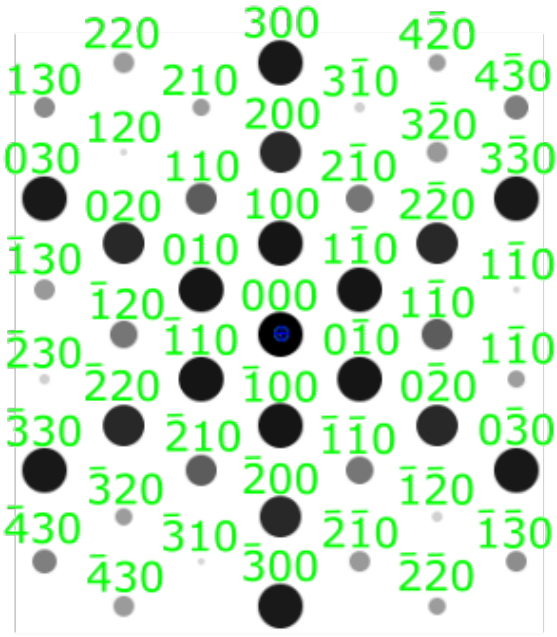

Figure D.1: JEMS kinematic SAED simulation of the 001 zone axis in $Pb_5Ge_3O_{11}$ at 100 nm thickness.

To get a complete picture of this "handedness", simulations from JEMS between 0 and 200 nm thickness is shown in figure D.2. In this case the $\bar{2}30$ and $\bar{1}30$ reflections

are used, and opposite domains will use the opposite reflection if one is selected in DF imaging. The difference between the intensity can be seen to be far larger than any reflection along the 100 zone axis, most likely because there is a kinematic component to the difference (figure D.1) in addition to a dynamic component[1].

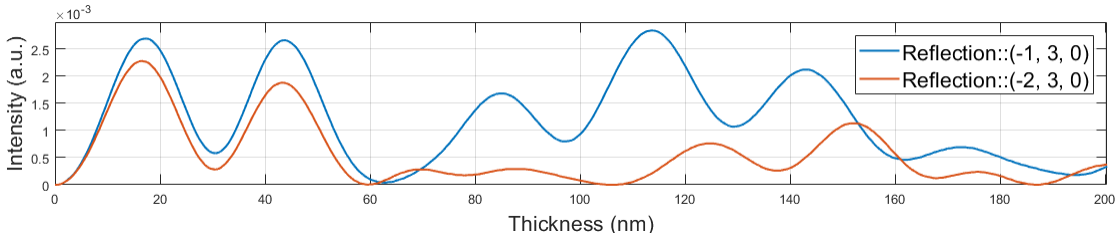

Figure D.2: *JEMS* dynamical SAED simulation of the $\bar{1}30$ and $\bar{2}30$ reflections along the 001 zone axis.

[1]When comparing reflections that exchange position under an inversion, they are kinematically identical and any difference originate due to a dynamical effect.

Kasper Aas Hunnestad

Visualizing Ferroelectric Domain Structures in $ErMnO_3$ and $Pb_5Ge_3O_{11}$ by Electron Microscopy

NTNU
Kunnskap for en bedre verden